Dissertation

Understanding the Solubility and Mechanical Elastic Properties of Ti–B–N Thin Films

carried out for the purpose of obtaining the degree of Doctor technicae (Dr. techn.),

submitted at TU Wien
Faculty of Mechanical and Industrial Engineering
by
Rebecca JANKNECHT
Mat.No.: 01127798

under the supervision of
Univ.Prof. Dipl.-Ing. Dr. mont. Paul Heinz Mayrhofer
Institute of Materials Science and Technology, E308-01
and
Dipl.-Ing. Dr. techn. Rainer Hahn
Institute of Materials Science and Technology, E308-01

Reviewed by

Prof. Lars Hultman
Linköping University
SE-581 83 Linköping

Vienna, 27.06.2024

Ass. Prof. Ian McCue
Northwestern University
Evanston, IL 60208

Vienna, 27.06.2024

I confirm, that the printing of this thesis requires the approval of the examination board.

Affidavit

I declare in lieu of oath, that I wrote this thesis and carried out the associated research myself, using only the literature cited in this volume. If text passages from sources are used literally, they are marked as such. I also confirm that no generative artificial intelligence (AI) has been used in the writing of this work.

I confirm that this work is original and has not been submitted for examination elsewhere, nor is it currently under consideration for a thesis elsewhere.

I acknowledge that the submitted work will be checked electronically-technically using suitable and state-of-the-art means (plagiarism detection software). On the one hand, this ensures that the submitted work was prepared according to the high-quality standards within the applicable rules to ensure good scientific practice "Code of Conduct" at the TU Wien. On the other hand, a comparison with other student theses avoids violations of my personal copyright.

Vienna, 27.06.2024

Rebecca Janknecht

Acknowledgements

I am deeply grateful to all those who have supported me throughout my journey as a graduate student over the past few years. I would like to express my sincerest gratitude to my supervisor, **Prof. Paul H. Mayrhofer**, for his patience and belief in my ideas, allowing me to find my own path even in challenging times. His open-door policy, along with the opportunities he provided to attend various conferences and conduct research at external institutions, greatly enriched my academic and personal experience. Additionally, I am deeply grateful to **Rainer Hahn**, for his guidance and support throughout my work. His insightful discussions significantly expanded my knowledge of materials science, and his way of thinking greatly contributed to my research. His willingness to address my questions and ideas was truly invaluable. Together, we made a great team. I also extend my gratitude to **Nikola Koutná** for supporting this work with her incredible DFT skills and translating my ideas into calculations. Special thanks go to **Balint Hajas** for his support in the PVD lab and his culinary talents, which brought joy to our entire group. I am further truly grateful to the members of the USTEM facility, especially **Andreas Steiger-Thirsfeld** and **Jakob Gruber**, for their assistance and guidance in preparing samples for TEM studies and synchrotron beamtime. I would like to thank **Tomasz Wójcik**, **Zhuo Chen**, and **Prof. Zaoli Zhang** for their assistance in the TEM studies and inspiring discussions. I would also like to thank **Anton Davydok**, beamline scientist at PETRA III in Hamburg, for his support during the synchrotron experiments as well as **Juraj Todt** and **Michael Meindlhumer** for their invaluable help and guidance in analyzing the synchrotron data. My former and present fellow graduate students, especially **Barbara**, **Anna**, **Shuyao**, **Chun**, **Sophie**, **Thia**, **Katharina**, **Erwin**, **Ludwig**, and **Alexander**, I would like to thank you all for the many precious memories of conference visits and countless hours spent together in the lab. We work better together, and together we work better. I would also like to express my heartfelt gratitude to all members of my family, especially **my parents**, for nurturing my love for learning and encouraging my talents, shaping me into the woman I am today, and for having two incredible sisters. My final thanks go to my loving husband **Markus**. As I struggled to hold the atoms together, you kept me from falling apart.

"Sputterpeople will go to heaven."

Wolf-Dieter Münz

Table of Contents

English Abstract

In today's industry, ceramic hard coatings have become necessary to extend the service life and improve the properties of tools and components. Of particular interest is the class of transition metal nitrides, with face-centered cubic (fcc) TiN being the most widely used and studied coating material. Alloying is a widely used method to improve the performance of this material. An excellent example of alloying is the addition of B or Al to improve mechanical properties. However, it has been shown that the solubility of B on the non-metal lattice of fcc-TiN—unlike that of Al on the metallic lattice of fcc-TiN—is not trivial, since only a few atomic percent of the provided amount can be dissolved due to constraints, beyond which precipitation occurs. This work shows that a B solubility of up to 10 at.% (equivalent to 20 at% of the non-metal sublattice) can be easily achieved by controlled manipulation of the TiN-based lattice through vacancies at the non-metal sublattice and/or metal-alloying at the metal sublattice. When B is completely dissolved in the fcc-TiN lattice, there is a slight increase in fracture toughness compared to pure fcc-TiN. In contrast, coatings with the same B content—where excess B segregates amorphously at the grain boundaries—exhibit similar hardness, but the solubility of up to 10 at.% B results in a significant increase in fracture toughness. The B solubility was primarily investigated by detailed X-ray diffraction studies and confirmed by complementary high-resolution transmission electron microscopy. As important as the solubility of alloying elements in a material system is the determination of the properties relevant to the application. Density functional theory calculations are at the forefront of modern materials science in this regard. However, their inherent limitation of calculating only elastic properties, which are very difficult to determine experimentally, limits their full potential and leaves materials science without an essential feedback tool. Therefore, this thesis also concentrates on a new combined micromechanical method based on synchrotron diffraction to fully derive the elastic constants purely by experiments (including the Poisson's ratio, which is often simply assumed or calculated).

This study shows not only how to determine the solubility of the desired alloying element boron in TiN, but also how this affects the application-relevant properties, how this solubility can be modified, and finally, a methodology to entirely determine the elastic constants of thin films.

In a general context, all these studies can be applied to the Ti-B-N model system and, in principle, to all material systems, thus representing a significant enrichment in the field of materials science.

Deutsche Kurzfassung

Keramische Hartstoffschichten sind zu einer Notwendigkeit geworden, um die die Eigenschaften von Werkzeugen und Bauteilen zu verbessern und damit deren Lebensdauer zu verlängern. Besonders hervorzuheben ist die Klasse der Übergangsmetallnitride, wobei kubisch flächenzentriertes (kfz) Titannitrid (TiN) als das am häufigsten verwendete und untersuchte Schichtmaterial einen Spezialfall darstellt. Um die Beanspruchbarkeit von TiN Hartstoffschichten zu verbessern, wird TiN häufig ein drittes Element zulegiert. Ein gelungenes Beispiel ist die Legierung mit Bor oder Aluminium zur Verbesserung der mechanischen Eigenschaften. Es hat sich jedoch gezeigt, dass die Löslichkeit von Bor im nichtmetallischen Gitter im Gegensatz zur Löslichkeit von Aluminium im metallischen Gitter von kfz-TiN nicht trivial ist, da das wesentlich größere Boratom aufgrund geometrischer/thermodynamischer/kinetischer Limitierungen nur zu einem sehr geringen Anteil im kfz Gitter gelöst werden kann. Zudem führt ein Überschuss an Bor zur Ausbildung weiterer Phasen (z.B. amorphen Korngrenzenphasen). In dieser Arbeit konnte gezeigt werden, dass einerseits durch kontrolliertes Einbringen von Leerstellen am Nichtmetallgitter und andererseits durch gezieltes Legieren größerer Atomen im Metallgitter eine Borlöslichkeit von bis zu 10 at.% (entsprechend 20 at% am Nichtmetalluntergitter) problemlos erreicht werden kann. Dies führte bei gleicher Härte zu einer leichten Erhöhung der Bruchzähigkeit gegenüber dem Ausgangssystem kfz-TiN und zu einer deutlichen Verbesserung gegenüber einer Schicht mit ähnlichem (nicht gelöstem) B-Gehalt. Diese Löslichkeit wurde hauptsächlich durch detaillierte Röntgendiffraktionsmessungen und durch ergänzende Hochauflösende Transmissionselektronenmikroskopie bestätigt. Ebenso wichtig wie die Löslichkeit von Legierungselementen in einem Werkstoffsystem ist die Bestimmung der anwendungsrelevanten Eigenschaften. Die Anwendung der Dichtefunktionaltheorie gilt in der heutigen Materialwissenschaft als wegweisend, hat aber die inhärente Einschränkung, dass z.B. die berechneten elastischen Eigenschaften experimentell nur sehr schwer zu verifizieren sind. Damit fehlt der Materialwissenschaft ein wichtiges Rückkopplungswerkzeug. Im dritten Teil dieser Arbeit wird eine neue kombinierte mikromechanische Methode basierend auf Röntgenbeugung mit Sychrotronstrahlung vorgestellt, die sich genau dieser Problematik annimmt und eine rein experimentelle Bestimmung der elastischen Konstanten von dünnen Schichten erlaubt.

Diese Arbeit zeigt nicht nur wie die Löslichkeit eines gewünschten Legierungselements (hier Bor) in kfz-TiN modifiziert werden kann, sondern auch, welche Auswirkungen dies auf die

anwendungsrelevanten Eigenschaften hat. Allgemein betrachtet lassen sich all diese Methoden nicht nur auf das gewählte Modellsystem Ti–B–N, sondern prinzipiell auf alle Materialsysteme anwenden und stellen somit eine wesentliche Bereicherung auf dem Gebiet der Materialwissenschaften dar.

1 Introduction and Motivation

In materials science and engineering, scientists seek to understand the structure, behavior, and performance of materials to explore their properties and improve them for targeted technological applications. With a background in fashion design, I have long been fascinated by how creativity combines with technical precision to bring aesthetic vision and functional design to life. In fashion design, a clothing item is not merely a utilitarian object; it serves as a second skin, protecting it from the elements while expressing individuality and style. Just as fashion designers carefully select fabrics, textures, colors, and patterns to adorn the human form, researchers in coating technology tailor the composition and structure of thin films to decorate and enhance the performance of bulk materials.

In particular, physical vapor deposition (PVD) has emerged as a versatile tool in modern surface engineering [1]. Compared to traditional metallurgical strategies, PVD techniques offer distinct advantages over bulk synthesis, requiring significantly less material to provide effective surface protection against various external factors such as wear, corrosion, oxidation, abrasion, or chemical exposure [2]. In addition, the kinetically controlled path that sputtered atoms/species follow as they transition from the gaseous to the solid state—at exceptionally high cooling rates (~10^6 K/s)—facilitates the formation of metastable phases (in contrast to traditional synthesis routes constrained by equilibrium thermodynamics). The atomic bombardment inherent in PVD techniques, such as magnetron sputtering, facilitates the transfer of target material to the substrate, allowing precise control of the film growth morphology [3]. During this process, the energy imparted to the atoms introduces numerous defects into the crystal lattice of the deposited thin films, which act as strengthening mechanisms to enhance the mechanical properties of PVD sputtered coatings. By adjusting deposition parameters such as temperature, pressure, bias potential, and deposition rate; the coatings thickness, composition, and microstructure can be precisely tuned, enabling optimization as well as modification of thin film properties to improve the performance, reliability, and longevity of coated components and surfaces.

The applicability of PVD to many elements of the periodic table and its unparalleled flexibility in process parameters have made it an attractive and powerful tool for industry and science since its commercialization nearly half a century ago. While sputtering was first observed by Sir W.R. Grove [4] in 1852, it did not gain commercial importance until the 1940s, when more reliable and affordable vacuum equipment became available for surface coating purposes. In the early 1970s, magnetron sputtering sources developed by J.S. Chapin [5] emerged as a promising alternative toward faster deposition rates. However, early magnetron sources (where the magnetic field, $\boldsymbol{B}$, was symmetrically distributed) trapped the plasma close to the surface of the sputtering target, resulting in low ion bombardment and poor film quality. Although efforts have been made to overcome this limitation, such as adding additional ionization sources or using radio frequency, B. Windows and N. Savvides [6] discovered a more effective solution with the invention of the unbalanced magnetron in 1986. This unbalanced configuration allows some electrons to escape the confining $\boldsymbol{ExB}$ field (where $\boldsymbol{E}$ is the electric field), generating plasma in regions away from the target surface. When these escaping electrons are linked to other unbalanced magnetron sources (typically from south to north poles), the potential area where plasma can persist expands significantly. Together, the efforts of pioneering researchers such as J.A. Thornton [7,8], R.F. Bunshah [9], W.D. Sproul [10, 11], and W.-D. Münz [12–14] have brought magnetron sputtering technology from its earliest days to its current status as a widely used deposition approach in materials science and industrial manufacturing.

While PVD sputtering is well known for its applicability to various fields of research in materials science and engineering, the technique has become famous for depositing a variety of ceramic coatings. Particularly in applications demanding superior durability and performance, transition metal nitride hard coatings such as Ti–Al–N [14], Al–Cr–N [15], or Ti–C–N [16] have emerged as a vital subset, renowned for their exceptional hardness, wear and oxidation resistance [17,18]. Mainly, titanium nitride (TiN) stands out as a first-generation hard coating that has evolved immensely from its initial use as a protective layer for cutting tools in the mid-20th century to become one of the most prominent and widely used (and studied) coating systems in the industry (and science), due to its exceptional range of beneficial functionalities [19]. In the 1990s, with the work of W. Gissler [20], titanium boron nitride (Ti–B–N) coatings have gained recognition for their improved wear resistance and high-temperature stability (~600-800°C) compared to TiN [citation]. Following the work of C. Mitterer and P. H. Mayrhofer [21–23], nanocrystalline TiN+TiB_2 thin films became popular in the 2000's due to their inherent superhardness (> 40 GPa) [citation]. While the addition of boron (B) can significantly improve the mechanical properties of TiN-based coatings, achieving its full incorporation in the face-centered cubic (fcc) lattice is challenging. To understand this less studied limitation, the effect of variations in chemical composition along either the TiN–TiB_2 or TiN–TiB tie line on the solubility of B in the fcc-TiN lattice was investigated in this thesis (Chapter 5). Building on this research, this thesis further addresses the confined spatial conditions for B at the non-metal sublattice that inhibit the formation of the fcc-Ti(N,B) solid solution (Chapter 6).

Although the development of new synthesis strategies for ceramic thin films is a driving force in the field of surface and coating technology, careful evaluation and testing are critical to understanding and guaranteeing the target material properties. However, measuring the mechanical elastic properties of ceramic thin films, such as Young's modulus, E, and Poisson ratio, ν, is challenging. Despite recent advances in high throughput computing, theoretical models do not fully account for the complexity of thin film coatings. This thesis builds upon recent advances in in situ micromechanical testing and synchrotron X-ray diffraction to propose a novel methodology for accurately measuring direction-dependent elastic constants in ceramic hard coatings, using $TiN_{0.8}B_{0.2}$ thin films as model material (Chapter 7).

2 Alloy Design of TiN-based Coatings

In the crystal structure of titanium nitride (TiN), titanium (Ti) and nitrogen (N) atoms form a face-centered cubic (fcc) lattice within the unit cell, corresponding to the space group $Fm\bar{3}m$ (space group number 225). Based on its crystal, fcc-TiN can be further described as an interstitial compound or a *Hägg phase*, derived from the principles of intermetallic solid solutions established by Swedish chemist Gunnar Hägg in 1929. Hägg's rule guides the arrangement of smaller non-metal atoms (e.g., H, B, C, N, or P) within the interstitials of the transition metal-sublattice based on the ratio of the radius of the non-metal atom, r_x, to the radius of the metal atom, r_{Me}. In TiN, the smaller N atoms occupy the octahedral sites within the closely packed arrangement of larger Ti atoms (see Fig. 2.1), characteristic of interstitial compounds that obey the rule of

$$0.41 \leq \frac{r_x}{r_{Me}} \leq 0.59 \tag{2.1}$$

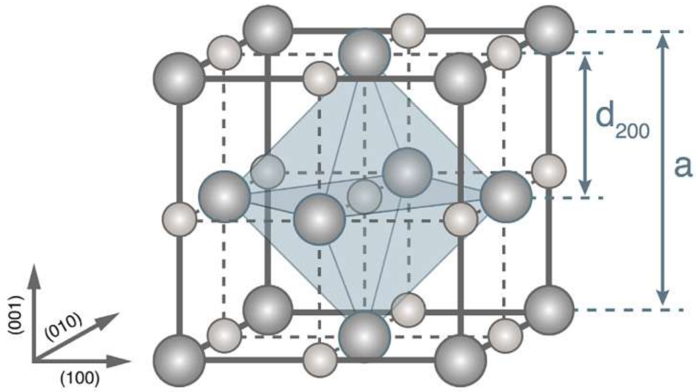

Figure 2.1. Illustration of a face-centered cubic titanium nitride unit cell, containing four Ti (dark gray) and four N (light gray) atoms: One-eighth of a Ti atom at each of the corner $\left(8 \cdot \frac{1}{8} = 1\right)$, one-half of a Ti atom on each of the six faces, $\left(6 \cdot \frac{1}{2} = 3\right)$, one-quarter of an N atom on each of the 12 edges, $\left(12 \cdot \frac{1}{4} = 3\right)$, and one N atom in the center. The octahedral side is indicated in blue. The lattice parameter, a, for fcc-TiN is 4.255 Å (calculated), and the lattice spacing for the {200} plane families, d_{200}, is 1.128 Å (calculated).

In the crystal structure of titanium nitride (TiN), titanium (Ti) and nitrogen (N) atoms form a face-centered cubic (fcc) lattice within the unit cell, corresponding to the space group $Fm\bar{3}m$ (space group number 225). Based on its crystal, fcc-TiN can be further described as an interstitial compound or a *Hägg phase* [24,25], derived from the principles of intermetallic solid solutions

established by Swedish chemist Gunnar Hägg in 1929. Hägg's rule guides the arrangement of smaller non-metal atoms (e.g., H, B, C, N, or P) within the interstitials of the transition metal-sublattice based on the ratio of the radius of the non-metal atom, r_x, to the radius of the metal atom, r_{Me}. In TiN, the smaller N atoms occupy the octahedral sites within the closely packed arrangement of larger Ti atoms (see Fig. 2.1), characteristic of interstitial compounds that obey the rule of

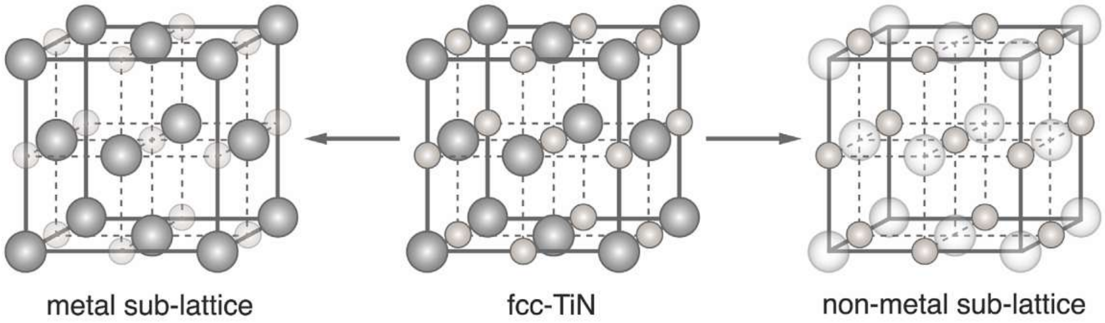

Figure 2.2. Illustration of the separation of the fcc-TiN lattice into the metal (Ti) sub-lattice (left) and the non-metal (N) sub-lattice (right). The larger Ti atoms are shown as dark gray spheres, while the light gray ones depict the smaller non-metal N atoms. This division allows for a more systematic approach to the alloy design of fcc-TiN-based coatings.

The concept of alloying beneficial elements is central to the success of modern thin film materials science [26]. A notable example of successful alloy design involves the incorporation of aluminum (Al) into fcc-TiN using PVD sputtering to form fcc-(Ti,Al)N coatings, where Al substitutes of Ti on the metal sublattice. The significant advantages of Al-incorporation are twofold. 1) Al forms a protective oxide layer on the surface of TiAlN coatings, enhancing their resistance to oxidation at elevated temperatures. 2) In thermodynamic equilibrium, AlN crystalizes in the hexagonal wurzite (WZ) structure, corresponding to the $P6_3mc$ space group (space group number 186). Nevertheless, the kinetic advantages of PVD sputtering can metastably incorporate ~80 at.% Al into fcc-metal-sublattice [27]. Compared to the hexagonal WZ structure, such as AlN, the higher packing density of the fcc structure further improves mechanical properties, such as hardness and wear resistance. However, exceeding this limit ultimately results in the formation of hexagonal (Al,Ti)N and a subsequent decline in mechanical properties [28]. Figure 2.3a shows that depending on the deposition temperature and concentration (corresponding to the free energy curves in Fig. 2.3b), the expected structure of Ti–Al–N thin films after PVD deposition is either the single-phase fcc or the single-phase hexagonal (WZ) solid solution (or two solid phases) [29]. High-temperature treatments (~700 °C) facilitate spinodal decomposition in fcc-(Ti,Al)N [30]. At the onset, coherent cubic-phase domains of AlN form (two co-existing solid phases). The mismatch in lattice parameters, a, between fcc-TiN (a=4.255 Å, calculated) and fcc-AlN (a=4.07 Å [31]) induces strain fields, leading to increased hardness (age-hardening). As the decomposition progresses, fcc-AlN transitions to its stable hexagonal (WZ) structure, eventually comprising the advantageous mechanical properties of fcc-(Ti,Al)N thin films.

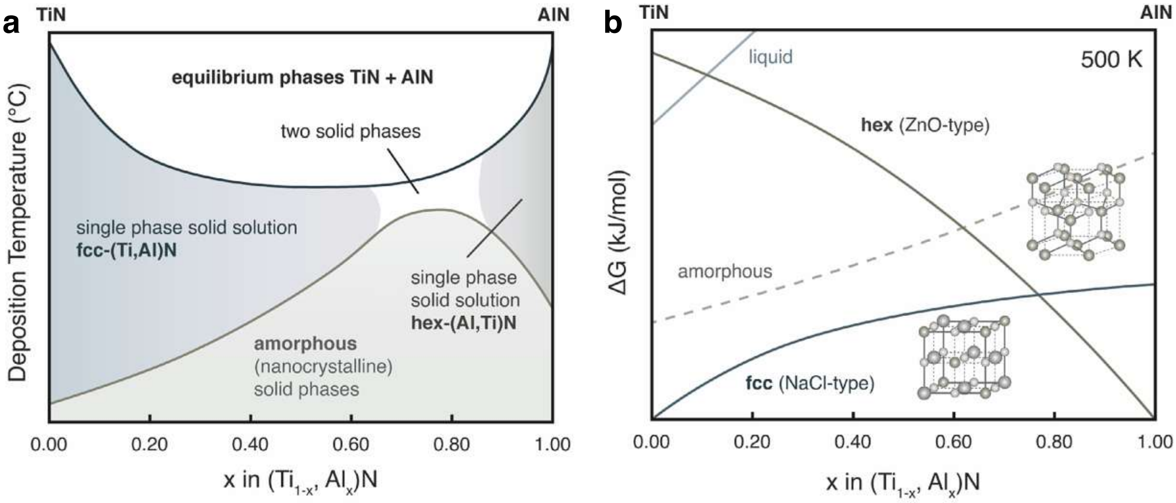

Figure 2.3. (a) Schematic PVD phase diagram and for the TiN–AlN system, showing the wide concentration range of the metastable fcc-(Ti,Al)N solid solution obtained by PVD sputtering modified after H. Holleck [29]. (b) Graphical representation of the calculated free formation energies according to [29] (normalized to $\Delta G = 0\ \mathrm{kJmol}^{-1}$ for the stable equilibrium fcc-TiN and hexagonal (WZ)-AlN phases) for amorphous, liquid, fcc, and hexagonal (WZ) phases in the TiN–AlN system at 500 K.

2.1 Ti–B–N Thin Films

Unlike PVD sputtered ternary transition metal nitride coatings like fcc-(Ti,Al)N, fcc-(Al,Cr)N or fcc-Ti(N,C), Ti–B–N thin films commonly exist as TiN+TiB_2 nanocomposites or feature second (amorphous) B-rich grain boundary phases instead of being present as an fcc solid solution [17]. Ti–B–N coatings can be prepared by various deposition approaches, including chemical vapor deposition (CVD) [32], plasma-assisted CVD [33], cathodic arc deposition (Arc-PVD) [34], and PVD sputtering (or co-sputtering), either reactive or non-reactive [35]. In addition, several other techniques have been applied in the past, such as Ti^+ ion implantation into hexagonal boron nitride (BN) thin films [36] or interdiffusion of Ti/BN multilayers [37]. In 1994, W. Gissler [20] pointed out that all structural data obtained so far for Ti–B–N thin films correspond to different combinations of co-existing (binary) phases (corresponding to the calculated ternary phase diagram for 1500°C by [38] in Fig. 2.4) and show no evidence for a ternary fcc-Ti(N,B) solid solution. He further concluded that only a small solubility of B is possible in the fcc-TiN lattice (and a negligibly small solubility (<1 at.%) of N in the hexagonal close-packed (hcp) TiB_2 lattice), raising the question of a potential extension of the solubility limit of the ternary fcc-Ti(N,B) phase.

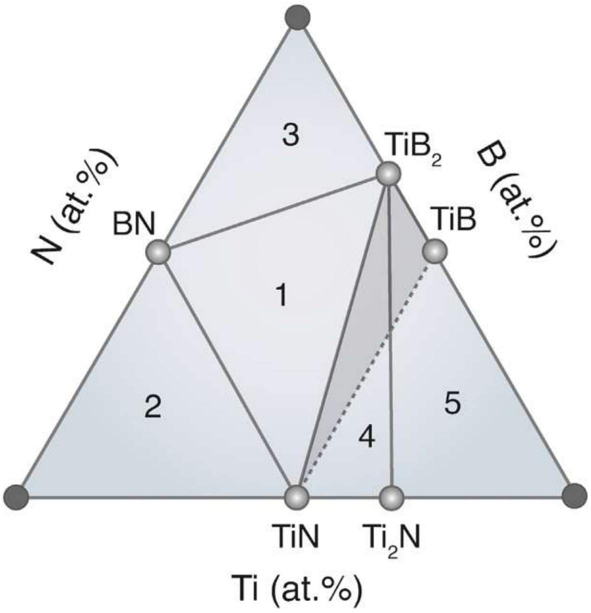

Figure 2.4. Simplified ternary phase diagram of Ti–B–N, modified after H. Novotny [38] and W. Gissler [20], at 1500 °C, divided into five distinct zones, labeled 1–5, corresponding to different combinations of co-existing phases. 1. TiB_2+TiN+BN, 2. TiN+BN+N_2, 3. TiB_2+B+BN, 4. $Ti(N,B)_{1-x}$, 5. Ti(ss)+TiB_2. The gray shaded area represents the TiN–TiB_2–TiB phase field of interest in this thesis.

X-ray diffraction analysis of the fcc-TiN (and hcp-TiB_2) phase(s) showed that with increasing B (or N) content, the diffraction peaks become broader until an amorphous-like pattern appears, which is mainly attributed to the formation of progressively smaller grains [20,23]. P.H. Mayrhofer [39] explained this grain refinement phenomenon as the result of segregation-driven renucleation processes, supported by Transmission Electron Microscopy (TEM) investigations, revealing the relatively randomly oriented nanocrystalline microstructure of as-deposited Ti–B–N thin films with high B concentrations (±30 at.%). Thermodynamically, the phase separation of fcc-TiN and hcp-TiB_2 is favored by a large miscibility gap observed in the equilibrium Ti–B–N phase diagram. Ti, N, and B atoms condense at the substrate surface during the deposition process and spontaneously nucleate. Surplus B segregates at the nucleation surfaces, forming disordered B-rich regions that encapsulate the growing crystallites. As a result, grain coarsening during coalescence is suppressed, initiating a continuous nucleation-segregation process that hinders subsequent grain growth (see Fig. 2.5): The B-enriched regions covering the TiN crystallites promote the formation of TiB_2 nuclei (favored by the extremely low solubility limit for N in TiB_2). Renucleation of TiB_2 is again inhibited as excess N and B continue to segregate to the surfaces of the TiB_2 crystallites, forming regions of h-BN_x that cover the TiB_2 grains and promote renucleation of TiN crystallites [39]. The resulting coating exhibited a randomly oriented arrangement of nanocrystalline TiN and TiB_2 grains (2-3 nm) enclosed by a high volume fraction of a (softer) disordered (BTi_yN_x) phase. Although the TiN+TiB_2 as-deposited thin films exhibited a remarkable nanoindentation hardness (H=37 GPa), the best performance of the nanocrystalline TiN+TiB_2 coatings occurred when the disordered phase decreased during the annealing process (43 GPa at 800 °C).

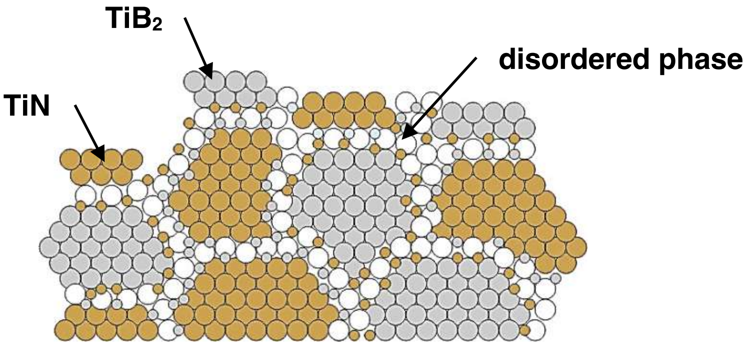

Figure 2.5. A schematic cross-sectional view of a nanocrystalline Ti–B–N thin film illustrates the segregation-driven renucleation of TiN and TiB_2 crystallites during film growth. In accordance with permission granted by P.H. Mayrhofer this figure has been reproduced from [39]

Comparing the chemical composition of previously studied Ti–B–N coatings within the corresponding ternary phase diagram, it is observed that hard (and superhard coatings, H > 40 GPa) are distributed along the TiN–TiB_2 or TiN–TiB tie lines [35]. Conversely, the softer Ti–B–N coatings found along the TiN–BN or the TiB_2–BN tie lines, centered within the TiN–BN–TiB_2 phase field, or closer to BN [35]. Although B alloying can significantly improve the mechanical properties (e.g., hardness, wear resistance, and thermal stability) of TiN-based coatings, achieving complete B solubility in the fcc-TiN lattice is challenging and less studied. Incorporation of B induces significant lattice distortions and increases the fcc-TiN lattice parameter, a=4.255 Å (calculated), due to the slightly larger covalent radius of B (0.84 Å) [40] compared to N (0.71 Å) [40]; as B replaces N in the fcc-TiN non-meal sublattice.

Instead of fully achieving the desired effect of solid solution hardening when B is added, forming an fcc-Ti(N,B) solid solution is somewhat limited due to the segregation of B at the grain boundaries of the fcc-TiN crystallites during nucleation. Excess B forms secondary amorphous B-rich grain phases or promotes the nucleation of nanocrystalline TiB_2 grains alongside TiN, as previously described. Thus, most of PVD sputtered Ti–B–N coatings exhibit nanocrystalline morphology rather than the pronounced columnar growth commonly observed in PVD thin films, i.e., grain refinement strengthening [41,42].

However, a decrease in hardness, H<30 GPa, in Ti–B–N thin films (compared to fcc-TiN) is mainly caused by the formation of secondary soft Ti or (amorphous) BN-rich grain boundary phases, the latter often observed when using reactive PVD sputtering. R. Hahn [35] has shown that the B content and the deposition route—comparing reactive and non-reactive DC magnetron sputtering—influence the phase formation and the resulting mechanical properties in PVD sputtered Ti–B–N coatings. Plasma analysis supported by mass spectrometry and X-ray photoelectron spectroscopy (XPS) revealed significant differences between the two deposition approaches. Due to the deficient $N^+/(N^++N_2^+)$ ratio during reactive sputtering (compared to non-reactive sputtering) and the oversupply of N_2, reactively deposited Ti–B–N coatings typically result in a chemical composition distributed along the TiN–BN tie line. In contrast, non-reactive sputtering allows chemistries to follow the TiN–TiB_2 line. These differences extend to the microstructural level, where non-reactively deposited Ti–B–N thin films generally exhibit increased hardness, H, Young's modulus, E, and fracture toughness, K_{IC}, compared to reactively sputtered ones. However, the performance of reactive sputtered Ti–B–N coatings is optimized when soft (amorphous) BN-rich phases exist between coexisting TiB_2 and TiN nano-crystallites in ~equal proportions (as previously mentioned in the text).

Previous studies have extensively studied the ternary phase system of Ti–B–N coatings, offering valuable insights into the influence of B on the microstructure and mechanical properties of TiN-based coatings. PVD sputtered Ti–B–N thin films typically exist as nanocomposites of TiN+TiB_2 and/or exhibit amorphous B-rich grain boundary phases rather than forming a single fcc-Ti(N,B) solid solution, caused by the limited solubility of B in the fcc-TiN lattice. High B content leads to smaller grains and the formation of disordered BN-rich regions that encapsulate the TiN and TiB_2 crystallites or if less (amorphous) B accumulates at the TiN grain boundaries. In both cases, segregation-driven processes inhibit coalescence and grain coarsening. Non-reactive sputtering generally results in Ti–B–N coatings with improved mechanical properties compared to fcc-TiN or reactive sputtering. This thesis investigates the less studied solubility of B in TiN-based thin films and its effects on mechanical properties. Examining chemistries along the TiN–TiB_2 and TiN–TiB tie-lines show that ~10 at.% B can be fully incorporated into the fcc-TiN lattice without forming other B-containing (amorphous) phases, significantly outperforming the hardness, H, and fracture toughness, K_{IC}, of fcc-TiN. Assisted by ab initio calculations, the significance of the spatial requirements for fully incorporating B within the fcc-TiN lattice is highlighted.

2.2 Phase Formation and Stability in Solid Solutions

Given that most materials of interest in materials science exist in a crystalline solid phase, a homogeneous mixture of one or more elements (e.g., B) within the crystal lattice of another material (e.g., fcc-TiN) is defined as a *solid solution* [43]. The term "solution" implies that the added components are dispersed at the atomic level within the lattice. The solubility of the element can vary from near insolubility, where the added element is minimally able to mix with the host lattice, to full miscibility, where the added element can disperse uniformly throughout the entire concentration range.

Understanding phase formation and stability in solid solutions is critical to the design of materials with desired properties. The Gibbs Phase Rule proposed by J.W. Gibbs in 1876 [44] is fundamental in predicting the number of phases that can coexist in equilibrium. For binary systems, the number of phases, P, in equilibrium is given by

$$f = n - P + 2 \tag{2.2}$$

where n is the number of components and f denotes the degrees of freedom (e.g., temperature, T, pressure, p, or composition, x. A *component* is defined as a chemically distinct species or element that cannot be broken down into simpler parts. For example, studying the phase formation of Ti–B–N thin films n depends on whether the system is considered a quasi-binary system (TiN+TiB_2 or TiN+TiB) or a ternary system (Ti+B+N). Their Gibbs free energy, G, determines the thermodynamic stability of these phases,

$$G = H - TS \tag{2.3}$$

combining enthalpy, H, and entropy, S. In thermodynamic equilibrium, the state of minimum Gibbs free energy, represents the most stable configuration of the material system, i.e., at a fixed temperature, T, and constant pressure, p, the system will tend to adjust its composition or phase structure to minimize its Gibbs free energy $G \rightarrow G_{min}$. When forming a solid solution (e.g., TiN+TiB_2), ΔG_{mix} refers to the Gibbs free energy of mixing,

$$\Delta G_{mix} = \Delta H_{mix} - T\Delta S_{mix} \tag{2.4}$$

where ΔH_{mix}, is the mixing enthalpy and ΔS_{mix} is the mixing entropy. For a single pure element (with respect to decomposition to the same pure element) ΔG_{mix} is typically considered to be zero. A negative ΔG_{mix} value indicates that the mixed state (i.e., the solid solution) is energetically more favorable than its constituents.

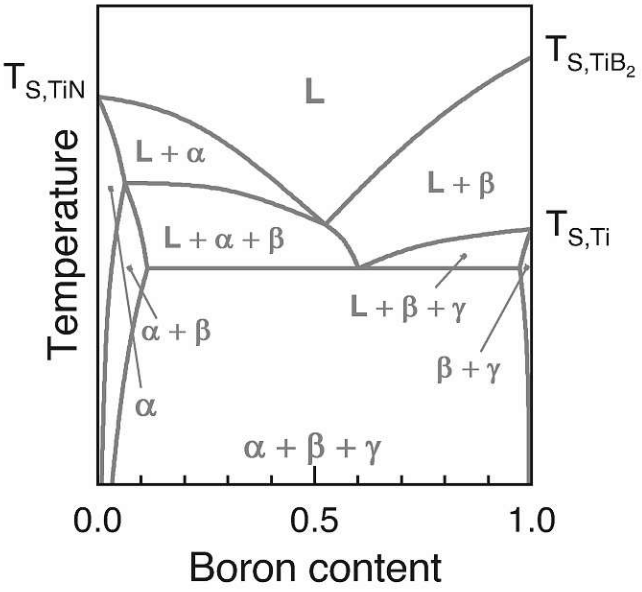

Figure 2.6. Schematic quasi-binary phase diagram along the TiN–TiB tie line in the Ti–B–N ternary phase diagram of interest in this thesis. The α-phase is representative for fcc-TiN, the β-phase is hcp-TiB_2, and the γ-Phase is hcp-Ti. T_S indicates the melting temperature for fcc-TiN, hcp-TiB_2, and hcp-Ti, respectively and L is the liquid phase field. The B concentration increases from left to right while the N concentration decreases.

Phase diagrams provide a graphical representation of the equilibrium phases in a material system (see in Fig. 2.6. an example for a quasi-binary phase diagram in the Ti–B–N system). In a typical binary phase diagram, the regions depict the stable phases as a function of temperature, pressure (y-axis) and chemical composition (x-axis) [43]. Each phase can be associated with an energy of formation, ΔE_f, quantifying the energy change when the phase is formed from its constituents. ΔE_f can be either negative or positive, depending on whether the phase formation gains or costs energy. To interpret the thermodynamic phase stability of a (ternary) material system, the ΔE_f of all possible combinations of phases must be considered [45–47]. The convex hull connects the points in the phase diagram with the lowest-energy state. Any composition that lies directly on the convex hull is considered thermodynamically stable under the given conditions, while less energetically favorable compositions represent metastable states. Even when the structural arrangements are not aligned with the lowest-energy states—akin to points above the convex hull—metastable solid solutions may persist due to kinetic barriers that impede their transition to the thermodynamically stable configuration.

2.3 Hume-Rothery Rules

If the mixing of atoms from components A and B decreases the system's overall energy, ΔG_{mix}<0, indicating that the process is energetically favorable. This typically occurs when A and B have similar sizes and chemical properties, allowing them to mix uniformly within the crystal lattice without significant strain or disruption. The arrangement of A and B determines the type of solid solution that forms. There are two main types [43]: 1. interstitial solid solutions or 2. substitutional solid substitutions. In interstitial solid solutions, the alloyed atoms occupy the interstitial sites of the host lattice. This arrangement is only feasible for atoms with small atomic radii, such as H, B, C, and N. As the interstitial sides are—nevertheless—too small, the incorporation of atoms causes elastic lattice distortions, leading to an (energetically unfavorable) increase in G. Consequently, the solubility limit is reduced, promoting the formation of other (secondary) phases. Most binary systems form substitutional solid solutions where A replaces B in the lattice. While some material systems exhibit unlimited solubility over the entire concentration range. However, many multi-component systems also show a miscibility gap, where solubility is limited at specific compositions and the system separates into two phases. This limitation occurs whenever A and B crystallize in different lattices.

The ability to form a substitutional solid solution is governed by the Hume-Rothery rules [48,49]: i) The atomic radii of the solvent and solute atoms should be similar (with a size ratio >15%). ii) The electronegativities of the atoms of the solvent and of the solute should be similar. iii) The number of valence electrons per atom (valence electron concentration) should be similar for solvent and solute elements. For an interstitial solid solution this rule applies if the solute has a radius less than 59% of the solvent. In the case of a significant difference in atomic size between A and B, the elastic energy required to incorporate A into the lattice of B is increased, making the formation of a substitutional solid solution less energetically favorable. As the electronegativity difference between A and B becomes larger, the formation of stoichiometric intermetallic phases is favored. Intermetallic phases typically form when the elements involved have significantly different electronegativities and exhibit strong chemical bonding and high thermodynamic stability. Consequently, the formation of such stable intermediate phases limits the solubility of the alloying elements within the solid solution. In practice, it is often observed that elements with a higher number of valence electrons have lower solubility than those with fewer valence electrons. According to the Pauli exclusion principle of quantum theory, an electron, a fermion (a particle with a half-integer spin), cannot occupy the same quantum state as the other electron and must, therefore, "stack" within an atom. Once the critical valence electron density (number of valence electrons per atom) is reached in crystalline materials, the energy required to accommodate additional electrons increases significantly. However, this critical valence electron density varies depending on the crystal structure; for example, it is higher in the body-centered cubic (bcc) lattice than in the fcc lattice. Consequently, when the critical valence electron concentration (VEC) is reached in an fcc solid solution by adding an atom with a high number of valence electrons, the bcc structure becomes energetically favored and more stable than the fcc structure as the alloying concentration is further increased.

3 Physical Vapor Deposition

Physical Vapor Deposition (PVD) refers to processes that specialize in depositing thin films on surfaces to be modified [50]. Operating solely on physical mechanisms, PVD methods involve first transferring the target material into the gas phase. Subsequently, the vaporized target species are transported through a vacuum process chamber and deposited onto a substrate surface through condensation, where nucleation and film growth commence. The vaporization of the target material distinguishes between different PVD processes, including thermal energy supply and sputtering, the latter achieved by bombarding the target surface with ions of process gas accelerated in an electric field. PVD sputtering is a versatile and highly beneficial technique in materials science and design, offering numerous advantages for creating thin film materials with outstanding properties, often surpassing those of bulk materials. One of the most significant advantages of PVD sputtering is its compositional versatility. By depositing coatings from atoms or ions in the gas phase, PVD allows for the formation of thin films with diverse compositions and structures. This versatility 1. enables the deposition of coatings made from a wide range of materials, including metals, alloys, borides, nitrides, oxides, and carbides, 2. provides flexibility in materials selection for specific applications, including protective coatings for tools (e.g., TiN, CrN, TiAlN), conductive or insulating coatings in microelectronics (e.g., TiN, Al, SiO_2), and applications in the automotive industry, microelectronics, and optical and decorative purposes [51]. Unlike traditional synthesis routes driven by equilibrium thermodynamics, PVD operates at the intersection of rapid kinetics and controlled deposition conditions. By subjecting materials to high cooling rates during deposition, PVD overcomes thermodynamic constraints and enables kinetic control of phase formation and stabilization [52].

3.1 The Principle of Sputtering

Plasma-assisted sputtering takes place within an evacuated chamber, typically maintained at pressures ranging from 0.1 to 5 Pa. In a low-pressure environment such as a vacuum chamber, the mean free path, λ, of the sputtered species—the average distance they can travel before colliding with another particle—is significantly extended to a few millimeters, facilitating a uniform and controlled deposition process. The mean free path, λ, of an atom with radius, r, at a given pressure, p, can be calculated from

$$\lambda = \frac{k}{\sqrt{2}\pi 4 r^2 p} \tag{3.1}$$

Inside the vacuum chamber, two electrodes (cathode and anode) are arranged with a specific distance, d, between them, where the cathode contains the target material to be atomized and the anode holds the substrate on which the material will be deposited. Prior to initiating the sputter process, an inert working gas, typically argon (Ar), is injected into the evacuated chamber. to 1. provide a medium for transferring energy within the electric field to the cathode, 2. maintain the plasma discharge, and 3. facilitate the transport of sputtered atoms or molecules to the substrate [2,52]. When a high electric field is applied between the electrodes the Ar atoms within the chamber become ionized, generating a plasma by glow discharge. The positively charged Ar^+ ions in the plasma are accelerated toward the target surface and collide with the target material. At the moment of impact, the Ar^+ ions transfer their momentum to the atoms near the target surface. In inelastic collisions, secondary electrons are emitted, whereas in elastic collisions, the target atoms transfer momentum to adjacent atoms. These subsequent collisions propagate through the material (i.e., collision cascade), causing atoms to be ejected from the target surface. This high-energy bombardment heats the target material, with ~95% of the collision energy being converted into heat. To prevent damage to the cathode and to limit chemical reactions and/or thermal expansion of the target material, the cathodes is equipped with a cooling water system.

After ejection, the released atoms are transferred to the gas phase and arrive at the substrate surface at a specific angle and with some loss of initial energy, following a collision-induced trajectory. The incoming atoms condense on the substrate, leading to film growth driven by surface diffusion and nucleation processes. If all components are obtained by evaporation of a condensed phase (i.e., compound target) in an inert working gas atmosphere, these processes are referred to as *non-reactive*. If one or more components of a composite coating are additionally introduced into the PVD chamber via a reactive gas (e.g., N_2, O_2, C_2H_2), these processes are referred to as *reactive*. Fig. 3.1 provides a detailed overview of the basic principles of sputtering and illustrates the various processes involved. The reactive sputtering process is controlled by adjusting the partial pressure of the reactive gas and the power applied to the metallic target.

Insufficient diffusion on the surface and at the grain boundaries, together with atomic shading effects, may cause defects such as pores or tensile stresses and increased surface roughness, which can significantly affect the quality of the coating. The deposition process can be improved by substrate rotation, substrate heating, and substrate bias voltage. Substrate rotation ensures uniform deposition conditions and film thickness, limiting atomic shadowing effects [3]. Substrate heating increases the adatom mobility, resulting in a denser microstructure and better substrate adhesion. The application of a negative potential (bias voltage) across the anode facilitates the bombardment of the target surface by positive Ar^+ ions (similar to the ion bombardment of the target). The energy of the bombarding ions can be controlled by adjusting the voltage, to enhances the surface mobility and film growth morphology (e.g., grain size), to reduce residual stresses, and to vary the composition [3]. Controlling (and adjusting) deposition parameters such as target power, gas flow rates, and substrate temperature is paramount to produce high-quality, uniform films with desired properties tailored for various applications, such as wear-resistant coatings or decorative finishes.

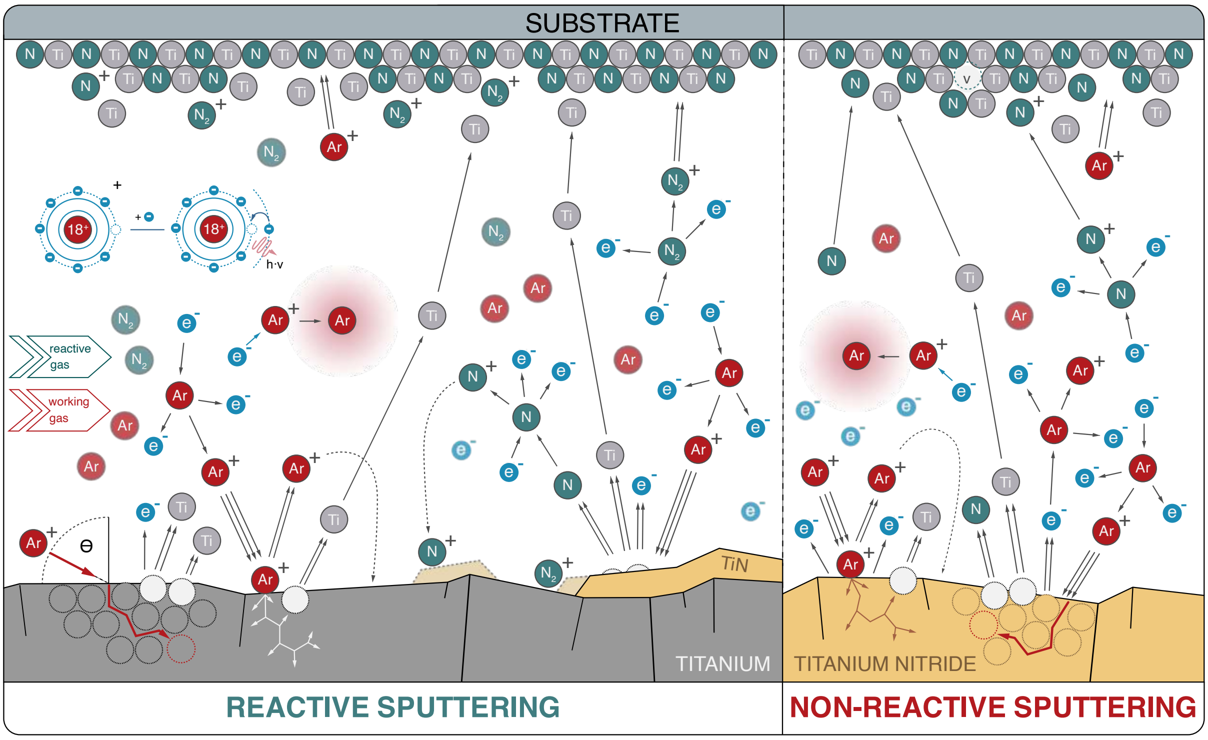

Figure 3.1. The basic principles of reactive (left) and non-reactive (right) sputtering are illustrated by the formation of fcc-TiN, summarized from the lectures in *Surface Technology* given by P.H. Mayrhofer [1].

In non-reactive DC sputter deposition, a compound target material such as TiN is bombarded with high-energy ions from a plasma, typically generated by applying a direct current (DC) voltage to an inert gas such as Ar. The Ar^+ ions collide with the TiN target, causing Ti and N atoms to escape (i.e., sputtered) from the target surface. These sputtered Ti and N atoms then travel through the vacuum chamber and are deposited on the substrate, forming am fcc-TiN thin film. Reactive sputtering is a similar process, but a reactive gas, such as N_2, is added to the inert working gas. As Ti atoms are sputtered from the metallic Ti target, they react with the N_2^+ ions in the plasma and form as fcc-TiN compound on the substrate. However, these reactive gas species can also undergo chemical reactions with the target material (i.e., target poisoning). Target poisoning scientifically impact on the sputtering process, especially when depositing insulating films (e.g., AlN, Al_2O_3)

[citation]. In such cases, the buildup of reaction products on the target surface (see Fig. 3.1) can alter its conductivity and interfere with the sputtering process (e.g., deposition rate). Understanding and mitigating the effects of this phenomenon is often accomplished by recording hysteresis curves [citation]. However, schieving a stable process for non-reactively depositing insulating compounds (e.g., BN, AlN, Al_2O_3) using DC power is not possible and requires pulsed DC modes. Key parameters for controlling pulsed DC sputtering include the pulse frequency, f, in kHz and the pulse width, t_{on}, typically in µs. The pulse duty cycle, D, defines the ratio of the pulse on time, t_{on}, to the total pulse period (t_{on}+ t_{off}). The effective power delivered to the target during each pulse period depends on the voltage applied to the target, V, the duty cycle D, and the pulse frequency, f. While it is possible to sputter non-conductive targets with high-end generators operating in pulsed mode, these processes typically yield very low sputtering rates compared to conventional DC sputtering. Additionally, they often require higher process gas pressures to maintain the plasma. Therefore, only thin films with final thicknesses of a few hundred nanometers can be achieved within a reasonable deposition time. These deposited coatings are predominantly amorphous, with properties (such as hardness) significantly lower than expected if they were cubic crystalline.

3.2 Sputter Yield

Sputter yield, S_a, is defined as the average number of atoms removed from the target surface per incident ion (S_a≈1–3) and reflects how effectively target atoms are ejected when bombarded by impinging ions. A higher sputter yield means that material is more efficiently removed from the target, resulting in a faster deposition rate. S_a can be expressed as [52,53]

$$S_a = \frac{3}{4\pi^2} \cdot \alpha_s \cdot \frac{4 \cdot m_i \cdot m_c}{(m_i + m_c)^2} \cdot \frac{E_i}{U_o} \qquad (3.2)$$

and therefore increases to a limited extent with increasing energy of the incident ions, E_i, which in turn depends on the applied power to the sputter target and the process pressure. A high processes pressure reduces the kinetic energy of the charged species due to more frequent collision events. If E_i exceeds a specific threshold and the incident ions penetrate deeper into the target material, most of E_i is spent for penetration rather than being transferred to the target atoms. When the momentum/energy transfer becomes less than the surface binding energy, U_o, (i.e., the energy threshold that must be overcome to release an atom from the top surface layer in vacuum during the sputtering process), then S_a rapidly decreases [54]. However, lowering the working gas pressures decreases the number of electrons and ions available for bombardment or impact ionization. α_s represents the sputtering yield coefficient and depends on the incident angle, Θ, of the Ar$^+$ ions normal to the target surface (see Fig. 3.1). S_a typically increases up to an angle of ~60—70 degrees [52]. At grazing angles, the ions are more likely to glance off the target surface without causing significant sputtering. In collisions between incident ions and target atoms, the energy transfer is more efficient when if the mass of the ion, m_i, is equal to the mass of the target atom, m_c. The mass effect on S_a is therefore at its maximum when m_i=m_c [53].

3.3 DC Unbalanced Magnetron Sputtering

Magnetrons provided a breakthrough solution to the sputtering rate limitations of diode sputtering. The principle of direct current (DC) Magnetron sputtering is based on confining electrons near the target surface using a combination of electric, $\boldsymbol{E}$, and magnetic fields, $\boldsymbol{B}$. The (unbalanced) magnetron shown in Fig. 3.2 is equipped with a central magnet (S-pole) positioned below the target. This central magnet is surrounded by magnets of opposite polarity (N-pole). This configuration generates arc-shaped magnetic field lines on the surface as current flows through the target. The DC power source maintains a stable potential difference between the target material (cathode) and the substrate (anode), accelerating the positively charged process gas ions towards the target surface for sputtering [52,53].

The orthogonal alignment of $\boldsymbol{E}$ and $\boldsymbol{B}$ induces an $\boldsymbol{E}\times\boldsymbol{B}$ drift that forces the sputtered secondary electrons to a two-dimensional, helical trajectory parallel to the target surface and perpendicular to the magnetic field lines (Lorentz force). The electrons are subsequently accelerated toward the anode due to the high electric field strength. In the region near the edge of the negative glow region, the electric field strength decreases. If the magnetic field lines are perpendicular to the electric field, $\boldsymbol{E}$, in this region, the resulting Lorentz force, $\boldsymbol{F}$

$$\boldsymbol{F} = q(\boldsymbol{E} + \boldsymbol{v} \times \boldsymbol{B}) \tag{3.3}$$

causes the electrons with charge, q, and velocity, $\boldsymbol{v}$, to follow an arcuate path back to the target surface and to be accelerated again toward the anode.

An electron can break free from its orbit by impact ionization, i.e., collision with an process gas atom (e.g., Ar) at the edge of the negative glow region [52,53]. Concentrated in this region, the ionized Ar+ ions rapidly move to the target surface forced by the electric field, $\boldsymbol{E}$, and deplete the target material along a defined erosion profile, technically known as racetrack .

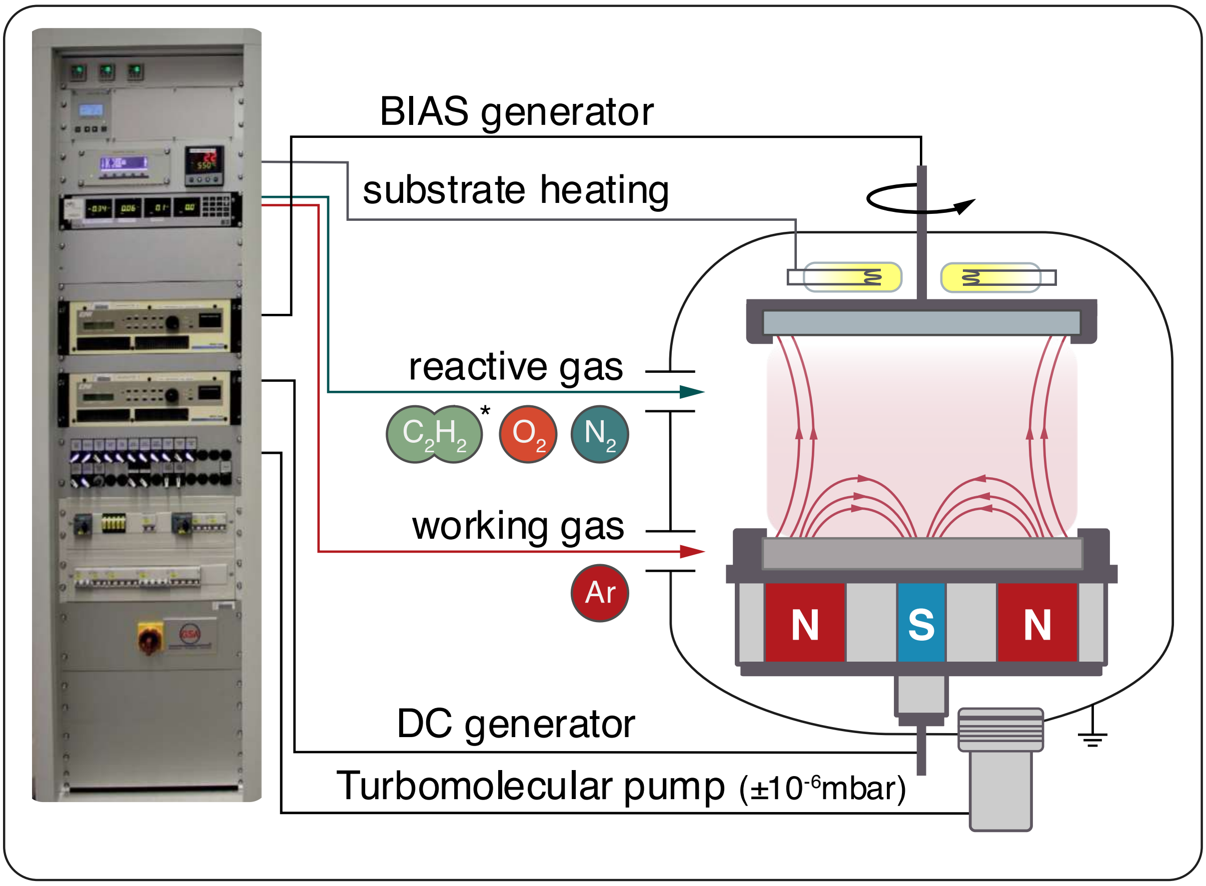

Figure 3.2. Illustration of the unbalanced magnetron sputtering system similar to the machine "Ylvi" used in this thesis for the deposition of various Ti–B–N thin films. The setup includes a switch box (on the left side) to control 1. the deposition parameters (e.g., sputter mode: DC or pulsed DC, target current, substrate bias, temperature), 2. the vacuum system (including a rotary vane pump for pre-vacuum and a turbomolecular pump for reaching high vacuum conditions), and gas mass flow controls for the working and reactive gases during sputtering. *Notably, the supply of acetylene gas, C_2H_2, requires additional safety adjustments.

The advantage of using a magnetron assembly in PVD sputtering is twofold: it traps the electrons close to the target surface, and it increases the number of secondary electrons available to ionize the process gas, thus requiring less Ar atoms (i.e., lower process gas pressure) to sustain the plasma. As a result, the vaporized target atoms experience fewer collisions, i.e., more energetic target atoms condense on the substrate surface, positively impacting both the deposition rate and the density of the deposited thin film.

4 Thin Film Characterization

Modern high-performance coatings are constantly opening up new areas of application with ever-increasing requirements, thus necessitating a comprehensive analysis of their material properties. The characterization of thin film materials is therefore one of the main tasks—common to all fields of materials science—providing valuable insights into the structure, composition and (mechanical) properties of a layered material, which is essential for targeted improvements and for making informed decisions during design, synthesis and processing. Although it is not the intention of this thesis to describe in detail all techniques and principles of thin film characterization, it should be noted that this methodology section "Thin Film Characterization" is limited to the main methods implemented in the thesis.

4.1 X-ray Diffraction

The crystalline structure of ceramic thin films is of greatest interested as in the crystal structure of a material all its properties are embedded. Since the demonstration of X-ray diffraction on crystals in 1912, this technique has become a fundamental tool in the fields of physics, crystallography, and materials science [55–57]. X-ray diffraction is a non-destructive method used to study fundamental aspects in materials science including 1. crystal structure and phase composition, 2. crystallite orientation distribution (texture), 3. orientation-dependent shape and size of coherently diffracting domains, and 4. 1st, 2nd, and 3rd order internal strains [58]. The technique is based on the interaction between short-wavelength X-rays, comparable to atomic distances within the crystal, and the electrons in the crystal lattice. For example, the effective wavelength, λ, of the copper (Cu) $K_{\alpha,\beta}$ radiation used for the laboratory X-ray diffraction experiments in this thesis is ~1.54 Å.

W.C. Röntgen discovered X-rays (“X” for unknown) in 1895 [59] and was awarded the first Nobel Prize in Physics for this discovery in 1901. X-rays can be understood as massless electromagnetic waves with wavelengths in the range of about 0.001–10 nm, propagating at the speed of light ($c \approx 3 \times 10^8$ m/s). The technically relevant energy range for X-rays is between 3 keV and 500 keV. Modern X-ray sources such as synchrotrons, which produce high-energy and high-intensity radiation, can generate X-rays with energies up to several hundred keV. Radiation generated in X-ray tubes consists of two main components: 1. characteristic X-rays and 2. bremsstrahlung. In 1911, J.E. Lilienfeld [60] developed the thermionic (hot cathode) tube technology which operates on the principle of thermionic emission and is still in use today: Electrons are emitted from a heated tungsten filament (cathode), and subsequently accelerated toward a metallic target material (anode), under the influence of an applied high voltage, typically in the kV range. Upon reaching the target, the high-speed electrons are decelerated by the strong electric field of the positively charged target nuclei. This abrupt deceleration causes the electrons to emit the energy difference in the form of high-frequency electromagnetic radiation with a continuous energy spectrum (bremsstrahlung). Some of the accelerated electrons can also knock out inner-shell electrons from the atoms of the target material. As outer-shell electrons transition to fill these vacancies, characteristic X-rays are emitted. These characteristic X-rays have discrete energies specific to the element of the target material and are used for X-ray diffraction. Notably, most of the energy produced in this process is converted into heat, highlighting the need to cool the anode during operation. In X-ray diffraction experiments, the K radiation of metals (either Cr, Fe, Co, Ni, Cu, or Mo) is typically used [61].

The X-ray beam emitted from the X-ray tube diverges; therefore, it is imperative to engineer the beam guidance system to focus partial beams. Focusing is essential for reliably observing weak and low-intensity diffraction phenomena. In numerous applications, X-rays are still detected using point detectors. All focusing techniques rely on Thales' theorem, which asserts that the apex angle remains constant in all triangles inscribed within a circle via a common secant. In the Bragg-Brentano geometry [62], in Fig. 4.1, the tube focus, sample, and detector are positioned on a focusing circle, with the radius of the circle decreasing as the diffraction angle increases. Only crystallites with lattice planes parallel to the surface meet the diffraction criterion [61].

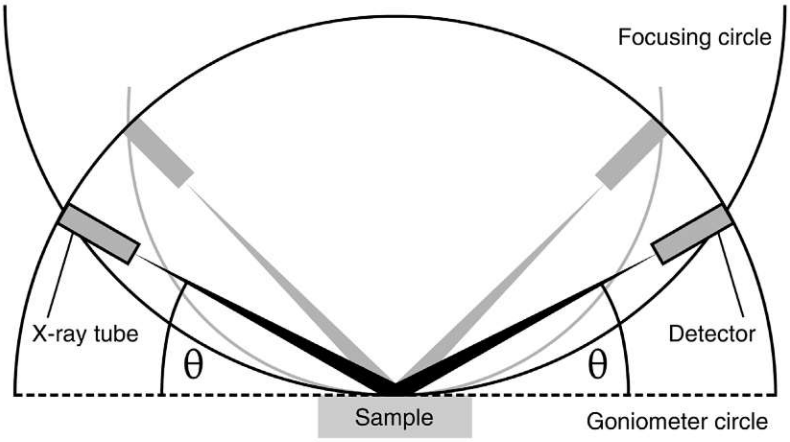

Figure 4.1. Schematic representation of the basic principle of X-ray focusing, showing the beam path for the divergent primary beam and the detector beam at two different diffraction angles, θ, in a Bragg-Brentano geometry (θ-θ goniometer). Adapted from [61]. The sample is stationary and horizontally aligned while the X-ray tube and detector move around the sample along the goniometer circle.

4.1.1 Phase Analysis

Polycrystalline thin film samples always consists of randomly oriented small crystallites, the grains. A crystallite is a small single crystal and is characterized by its orientation expressed by the Miller indices h, k, l. In the ideal polycrystalline material, all orientation vectors are statistically randomly distributed. Each crystal structure, representing a particular crystalline phase, is characterized by a unique arrangement of lattice planes with specific interatomic distances that can be examined using X-ray diffraction [63,64]. When a polycrystalline coating is subjected to a monochromatic incident X-ray beam, these lattice planes produce a series of diffraction cones. In a laboratory powder XRD setup, the arrangement of lattice plane spacings is analyzed by conducting a radial scan across the diffraction cones. This scan generates a plot of diffraction intensity, I, against the diffraction angle 2θ. Intensity peaks occur when a diffraction cone is intersected, thereby fulfilling the Bragg condition [65]

$$n\lambda = 2d_{hkl}\, sin\, \theta \tag{4.1}$$

for a specific lattice plane family, where n is the order of the diffraction peak, λ is the wavelength of the incident monochromatic X-ray beam, d_{hkl} is the lattice plane spacing, and θ is the Bragg angle (see Fig. 4.2). Another prerequisite is that the structure factor [63,64] of the lattice plane family is not equal to zero, as destructive interference can occur in specific directions. These directions (*hkl*), where this peak extinction occurs, depend on the Bravais lattice (there are 14) of the specific crystal structure.

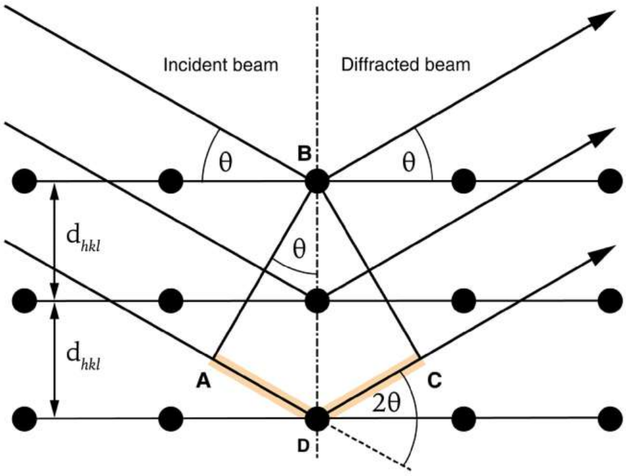

Figure 4.2. The schematically drawn Bragg condition explains how incident X-rays undergo diffraction when the difference in path lengths between waves scattered at various lattice planes is a multiple, n, of the X-ray wavelength λ, with $\overline{ADC} = 2d_{hkl}\, sin\, \theta$ (marked in orange). This condition, coupled with the structure factor, which permits constructive interference of scattered X-ray wave fronts, leads to diffraction.

The extinction rule for face-centered cubic crystals (e.g., fcc-TiN) implies that diffraction peaks are extinguished when the sum of the Miller indices h, k, l of the reflecting lattice plane distances, d_{hkl}, result in an even number, i.e., intensity peaks are observed when the sum is an odd number. This rule derives from the inherent symmetry properties of the fcc crystal structure.

4.1.2 Peak Analysis

Peak analysis serves as a valuable tool for studying the crystal structure of as-deposited polycrystalline thin films (e.g., phase transformations, defect and growth morphology, residual stresses, or texture) and structural changes induced by external treatments such as annealing, oxidation, or corrosion [61,63]. Several parameters are commonly used to characterize the intensity peaks observed in diffraction patterns, including peak position, 2θ, the intensity, I, which correlates with the number of diffracted X-rays from the crystal lattice, the width of the peak at half of its maximum intensity (FWHM), the peak geometry including shape, area and asymmetry. The most important features of the peak analysis are illustrated in Fig. 4.3.

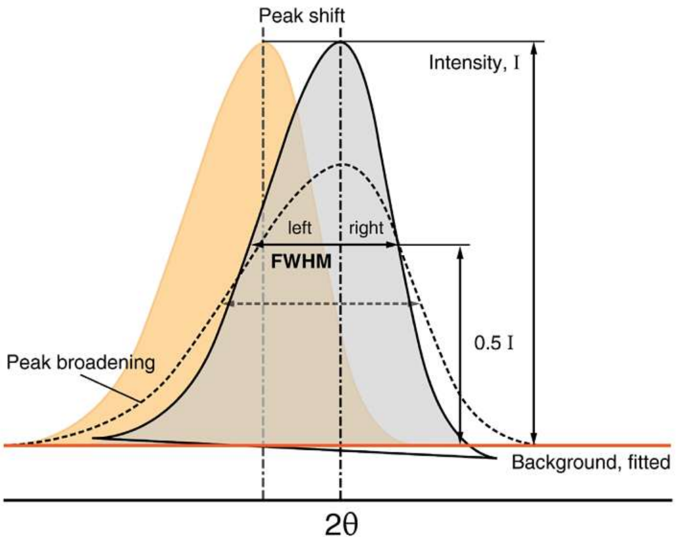

Figure 4.3. Illustration of the key parameters used for peak analysis of an XRD pattern. The peak position, 2θ, identifies the specific lattice plane distances, d_{hkl}, while the peak intensity, I, reflects the relative abundance of the crystalline. The peak shape provides insight into the microstructural properties of the sample. The Full Width at Half Maximum (FWHM) is the peak with and is measured at half the maximum peak intensity. Background Fitting adjusts for baseline noise to ensure accurate peak fitting. Peak shifts indicate changes in lattice parameters due to composition or residual stress, and peak broadening, seen as an increase in FWHM, can result from smaller crystallite sizes or increased lattice strain.

The most important features of the peak analysis are illustrated in Fig. 4.3. The initial step in analyzing diffraction patterns is background fitting, which involves subtracting the background signal from the recorded diffraction pattern to enhance the accuracy of subsequent analyses. The peaks within the diffraction pattern can be identified using databases to find the reference pattern that matches the crystalline phase(s) of the sample. Measuring the positions of these peaks helps to identify the specific lattice plane distances or peak shifts. Peak fit analysis employs mathematical functions, such as Pearson VII and pseudo-Voigt, to model the shape of diffraction peaks. These functions facilitate the accurate fitting and analysis of peaks, thereby enabling the extraction of detailed information about the crystalline material. The measurement of FWHM and peak asymmetry reveals details on crystallite size and residual stresses within the coating material. Smaller FWHM values indicate larger crystallite sizes and/or lower strain. Peak intensity analysis offers insights into the relative abundance of different phases and possible preferred orientation (texture) in the sample.

4.1.3 Synchrotron X-ray Diffraction

Using laboratory equipment, X-ray diffraction measurements are typically confined to the surface regions of samples because only reflection geometry is used and the penetration depth of laboratory X-ray tubes is limited to a few micrometers. The spatial resolution required for the study of nanostructured thin films is limited by 1. the beam size and 2. the challenge of deconvoluting information from different penetration when performing X-ray diffraction experiments in reflection geometry [63,66]. A main factor is the brilliance of the X-ray source, including the photon flux density and beam alignment (e.g., parallelity, and monochromaticity. Conventional laboratory X-ray sources are significantly limited by their brilliance, i.e., they can produce small beam diameters of a few micrometers, but this comes at the cost of beam intensity. For X-ray diffraction experiments requiring sub-micrometer or nanometer beam diameters while maintaining high intensity, a synchrotron light source is necessary. Synchrotrons offer a brilliance that is several orders of magnitude higher than laboratory sources. Additionally, synchrotron facilities allow the use of transmission geometry due to the availability of higher photon energies, enabling greater X-ray penetration depths [66–68]. Synchrotron facilities are indispensable for in-situ micromechanical testing due to their brilliant and highly focused X-ray beams. Only the use of synchrotron X-rays allows real-time monitoring of material behavior at the sub-micro- or nanoscale to investigate the internal strains and stresses of the sample [69–73], while the high spatial resolution guarantees precise recording of the material response under different loading conditions for different crystallographic lattice plane families.

In a synchrotron X-ray microdiffraction experiment performed in transmission geometry, the diffraction cones are collected by a 2D detector positioned perpendicular to the incident X-ray beam [74–77]. The resulting Debye-Scherrer rings in Fig.4.4 reflect the sequence of peaks observed in a conventional laboratory (θ-2θ) scan, where the sample is rotated with respect to the incident X-ray beam while the detector remains stationary. Azimuthal integration of these rings using the DPDAK software package [78] produces a data set similar to a 1D (θ-2θ) scan. This integration process is performed for all 2D diffraction patterns acquired during the experiment and requires further data processing depending on the type of experiment.

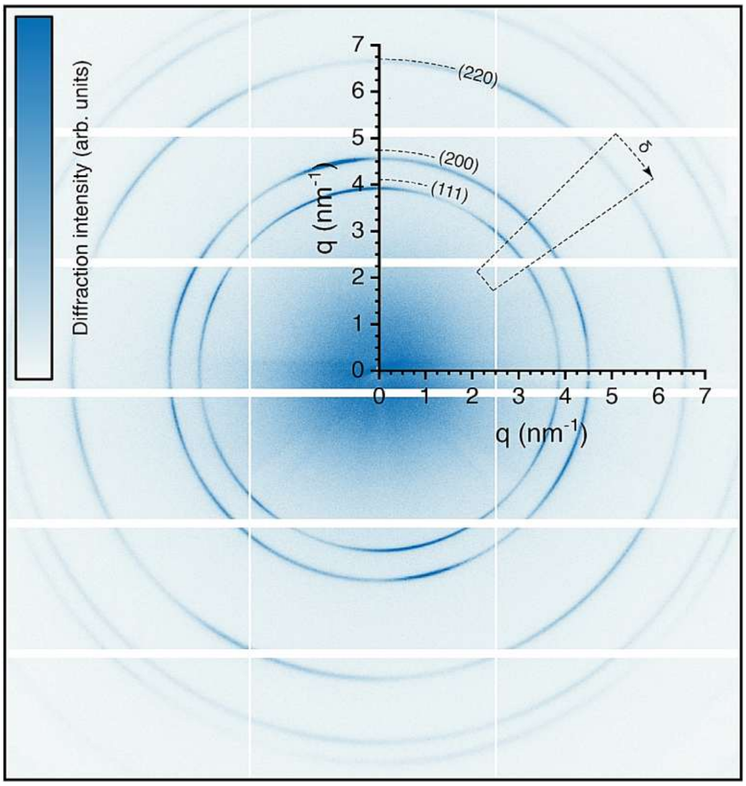

Figure 4.4. Debye-Scherrer Rings recorded for the {hkl}-plane families {111}, {200}, and {220] for a $TiN_{0.8}B_{0.2}$ cross-sectional thin film sample. The integration involves summing up the intensity values of diffraction spots at angle δ around the beam center.

4.1.4 X-ray Diffraction Stress Analysis

X-ray diffraction can further be used to probe the first-order strains (macrostrains), considering the elastic expansion and contraction of the crystal lattice and the resulting changes in lattice plane spacing [56,57,63,79]. X-ray diffraction measures only elastic strains, allowing direct conversion to corresponding stresses if the elastic properties of the material are known. This method measures only elastic strains, allowing direct conversion to corresponding deviatoric stresses if the elastic properties of the material are known. When testing ceramic thin films, which are characterized by predominantly elastic failure, it is reasonable to assume elastic material behavior during testing. Accurate determination of the unstrained lattice parameter, d_0^{hkl}, is crucial when calculating the X-ray elastic strain, $\varepsilon_{\theta\delta}^{hkl}(y,z)$ from

$$\varepsilon_{\theta\delta}^{hkl}(y,z) = \frac{d_{\theta\delta}^{hkl}(y,z) - d_0^{hkl}}{d_0^{hkl}} \tag{4.2}$$

where $d_{\theta\delta}^{hkl}(y,z)$ is the measured lattice spacing for a specific $\{hkl\}$ plane family in the direction of y and z. In a synchrotron X-ray diffraction experiment using transmission geometry, it is practical to use coordinates corresponding to the detector system, such as the diffraction angle, θ, and the azimuthal angle, δ, of the Debye-Scherrer ring. The fundamental equations for X-ray strain determination [79–81] to relate the X-ray elastic strain measurements, $\varepsilon_{\theta\delta}^{hkl}(y,z)$, to the total triaxial strain can be expressed as

$$\begin{aligned}\varepsilon_{\theta\delta}^{hkl}(y,z) &= \sin^2\theta\,\varepsilon_{xx}^{hkl}(y,z) + \cos^2\theta\,\sin^2\delta\,\varepsilon_{yy}^{hkl}(y,z) + \cos^2\theta\,\cos^2\delta\,\varepsilon_{zz}^{hkl}(y,z) \\ &\quad - \sin 2\theta\,\cos\delta\,\varepsilon_{zx}^{hkl}(y,z) + \cos^2\theta\,\sin 2\delta\,\varepsilon_{zy}^{hkl}(y,z) - \sin 2\theta\,\sin\delta\,\varepsilon_{xy}^{hkl}(y,z)\end{aligned} \tag{4.3}$$

Here, $\varepsilon_{xx}^{hkl}(y,z)$ and $\varepsilon_{yy}^{hkl}(y,z)$ denote the unknown in-plane strain components with respect to the measures specimen and $\varepsilon_{zz}^{hkl}(y,z)$ is the third unknown normal strain component in the out-of-plane (axial) direction. In the synchrotron experimental geometry, $\varepsilon_{xx}^{hkl}(y,z)$ is the normal strain component parallel to the incident X-ray beam. $\varepsilon_{zx}^{hkl}(y,z)$, $\varepsilon_{zy}^{hkl}(y,z)$, and $\varepsilon_{xy}^{hkl}(y,z)$ are the unknown shear strain components. If the material under investigation exhibits elastic isotropy on a macroscopic scale, the strain state can be related to the corresponding stress state using Hooke's law:

$$\begin{aligned}\varepsilon_{\theta\delta}^{hkl}(y,z) &= s_1^{hkl}\left[\sigma_{xx}(y,z) + \sigma_{yy}(y,z) + \sigma_{zz}(y,z)\right] \\ &\quad + \frac{1}{2}s_2^{hkl}\begin{bmatrix}\sin^2\theta\,\sigma_{xx}(y,z) + \ \cos^2\theta\,\sin^2\!\delta\,\sigma_{yy}(y,z) \\ + \cos^2\theta\,\cos^2\!\delta\,\sigma_{zz}(y,z)\end{bmatrix} \\ &\quad + \frac{1}{2}s_2^{hkl}\begin{bmatrix}-\sin 2\theta\,\cos\delta\,x(y,z) + \cos^2\theta\,\sin 2\delta\ \ \sigma_{zy}(y,z) \\ - \sin 2\theta\,\sin\delta\,\sigma_{xy}(y,z)\end{bmatrix}\end{aligned} \tag{4.4}$$

were $\sigma_{ij}(y,z)$ are the unknown stress components and s_1^{hkl} and $\frac{1}{2}s_2^{hkl}$ are the $\{hkl\}$-dependent diffraction (X-ray) elastic constants (DECs) of the material [63,79]. If the material also exhibits crystallographic elastic isotropy, the DECs are related to the overall elastic properties of the material, expressed in terms of Young's modulus, E^{hkl}, and Poisson's ratio, ν^{hkl}, as follows:

$$s_1^{hkl} = -\frac{\nu^{hkl}}{E^{hkl}} \tag{4.5}$$

and

$$\frac{1}{2}s_2^{hkl} = \frac{1+\nu^{hkl}}{E^{hkl}} \tag{4.6}$$

For most materials, the strain evaluated depends on the specific lattice plane family $\{hkl\}$, even for a polycrystalline material with a randomly oriented crystallographic texture. To address this, model that consider grain interaction [82–87] provide DECs with different values for different lattice plane families $\{hkl\}$, especially when calculated for materials that exhibit crystallographic elastic anisotropy.

In practice, Eq. (4.4) can be significantly simplified by assuming certain stress components are zero or equal. For instance, if we assume an uniaxial stress state with only stresses in the axial, z-direction, Eq. (4.4) reads

$$\varepsilon_{\theta\delta}^{hkl}(y,z) = \frac{1}{2}s_2^{hkl}\sigma_{zz}(y,z)\sin^2\delta + 2s_1^{hkl}\sigma_{zz}(y,z)$$

(4.7)
(4.7)

The stress state in the in-situ micropillar compression testing experiment performed in this thesis is assumed to uniaxial, where the pillar is compressed along a single axis, allowing for detailed investigation of material behavior under specific loading conditions. The evaluation procedure for this experiment is provided in greater detail in Chapter X.

4.2 Imaging Techniques

In materials science, our understanding of materials is built on the ability to visualize and image samples. From the macroscopic level down to the atomic scale, imaging techniques allow researchers to peer into the structure of materials, providing insight into how atoms are arranged and how these arrangements affect the material's properties. Researchers can obtain information about grain boundaries, defects, cracks, and morphology by taking high-resolution images of material surfaces and interfaces to characterize materials in unprecedented detail. Such insight is essential to characterize and locate these flaws, which can profoundly affect material performance in real-world applications. The revolutionary invention of the scanning tunneling microscope (STM) by Gerd Binnig and Heinrich Rohrer [88] (who shared the 1986 Nobel Prize in Physics with Ernst Ruska) is one of the most notable advances. This groundbreaking instrument revealed the intricate atomic-scale behavior and crystal growth mechanisms that had previously been hidden from sight. Similarly, the transmission electron microscope (TEM) pioneered by Ernst Ruska [89], which first surpassed optical resolution in the 1930s, has evolved over the years as manufacturers race to achieve the highest resolution possible. Other imaging technologies, such as the more accessible scanning electron microscope (SEM), have further expanded our imaging capabilities to guide material design and development. The prominent role of electrons in these techniques, due to their ease of focusing and scanning, has advanced the field of materials characterization and opened new avenues of exploration.

In the quest to study the intricate details of micro-structured coatings at the nanoscale, conventional optical microscopy faces a resolution limit imposed by the wavelength of visible light. The Abbe diffraction limit, expressed as

$$d = \frac{\lambda}{2n\ sin\theta} = \frac{\lambda}{2NA} \tag{4.8}$$

dictates that the resolving power of optical systems is limited by approximately half the wavelength of the illuminating light, restricting observations to features no smaller than a few hundred nanometers. The resolution limit, d, represents the minimum distance between two distinguishable points or features in an optical image. It is depends on the wavelength, λ, of the light used for imaging and the numerical aperture, NA, of the optical system, defined by n, the refractive index of the medium between the specimen to be observed and the objective lens, and θ, which is the half-angle of the maximum cone of light entering the lens.

Central to the principles of electron microscopy to overcome this criterion is the fundamental concept of wave-particle duality introduced by Louis de Broglie in 1924 [90]. According to de Broglie's hypothesis, which he formulated in his doctoral thesis (!) and for which he was honored with the Nobel Prize for Physics in 1929, every electron (or particle in general) exhibits wave-like properties. Given by the equation

$$\lambda_{DB} = \frac{h}{p_e} \tag{4.9}$$

an electron's momentum, p_e, is related to its De Borglie wavelength λ_{DB} by Planck's constant $h \approx$

$6.626 \cdot 10^{-34}$ Js. Electrons, as charged particles, can be accelerated by the use of electric fields within a vacuum chamber. When subjected to a high voltage, V, electrons are propelled toward the positively charged electrode and gain kinetic energy, $E_{kin} = eV$, in the process, where e denotes the elemental charge ($e \approx 1.602 \cdot 10^{-19}$ C). Consequently, p_e, can be derived from the mass of the electron, m_e, and its velocity, v:

$$p_e = m_e v = \sqrt{2 m_e e V} \tag{4.10}$$

Combining these relations, λ of an accelerated electron can be expressed as:

$$\lambda = \frac{h}{\sqrt{2 m_e e V}} \tag{4.11}$$

(4.11)

In practice, electron microscopes exploit this fundamental principle by accelerating electrons to high energies, resulting in wavelengths that are orders of magnitude smaller than those of visible light. For example, the voltage applied for TEM can reach hundreds of kV, while SEM analysis typically uses voltages in the 1-30 kV range. This level of resolution is essential for the study of the microstructure and texture of hard coatings, which are often characterized by complex defect structures on the nanometer scale.

4.2.1 Scanning Electron Microscopy

A scanning electron microscope (SEM) cross-section image provides unique insight into the microstructure of (hard) coating materials, revealing characteristic aspects of film growth to optimize deposition processes and ensure reliable performance in various applications. In addition, the SEM allows for quantitative analysis using EDS to identify the elemental composition and map the distribution of (metallic) elements across the coating surface. SEM coupled with Electron Backscatter Diffraction (EBSD) allows characterization of grain size (>50 nm and therefore not suitable for nanostructured hard coatings), crystallographic orientation and distribution, providing information on grain growth mechanisms and microstructural evolution

Thin film characterization on the SEM typically observes the coating cross section to reveal its morphology and characteristic columnar growth. Uniform deposition conditions are essential to achieve consistent coating properties. SEM analysis reveals variations in coating thickness, density, surface roughness, and morphology, highlighting regions of non-uniform growth to facilitate optimization of deposition parameters. SEM imaging further exposes the quality of the coating-substrate adhesion, as delamination compromises coating integrity and performance.

In SEM, an electron beam is generated in a controlled vacuum environment, typically at energies ≤30 keV. This beam, emitted from either thermionic or field emission sources, is precisely focused by electromagnetic lenses and subsequently scanned across the sample surface. Thermionic emission relies on the high-temperature excitation of a tungsten filament or an LaB_6 crystal, which facilitates the emission of electrons when the work function of the material is exceeded. Conversely, the use of a field emission gun (FEG) surpasses thermionic emission sources for applications requiring high resolution microscopy due to its ability to generate a highly coherent and intense electron beam. The fundamental principle behind the operation of an FEG is the phenomenon of field emission, a quantum mechanical process whereby electrons are emitted from a material surface when subjected to a strong electric field. Mathematically, the emission (or tunneling) of electrons from a solid surface can be described by the Fowler-Nordheim equation [91],

$$j(E) = \frac{A}{\Phi^2} \cdot |E|^2 \cdot e^{-\frac{B\Phi^{\frac{3}{2}}}{|E|}} \tag{4.12}$$

which relates the emitted current density, j, to the applied electric field, E, and material properties such as work function, Φ, where A and $B$are material constants. In FEG, a high voltage is applied to an extremely sharp metal tip (often made of single crystal tungsten or a similar high melting point material) with a radius of curvature r (where r is in the few nm or even sub-nm range). According to the expression $F = V/r$, the electric field strength, F, becomes exceptionally high at the tip, far exceeding the threshold required for electron emission.

Once emitted, the electrons form a divergent beam that spreads out from the emitter source and needs to be shaped and focused for imaging using a combination of electromagnetic lenses. Aperture systems are used to further control the size and shape of the beam. A prominent feature used to control the emitted electrons is the Wehnelt cylinder [92], which is positioned near the electron source. It is biased to a negative potential relative to the emitter. By adjusting the voltage applied to the Wehnelt cylinder, the focus of the electron beam can be fine-tuned to ensure optimal resolution and imaging performance. The focused electron beam is scanned across the surface of the sample using electromagnetic coils or electrostatic deflectors. These components precisely control the direction and amplitude of the beam's movement, allowing it to systematically scan the entire surface of the sample. As the electron beam traverses the material (up to a penetration depth of approximately 5 μm), it interacts with the sample atoms, which broadens its trajectory, resulting in an excitation volume with a plume-shaped profile. During this process, the electron beam exchanges energy with the atoms in the sample. If a sufficient amount of energy is transferred, secondary electrons (SE) are generated from the outer electron shells of the atoms. These low-energy SE undergo inelastic scattering, rapidly losing their energy and becoming reabsorbed by the sample. However, if they are located in close proximity to the surface (where the excitation volume is still narrow), some SE escape from the sample surface. SE are attracted to the detector by an electric field. The detector is positioned at an specific angle relative to the sample surface, which allows electrons emitted from edges facing the detector to be captured more efficiently. Conversely, electrons emitted from edges facing away from the detector may be reabsorbed to some extent. This setup creates the characteristic shadowing effect in SEM images, facilitating the interpretation of topographical features.

4.3 Chemical Analysis

Quantifying the elemental composition of thin films is both critical and challenging. The chemical composition (i.e., the number and types of atoms present during film nucleation) directly affects the structure-property relationship of the film and should be accurately determined. Only accurate compositional analysis will ensure that the desired stoichiometry is achieved, leading to reproducible synthesis of thin films with consistent properties.

However, most coating systems within the material class of ceramics belong to the borides, carbides, and nitrides and consist—in addition to their metallic counterpart(s)—of non-metal elements such as B, C, and/or N. These so-called light elements (due to their low atomic mass number, A) present significant challenges to commonly used quantification methods such as energy dispersive X-ray spectroscopy (EDS), which may overestimate the non-metal composition of the ceramic thin film. In addition, the inherently low sample thickness and the presence of impurities (mainly C and O) make accurate and reliable quantitative analysis difficult compared to bulk materials. Although EDS is a widely used and accessible non-destructive analytical technique for determining the relative elemental composition of metallic thin films and alloys, it is very limited for quantifying Ti–B–N thin films. It works by bombarding the sample under investigation with high energy electrons (~10-15 keV), causing the emission of characteristic X-rays from the atoms of the sample. The energy and intensity of these X-rays correspond to specific elements present in the sample. For quantitative EDS measurements, calibration with certified reference materials of known elemental composition is essential to establish a correlation between X-ray intensities and elemental concentrations. However, measuring light elements such as B (K_α=0.183 keV [93]) and N (K_α=0.392 keV [93]) by EDS results in weak X-ray signals that are masked by background noise (poor peak-to-background ratio). In addition, Ti (K_α=4.508 keV, L_α=0.452 keV [93,94]) and N have overlapping characteristic X-ray emission peaks (Ti L_α and N K_α) and it is not easy to distinguish them accurately.

4.3.1 Time-of-Flight Elastic Recoil Detection Analysis with Heavy Ions

To meet these challenges, Time-of-Flight Elastic Recoil Detection Analysis (ToF-ERDA) [95] with heavy ions (HI) proved to be the method of choice for quantifying the elemental composition of Ti–B–N thin films [96,97]. ToF-HI-ERDA operates on the classical Rutherford scattering principle of elastic collisions between incident ions and targeted atoms within the sample. By measuring the kinetic energy, E_{kin}, of recoiled atoms, a precise depth profiling of the material's elemental composition can be obtained without the need for specific calibration standards [98]. The sensitivity of ToF-ERDA to light elements is a consequence of their low atomic mass, resulting in a significant energy transfer during elastic collisions with incident heavier projectiles.

In ToF-HI-ERDA, a beam of heavy, high-energy ions (with a projectile energy in the MeV range) is accelerated toward the surface of the sample and impinges on the target with grazing incidence. The majority of these heavy ions undergo elastic scattering, exchanging energy and momentum with the nuclei of the target material without significant loss of kinetic energy. However, a fraction of these incoming projectiles undergo nuclear collisions, resulting in the recoil ejection of target atoms in the forward direction (as opposed to Rutherford Backscatter Spectrometry (RBS) analyses). The recoiled atoms carry some of the energy and momentum of the incoming ions. When a recoiled atom is created (ejected), it moves with a certain velocity, v, and kinetic energy, E_{kin}, where v and E_{kin} can be derived by using time-of-flight (ToF) spectrometers. By detecting the time-of-flight of recoiled atoms at different depths within the sample, ToF-HI-ERDA effectively obtains depth profiling information of all detected elements with a depth resolution of a few nm [99].

4.4 Mechanical Properties

Thin films, characterized by their nano-to-micron-scale thickness and high surface-to-volume ratio, exhibit unique and often enhanced properties compared to bulk materials. In order to assess the mechanical properties of a protective hard material coating, its ability to withstand load is of utmost importance. Thin films are usually not suitable for traditional mechanical testing methods due to their small dimensions. Instead, techniques such as micro-pillar compression [100], micro-cantilever bending [101–103], and nanoindentation [69] are used. However, the first two methods require extensive sample preparation and experience, often involving focused ion beam (FIB) milling [104]. Nanoindentation requires less sample preparation and is more accessible. Its advantage lies in its applicability to coated devices with varying mechanical properties.

4.4.1 Nanoindentation

Nanoindentation represents a significant advancement in hardness testing, offering automated measurement of both hardness, H, and Young's modulus, E. Using a sharp conical diamond indenter (e.g. Berkovich geometry [105]) with a tip radius in the nanometer range a controlled load, P, is applied to the coating's surface, inducing both elastic and plastic deformation within the material. Upon unloading, the temporary elastic deformation is reversed as the material reverts to its original shape. However, any plastic deformation remains in the form of indents (see Fig. 4.5a). The pioneering approach of Oliver and Pharr [106] eliminated the requirement for manually measuring the residual indentation size by leveraging contact mechanics to derive indentation dimensions from force-displacement curves recorded during testing (see Fig. 4.5b).

The depth of penetration into the material, h, and P are precisely monitored throughout the indentation process. This load-displacement relationship can be expressed using a power law

$$P = \alpha h^{m} \tag{4.13}$$

where α and m are constants of the indentation system.

Analysis of the non-linear force-displacement curve generated during unloading allows for the accurate determination of essential mechanical properties such as H and the indentation (or reduced) modulus, E_r, defined by the equation

$$\frac{1}{E_r} = \frac{(1-\nu^2)}{E} + \frac{(1-{\nu_i}^2)}{E_i} \tag{4.14}$$

where ν is the Poisson's ratio and the index i denotes the same parameters for the indenter.

According to Oliver and Pharr [106], E_r can be calculated as follows

$$E_r = \frac{dP}{dh}\frac{1}{2}\frac{\sqrt{\pi}}{\sqrt{A_c}} \tag{4.15}$$

This analysis relates the slope of the unloading force-displacement curve to the projected indentation contact area, A_c, to quantify the reduced material's stiffness and its ability to recover from deformation after loading. When the Poisson's ratio, ν, of the material is known, this approach allows the calculation of the polycrystalline Young's modulus E.

At peak load, P_{max}, the hardness of the coating material is defined as

$$H = \frac{P_{max}}{A_c} \tag{4.16}$$

assuming that the contact between the indenter and the material surface is well-defined. To isolate the ceramic film-only mechanical properties, it is crucial to limit the penetration depth of the indenter to less than 10% of the film thickness. Nanoindentation, as described in detail by T. Fisher-Cripps [107], provides a different approach to determining the reduced modulus of polycrystalline ceramic hard coatings. This method involves fitting a power-law function to load-displacement data obtained from indentations at various depths, allowing extrapolation of the film-only reduced modulus at zero indentation depth. providing a comprehensive understanding of the mechanical properties of the ceramic coatings.

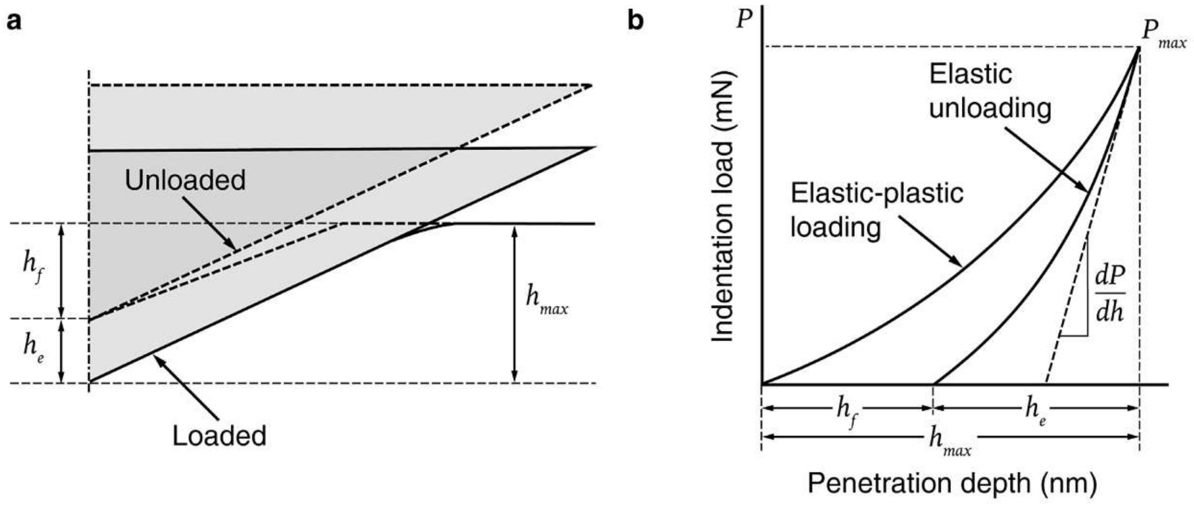

Figure 4.5 (a) Schematic representation of the indenter and specimen surface geometry at maximum load and complete unloading for a conical indenter. Adapted from [108]. (b) Exemplary illustration of a compliance curve from a nanoindentation experiment for elastic-plastic loading followed by elastic unloading with maximum load, P_{max}, and maximum depth, h_{max}, beneath the material's free surface. h_f denotes the depth of the residual impression, and h_e indicates the displacement associated with elastic recovery during unloading. The area, A, of the indentation contact and the slope of the elastic unloading, $\frac{dP}{dh}$, are used to calculate the reduced modulus, E_r, and hardness, H. Adapted from [107].

List of References

[1] P. H. Mayrhofer*, in Surface Technology* (Wien, 2024).

[2] D.L. Smith, *Thin-Film Deposition: Principles and Practice, first ed.*, McGraw-Hill, New York, 1995.

[3] L.B. Freund, S. Suresh, *Thin Film Materials Stress, Defect Formation and Surface Evolution*, Cambridge University Press, Cambridge, 2003.

[4] G.W. Grove, *On the electro-chemical polarity of gases*, Phil Trans R Soc. **142** (1852) 87–101.

[5] J.S. Chapin. U.S. Patent No. 4,166,018. Washington, DC: U.S. Patent and Trademark Office, 1979.

[6] B. Window, N. Savvides, *Charged particle fluxes from planar magnetron sputtering sources*, Journal of Vacuum Science & Technology A: Vacuum, Surfaces, and Films. **4** (1986) 196–202.

[7] J.A. Thornton, *High rate thick film growth*, Annual review of materials science. 7 (1977) 239–260.

[8] J.A. Thornton, *The microstructure of sputter-deposited coatings*, Journal of Vacuum Science & Technology A: Vacuum, Surfaces, and Films. **4** (1986) 3059–3065.

[9] R.F. Bunshah, C. Weissmantel, *Handbook of hard coatings*, *Vol. 3*, Noyes Publications, Park Ridge, New Jersey, 2001.

[10] W.D. Sproul, *High rate reactive sputtering process control*, Surf Coat Technol. 33 (1987) 73–81.

[11] W.D. Sproul, D.J. Christie, D.C. Carter, *Control of reactive sputtering processes*, Thin Solid Films. **491** (2005) 1–17.

[12] J. Musil, S. Kadlec, W.-D. Münz, *Unbalanced magnetrons and new sputtering systems with enhanced plasma ionization*, Journal of Vacuum Science & Technology A: Vacuum, Surfaces, and Films. **9** (1991) 1171–1177.

[13] J. Paulitsch, M. Schenkel, T. Zufraß, P.H. Mayrhofer, W.D. Münz, *Structure and properties of high power impulse magnetron sputtering and DC magnetron sputtering CrN and TiN films deposited in an industrial scale unit*, Thin Solid Films. **518** (2010) 5558–5564.

[14] W. Münz, *Titanium aluminum nitride films: A new alternative to TiN coatings*, Journal of Vacuum Science & Technology A: Vacuum, Surfaces, and Films. **4** (1986) 2717–2725.

[15] H. Willmann, P.H. Mayrhofer, P.O.Å. Persson, A.E. Reiter, L. Hultman, C. Mitterer, *Thermal stability of Al-Cr-N hard coatings*, Scr Mater. **54** (2006) 1847–1851.

[16] J.R. Banavar, A. Maritan, A. Rinaldo, *Size and form in efficient transportation networks*, Nature, **399** (1999) 130–132.

[17] P.H. Mayrhofer, C. Mitterer, L. Hultman, H. Clemens, *Microstructural design of hard coatings*, Prog Mater Sci. **51** (2006) 1032–1114.

[18] L. Hultman, *Thermal stability of nitride thin films*, Vacuum. **57** (2000) 1–30.

[19] I. Petrov, L. Hultman, M. Stueber, L.C. Chen, P. Desjardins, *Preface of the special issue "Thin Films Advances" dedicated to the 75th birthday of Professor Joe Greene*, Thin Solid Films. **688** (2019) 137494.

[20] W. Gissler, *Structure and properties of Ti-B-N coatings*, Surf Coat Technol. **68** (1994) 556–563.

[21] P.H. Mayrhofer, M. Stoiber, C. Mitterer, *Age hardening of PACVD TiBN thin films*, Scr Mater. **53** (2005) 241–245.

[22] P.H. Mayrhofer, M. Stoiber, *Thermal stability of superhard Ti-B-N coatings*, Surf Coat Technol. **201** (2007) 6148–6153.

[23] C. Mitterer, P.H. Mayrhofer, M. Beschliesser, P. Losbichler, P. Warbichler, F. Hofer, P.N. Gibson, W. Gissler, H. Hruby, J. Musil, J. Vlček, *Microstructure and properties of nanocomposite Ti-B-N and Ti-B-C coatings*, Surf Coat Technol. **120** (1999) 405–411.

[24] G. Hägg, *Eigenschaften der Phasen von Übergangselementen in binären Systemen mit Bor, Kohlenstoff und Stickstoff*, Z Phys Chem B, **6** (1929) 221–232.

[25] G. Hägg, *Gesetzmässigkeiten im kristallbau bei hydriden, boriden, carbiden und nitriden der übergangselemente*, Z Phys Chem B. **12** (1931) 33–56.

[26] H. Holleck, *Material selection for hard coatings*, Journal of Vacuum Science & Technology A: Vacuum, Surfaces, and Films. **4** (1986) 2661–2669.

[27] S.P.K. Yalaman Chilli, D. Kurapov, T. Sasaki, K. Kubota, Oerlikon Surface Solutions AG, Pfäffikon, Mitsubishi Hitachi Tool Engineering, LTD. *Cubic Al-rich AlTiN Coatings Deposited from Ceramic Targets*. WO 2020/094882 A1, 2019.

[28] P.H. Mayrhofer, D. Music, J.M. Schneider, *Influence of the Al distribution on the structure, elastic properties, and phase stability of supersaturated* $Ti_{1-x}Al_xN$, J Appl Phys. **100** (2006) 094906.

[29] H. Holleck, *Metastable coatings—Prediction of composition and structure*, Surface and Coatings Technology. **36** (1988) 151–159.

[30] P.H. Mayrhofer, A. Hörling, L. Karlsson, J. Sjölén, T. Larsson, C. Mitterer, L. Hultman, *Self-organized nanostructures in the Ti-Al-N system*, Appl Phys Lett. **83** (2003) 2049–2051.

[31] A. Jain, S.P. Ong, G. Hautier, W. Chen, W.D. Richards, S. Dacek, S. Cholia, D. Gunter, D. Skinner, G. Ceder, K.A. Persson, *Commentary: The materials project: A materials genome approach to accelerating materials innovation*, APL Mater. **1** (2013) 011002.

[32] C. Kainz, N. Schalk, M. Tkadletz, C. Mitterer, C. Czettl, *The effect of B and C addition on microstructure and mechanical properties of TiN hard coatings grown by chemical vapor deposition*, Thin Solid Films. **688** (2019) 137283.

[33] K.-T. Rie, A. Gebauer, J. Wiihle, *Plasma assisted CVD for low temperature coatings and corrosion resistance to improve the wear*, Surf Coat Technol. **86** (1996) 498–506.

[34] J. Neidhardt, Z. Czigány, B. Sartory, R. Tessadri, M. O'Sullivan, C. Mitterer, *Nanocomposite Ti-B-N coatings synthesized by reactive arc evaporation*, Acta Mater. **54** (2006) 4193–4200.

[35] R. Hahn, A. Tymoszuk, T. Wojcik, A. Kirnbauer, T. Kozák, J. Čapek, M. Sauer, A. Foelske, O. Hunold, P. Polcik, P.H. Mayrhofer, H. Riedl, *Phase formation and mechanical properties of reactively and non-reactively sputtered Ti-B-N hard coatings*, Surf Coat Technol. **420** (2021) 127327.

[36] W. Gissler, P.N. Gibson, *Titanium Implantation into Boron Nitride Films and Ion-Beam Mixing of Titanium-Boron Nitride Multilayers*, Ceramics international. **22** (1996) 335–340.

[37] T. Friesen, J. Haupt, W. Gissler, A. Barna, P.B. Barna, *Ultrahard coatings from Ti-BN multilayers and by co-sputtering*, Surface and Coatings Technology. **48** (1991) 169–174 .

[38] H. Nowotny, F. Benesovsky, C. Brukl, *Die Dreistoffe: Titan—Bor—Kohlenstoff und Titan—Bor—Stickstoff*, Monatshefte für Chemie und verwandte Teile anderer Wissenschaften. **92** (1961) 403–414.

[39] P.H. Mayrhofer, C. Mitterer, J.G. Wen, I. Petrov, J.E. Greene, *Thermally induced self-hardening of nanocrystalline Ti-B-N thin films*, J Appl Phys. **100** (2006) 044301.

[40] B. Cordero, V. Gómez, A.E. Platero-Prats, M. Revés, J. Echeverría, E. Cremades, F. Barragán, S. Alvarez, *Covalent radii revisited*, Journal of the Chemical Society. Dalton Transactions. **21** (2008) 2832–2838.

[41] E.O. Hall, *The Deformation and Ageing of Mild Steel: III Discussion of Results*, Proceedings of the Physical Society. Section B. **64** (1951) 747–747.

[42] N.J. Petch, *The influence of grain boundary carbide and grain size on the cleavage strength and impact transition temperature of stee*l, Acta Metallurgica. **34** (1986) 1387–1393.

[43] G. Gottstein Physikalische *Grundlagen, Materialwissenschaft und Werkstofftechnik*, Springer-Verlag, Berlin Heidelberg, 2014.

[44] J.W. Gibbs, *On the equilibrium of heterogeneous substances, vol 1. Collected works*, Longmans, Green, and Co., New York, 1876.

[45] W. Sun, S.T. Dacek, S.P. Ong, G. Hautier, A. Jain, W.D. Richards, A.C. Gamst, K.A. Persson, G. Ceder, *The thermodynamic scale of inorganic crystalline metastability*, Science advances. **2** (2016) e1600225.

[46] W. Sun, A. Holder, B. Orvañanos, E. Arca, A. Zakutayev, S. Lany, G. Ceder, *Thermodynamic Routes to Novel Metastable Nitrogen-Rich Nitrides*, Chemistry of Materials. **29** (2017) 6936–6946.

[47] W. Sun, C.J. Bartel, E. Arca, S.R. Bauers, B. Matthews, B. Orvañanos, B.R. Chen, M.F. Toney, L.T. Schelhas, W. Tumas, J. Tate, A. Zakutayev, S. Lany, A.M. Holder, G. Ceder, *A map of the inorganic ternary metal nitrides*, Nat Mater. **18** (2019) 732–739.

[48] W. Hume-Rothery, J Inst Metals, 1926, 35, 319–335.

[49] A. Martin and M. Thuo, *Beyond Hume-Rothery Rules*, Acc Mater Res. **4** (2023) 809–813.

[50] H. Frey, H.R. Khan, Handbook of Thin-Film Technology, Springer-Verlag, Berlin Heidelberg, 2015.

[51] F.-W. Bach, K. Möhwald, A. Laarmann, T. Wemz, *Moderne Beschichtungsverfahren*, WILEY-CH Verlag GmbH & Co. KGaA, Weinheim, 2005.

[52] M. Ohring, *Material Science of Thin Films - Science, Applications and Technology, 3rd ed.*, Academic Press Inc., 2002.

[53] P. M. Martin, *Handbook of Deposition Technologies for Films and Coatings - Science, Application and Technology*, *3rd ed.*, Elsevier Inc., Oxford, 2010.

[54] U. Behringer, H. Gärtner, R. Grün, G. Kienel, M. Knepper, E. Lugscheider, H. Oechsner, G. Wahl, J. Waldorf, G.K. Wolf, *Vakuumbeschichtung 2*, Springer-Verlag, Berlin Heidelberg, 1994.

[55] M. De Graef, and M. E. Henry, *Structure of Materials*, Cambridge University Press, Cambridge, 2007.

[56] L.H. Schwartz, J.B. Cohen, *Diffraction from Materials*, Springer-Verlag, Berlin Heidelberg, 1987.

[57] V. Hauk, *Structural and Residual Stress Analysis by Nondestructive Methods, second ed.*, Elsevier Science B.V., Amsterdam, 1997.

[58] J. Todt, PhD thesis, Montanuniversität Leoben, 2016.

[59] W.C. Röntgen, *On a new kind of rays*, Science. **3** (1896) 227-231.

[60] J.E. Lilienfeld, *Über eine allgemeine und hervorragend empfindliche Methode zur spektralen qualitativen Elementaranalyse von Gasgemischen*, Annalen der Physik. **321** (1905) 931–942.

[61] L. Spieß, R. Schwarzer, H. Behnken, and G. Teichert, *Moderne Röntgenbeugung, first ed.*, Teubner Verlag, 2005.

[62] B.J. Brentano, *Focussing method of crystal powder analysis by X-rays*, Phys. Soc. London. **37** (1924) 184–942.

[63] M. Birkholz, *Thin Film Analysis by X-Ray Scattering*, WILEY-CH Verlag GmbH & Co. KGaA, Weinheim, 2006.

[64] M.M. Woolfson, *An Introduction to X-ray Crystallography, second ed.*, Cambridge University Press, Cambridge, 1970.

[65] W.H. Bragg, W.L. Bragg, *The Reflection of X-rays by Crystals*, Proceedings of the Royal Society of London. Series A, Containing Papers of a Mathematical and Physical Character, **88** (1913), 428–438.

[66] M. Stefenelli, J. Todt, A. Riedl, W. Ecker, T. Müller, R. Daniel, M. Burghammer, J. Keckes, *X-ray analysis of residual stress gradients in TiN coatings by a Laplace space approach and cross-sectional nanodiffraction: A critical comparison*, J Appl Crystallogr. **46** (2013) 1378–1385.

[67] J. Keckes, M. Bartosik, R. Daniel, C. Mitterer, G. Maier, W. Ecker, J. Vila-Comamala, C. David, S. Schoeder, M. Burghammer, *X-ray nanodiffraction reveals strain and microstructure evolution in nanocrystalline thin films*, Scr Mater. **67** (2012) 748–751.

[68] M. Bartosik, R. Daniel, C. Mitterer, I. Matko, M. Burghammer, P.H. Mayrhofer, J. Keckes, Cross-sectional X-ray nanobeam diffraction analysis of a compositionally graded CrNx thin film, Thin Solid Films. 542 (2013) 1–4.

[69] A. Zeilinger, J. Todt, C. Krywka, M. Müller, W. Ecker, B. Sartory, M. Meindlhumer, M. Stefenelli, R. Daniel, C. Mitterer, J. Keckes, *In-situ Observation of Cross-Sectional Microstructural*

Changes and Stress Distributions in Fracturing TiN Thin Film during Nanoindentation, Sci Rep. **6** (2016) 22670.

[70] J. Todt, C. Krywka, Z.L. Zhang, P.H. Mayrhofer, J. Keckes, M. Bartosik, *Indentation response of a superlattice thin film revealed by in-situ scanning X-ray nanodiffraction*, Acta Mater. **195** (2020) 425–432.

[71] W. Ecker, J. Keckes, M. Krobath, J. Zalesak, R. Daniel, M. Rosenthal, J. Todt, *Nanoscale evolution of stress concentrations and crack morphology in multilayered CrN coating during indentation: Experiment and simulation*, Mater Des. **188** (2020) 108478.

[72] L. Zauner, R. Hahn, E. Aschauer, T. Wojcik, A. Davydok, O. Hunold, P. Polcik, H. Riedl, *Assessing the fracture and fatigue resistance of nanostructured thin films*, Acta Mater. **239** (2022) 118260.

[73] M. Meindlhumer, L.R. Brandt, J. Zalesak, M. Rosenthal, H. Hruby, J. Kopecek, E. Salvati, C. Mitterer, R. Daniel, J. Todt, J. Keckes, A.M. Korsunsky, *Evolution of stress fields during crack growth and arrest in a brittle-ductile CrN-Cr clamped-cantilever analysed by X-ray nanodiffraction and modelling*, Mater Des. **198** (2021) 109365.

[74] A.P. Hammersley, S.O. Svensson, A. Thompson, *Calibration and correction of spatial distortions in 2D detector systems*, Nucl Instrum Methods Phys Res A. **346** (1994) 312–321.

[75] M. Stefenelli, PhD thesis, Montanuniversität Leoben, 2014.

[76] A.P. Hammersley, S.O. Svensson, A. Thompson, H. Graafsma, Å. Kvick, J.P. Moy, *Calibration and correction of distortions in two-dimensional detector systems*, Review of Scientific Instruments. **66** (1995) 2729–2733.

[77] B.B. He, *Introduction to two-dimensional X-ray diffraction*, Powder Diffr. **18** (2003) 71–85.

[78] G. Benecke, W. Wagermaier, C. Li, M. Schwartzkopf, G. Flucke, R. Hoerth, I. Zizak, M. Burghammer, E. Metwalli, P. Müller-Buschbaum, M. Trebbin, S. Förster, O. Paris, S. V. Roth, P. Fratzl, *A customizable software for fast reduction and analysis of large X-ray scattering data sets: Applications of the new DPDAK package to small-angle X-ray scattering and grazing-incidence small-angle X-ray scattering*, J Appl Crystallogr. **47** (2014) 1797–1803.

[79] I. Noyan, and J. Cohen, *Residual Stress: Measurement by Diffraction and Interpretation*, ed. B., Springer-Verlag, Berlin Heidelberg, 1987.

[80] M. Stefenelli, R. Daniel, W. Ecker, D. Kiener, J. Todt, A. Zeilinger, C. Mitterer, M. Burghammer, J. Keckes, *X-ray nanodiffraction reveals stress distribution across an indented multilayered CrN-Cr thin film*, Acta Mater. 85 (2015) 24–31.

[82] R.A. Winholtz, J.B. Cohen, *Generalised Least-squares Determination of Triaxial Stress States by X-ray Diffraction and the Associated Errors*, J Phys. **41** (1988) 189–199.

[83] R. Hill, The Elastic Behaviour of a Crystalline Aggregate, Proc Phys Soc A. **65** (1952) 349–354.

[84] A. Reuss, Berechnung der Fließgrenze von Mischkristallen auf Grund der Plastizitätsbedingung für Einkristalle, Z angew Math Mech. **9** (1929) 49–58.

[85] J.D. Eshelby, The Determination of the Elastic Field of an Ellipsoidal Inclusion, Proc R Soc Lond A. **1226** (1957) 376–396.

[86] W. Voigt, *Lehrbuch der Kristallphysik (mit Ausschluss der Kristalloptik)*, B.G. Teubner, 1910.

[87] T. Gnäupel-Herold, ISODEC: *Software for calculating diffraction elastic constants*, J Appl Crystallogr. **45** (2012) 573–574.

[88] E. Kröner, *Berechnung der elastischen Konstanten des Vielkristalls aus den Konstanten des Einkristalls*, Z Physik. **151** (1958) 504–518.

[89] G. Binnig, H. Rohrer, C. Gerber, E. Weibel, *Surface studies by scanning tunneling microscopy*, Physical review letters. **49** (1982) 57–61.

[90] V.M. Knoll, E. Ruska, *Das Elektronenmikroskop*, Zeitschrift für Physik. **78** (1932) 318–339.

[91] L. De Broglie, PhD thesis, Migration-université en cours d'affectation, 1924.

[92] R.H. Fowler, L. Nordheim, *Electron emission in intense electric fields*, Proceedings of the Royal Society of London. Series A, Containing Papers of a Mathematical and Physical Character. **781** (1928) 173–181.

[93] A. Wehnelt, *Über den Austritt negativer Ionen aus glühenden Metallverbindungen und damit zusammenhängende Erscheinungen*, Annalen der Physik. **8** (1904) 425–468.

[94] J.A. Bearden, *X-ray wavelengths*, Reviews of Modern Physics. **39** (1967) 78–124.

[95] R.D. Deslattes, E.G. Kessler Jr., P. Indelicato, L. de Billy, E. Lindroth, J. Anton, J.S. Coursey, D.J. Schwab, C. Chang, R. Sukumar, K. Olsen, and R.A. Dragoset (2005), *X-ray Transition Energies (version 1.2)*, http://physics.nist.gov/XrayTrans. Access : 22.05.2024, National Institute of Standards and Technology, Gaithersburg, MD.

[96] J. L'Ecuyer, C. Brassard, C. Cardinal, J. Chabbal, L. Deschênes, J.P. Labrie, B. Terreault, J.G. Martel, R. St.-Jacques, *An accurate and sensitive method for the determination of the depth distribution of light elements in heavy materials*, J Appl Phys. **47** (1976) 381–382.

[97] B. Bakhit, D. Primetzhofer, E. Pitthan, M.A. Sortica, E. Ntemou, J. Rosen, L. Hultman, I. Petrov, G. Greczynski, *Systematic compositional analysis of sputter-deposited boron-containing thin films*, Journal of Vacuum Science & Technology A: Vacuum, Surfaces, and Films. 39 (2021) 063408.

[98] J. Dobrovodský, D. Vana, M. BeÅo, F. Lofaj, R. Riedlmajer, *Ion Beam Analysis including ToF-ERDA of complex composition layers*, in: J Phys Conf Ser, Institute of Physics, 2024.

[99] P. Ström, D. Primetzhofer, *Ion beam tools for nondestructive in-situ and in-operando composition analysis and modification of materials at the Tandem Laboratory in Uppsala*, Journal of Instrumentation. 17 (2022) P04011.

[100] K. Yasuda, *Time-of-flight ERDA for depth profiling of light elements*, Quantum Beam Science. 4 (2020) 40.

[101] M.D. Uchic, D.M. Dimiduk, J.N. Florando, W.D. Nix, *Sample dimensions influence strength and crystal plasticity*, Science. **305** (2004) 986–989.

[102] K. Matoy, H. Schönherr, T. Detzel, T. Schöberl, R. Pippan, C. Motz, G. Dehm, *A comparative micro-cantilever study of the mechanical behavior of silicon based passivation films*, Thin Solid Films. **518** (2009) 247–256.

[103] W. Luo, C. Kirchlechner, X. Fang, S. Brinckmann, G. Dehm, F. Stein, *Influence of composition and crystal structure on the fracture toughness of NbCo2 Laves phase studied by micro-cantilever bending tests*, Mater Des. **145** (2018) 116–121.

[104] J. Ast, G. Mohanty, Y. Guo, J. Michler, X. Maeder, *In situ micromechanical testing of tungsten micro-cantilevers using HR-EBSD for the assessment of deformation evolution*, Mater Des. **117** (2017) 265–266.

[105] R.M. Langford, M. Rogers, *In situ lift-out: Steps to improve yield and a comparison with other FIB TEM sample preparation techniques*, Micron. **39** (2008) 1325–1330.

[106] E.S. Berkovich, *Three faceted diamond pyramid for micro-hardness testing*, Industrial Diamond Review. **111** (1951) 129.

[107] W.C. Oliver, G.M. Pharr, *An improved technique for determining hardness and elastic modulus using load and displacement sensing indentation experiments*, J Mater Res. **7** (1992) 1564–1583.

[108] A.C. Fischer-Cripps, *Critical review of analysis and interpretation of nanoindentation test data*, Surf Coat Technol. **200** (2006) 4153–4165.

5 A Strategy to Enhance the B-Solubility and Mechanical Properties of Ti–B–N Thin Films

The Ti–B–N system offers a wide range of possible meta(stable) phases, making it interesting for science and industry. However, the solubility for B within the face-centered cubic (fcc)-TiN lattice is rather limited and less studied, especially without forming B-rich phases. Therefore, we address how chemistries along the TiN–TiB_2 or TiN–TiB tie-line influence this B-solubility. The variation between these two tie-lines is realized through non-reactive co-sputtering of a TiN, TiB_2, and Ti target. We show that for variations along the TiN–TiB tie-line, even 8.9 at.% B (equivalent to 19.3 at.% non-metal fractions) can fully be incorporated into the fcc-TiN_y lattice without forming other B-containing phases. The combination of detailed microstructural characterization through X-ray diffraction and transmission electron microscopy with ab initio calculations of fcc $Ti_{1-x}NB_x$, $TiN_{1-x}B_x$, and $TiN_{1-2x}B_x$ solid solutions indicates that B essentially substitutes N. The single-phase fcc-$TiB_{0.17}N_{0.69}$ (the highest B-containing sample along the TiN–TiB tie-line studied) exhibits the highest hardness H of 37.1±1.9 GPa combined with the highest fracture toughness K_{IC} of 3.0±0.2 MPa·m$^{1/2}$ among the samples studied. These are markedly above those of B-free $TiN_{0.87}$ having H = 29.2±2.1 GPa and K_{IC} = 2.7±<0.1 MPa·m$^{1/2}$.

5.1 Introduction

Hard coatings have revolutionized materials science and engineering by enhancing the performance and durability of various materials. In particular, TiN thin films—offering an outstanding combination of mechanical properties—have found extensive usage as protective coatings for cutting tools exposed to severe mechanical and corrosive loads [1,2]. While boron (B) addition can significantly improve the hardness, wear resistance, and thermal stability of TiN-based coatings [3–7], achieving its full incorporation in the face-centered cubic (fcc) lattice is challenging [8–10]. To address this limitation, we investigate how variations either along the TiN–TiB_2 or TiN–TiB tie-line influence the solubility of B in TiN_y. We used non-reactive magnetron co-sputtering of a TiN, TiB_2, and Ti target for this task.

The larger covalent bonding radii of B (0.84 Å) compared to N (0.71 Å) cause lattice distortions in TiN when N atoms are substituted by B [11], bringing a dielastic contribution to the solid solution strengthening mechanisms (see Fleischer's formula [12]). However, the atomic size difference and altered bond characteristics limit the full incorporation of B in the TiN lattice [13]. Typically, excess B segregates at grain boundaries [14], hindering coalescence during nucleation and coarsening during film growth. The change to a smaller-grained microstructure increases hardness by grain refinement strengthening [15,16]. Nanocomposite Ti–B–N coatings exhibit a similar effect, where TiN and TiB_2 grow simultaneously in a sequence of segregation-driven renucleation processes [17,18]. However, in reactively deposited coatings, limited B solubility in TiN induces the formation of soft amorphous BN phases [19]. Generally, the chemistry of reactively deposited coatings follows the TiN–BN tie line more. In contrast, non-reactive approaches allow compositions along the TiN–TiB_2 and TiN–TiB tie lines, achieving hard and super hard (> 40 GPa) coatings [19].

Previous studies on Ti–B–N coatings developed a well-understood ternary phase system [3,4,17–20], providing a solid basis for understanding the impact of B on the microstructure and mechanical properties of TiN [20–23]. However, soluting higher amounts of B in the fcc lattice—without forming secondary phases—remains challenging. To overcome this challenge, we propose a non-reactive co-sputtering approach to achieve a single-phased Ti–B–N solid solution with a high amount of B incorporated in the TiN lattice.

Specifically, we aimed for Ti–B–N coatings with chemistry along two quasibinary tie lines: (i) TiN–TiB_2, via co-sputtering TiN and TiB_2 targets, and (ii) TiN–TiB, via co-sputtering TiN, TiB_2, and Ti. For easier reading, these coating systems are referred to as TiN–TiB_2 and Ti(N,B). Notably, TiN–TiB_2 refers to the analogous tie-line, not the coating composition. Varying the current applied to the TiB_2 and Ti targets—while keeping that at TiN constant—we show that additional co-sputtering of Ti increases the solubility of B in TiN up to 8.9 at.%. Ab initio density functional theory calculations underpin these observations. Furthermore, Ti over-stoichiometry (or more vacancies at the non-metal sublattice [24]) is required to maintain the high hardness of single-phased Ti–B–N and fracture toughness if the B-content exceeds ~3 at.%.

5.2 Materials and Methods

Six different Ti–B–N coatings, in addition to one TiN_y, were prepared with an AJA International Orion 5 PVD machine equipped with one 3” and two 2” unbalanced magnetron sputtering sources holding a TiN (99.5 % purity), TiB_2 (99.5 % purity), and Ti (grade 2) target (all from Plansee Composite Materials GmbH), respectively. Before loading and mounting the substrates Si (100) 7×20×0.38 mm^3, mirror polished austenitic steel 7×20×0.75 mm^3, and single crystalline sapphire $(1\bar{1}02)$ 10×10×0.53 mm^3 to the deposition chamber, they were ultrasonically cleaned in acetone and ethanol for 5 min each. Inside the chamber—after reaching the base pressure of below $1\cdot10^{-4}$ Pa ($1\cdot10^{-6}$ mbar)—the substrates were thermally cleaned at ~450 °C for 20 min, afterwards Ar-ion etched using an Ar pressure (20 sccm Ar-flow) of 6 Pa and applying a negative voltage of 750 V to the rotating (1 Hz) substrate-holder (keeping the ~450 °C). During depositions—using a current-controlled mode for sputtering the target—the substrates were negatively biased with -60 V DC. The Ar pressure was 0.4 Pa (10 sccm Ar-flow) while the temperature and the substrate-holder rotation was 1 Hz. The 4-inch substrate holder is ~10 cm above the confocal target arrangement. Different chemistries of the Ti–B–N coatings are obtained by adjusting solely the sputtering-currents applied to the 2-inch TiB_2 (I_{TiB2}) and Ti (I_{Ti}) targets between 0 and 0.6 A, while the TiN target was always operated with I_{TiN} = 0.75 A. The other deposition parameters were kept constant using a substrate bias of -60 V DC, substrate temperature of ~450 °C, substrate-holder rotation of 1 Hz, and an Ar pressure of 0.4 Pa (10 sccm Ar-flow). In addition to the TiN_y coating (i.e., I_{Ti} = I_{TiB2} = 0 A), three Ti–B–N coatings are prepared only with the TiN and TiB_2 target (i.e., I_{Ti} = 0 A, and I_{TiB2} = 0.2, 0.4, 0.6 A), and three are prepared by synchronizing the TiB_2 and Ti target (i.e., I_{Ti} = I_{TiB2} = 0.2, 0.4, 0.6 A). For easier distinction, the first three are referred to as TiN–TiB_2 and the last three as Ti(B,N) throughout the manuscript; overall, they will be named Ti–B–N. The deposition time was adjusted between 80 and 92 min (based on pre-studies) to prepare coatings with a thickness t of ~2 µm.

Their chemical composition was obtained from samples deposited on sapphire through Time-of-Flight Elastic Recoil Detection Analysis (ToF-ERDA) at the 5 MV Pelletron Tandem accelerator at Uppsala University [25] using $^{127}I^{8+}$ projectiles with a primary energy of 36 MeV. The beam incident angle was 67.5° to the surface normal, where recoils reached the detector at an angle of 45° with respect to the incident beam direction. The raw experimental data were analyzed using the CONTES software package [26]. Total systematic and statistical uncertainties were estimated to be below 5% of the deduced value for the major constituents. Additional chemical information was obtained from X-ray fluorescence (XRF) measurements using a PANalytical AxiosmAX-Advanced spectrometer with a rhodium (Rh) X-ray tube operating at 50 kV and 55 mA under vacuum conditions—calibrated with the three ERDA-analyzed $TiN_{0.87}$, TiN+TiB_2 (10.4 at.% B), and Ti(N,B) (8.9 at.% B) thin films.

Structural information of the coatings was derived from X-ray diffraction patterns collected with a PANalytical XPert Pro MPD (θ-θ diffractometer) in Bragg Brentano geometry, which was equipped with a CuKα radiation source operated with 45 kV and 40 mA. Fracture cross sections were investigated with an FEI Quanta 250 scanning electron microscopy (SEM) equipped with a field emission gun (operating at 10 kV) using fracture cross-sections of samples grown on Si (100) and with an FEI F20 transmission electron microscopy (TEM) equipped with a field emission gun (operating at 200 kV). The cross-section TEM samples were prepared by mechanical polishing down to 10 µm lamella thickness, following conventional preparation steps, and subsequent Ar ion milling (using a GATAN PIPS II). Top-view TEM lamella preparation was accomplished by focused ion beam (FIB) cutting on a Thermo Fischer Scios 2 DualBeam system, following a typical FIB TEM sample preparation recipe [27]. Initially, a 2 µm thick plane-view lamella was cut free, followed by ion milling steps to achieve a final thickness of about 75 nm. A final cleaning step at 2 kV and 27 pA and subsequent Ar ion milling at 0.5 kV using a Gatan PIPS II system resulted in <25 nm thickness in specific areas. A 200 kV field emission TEM (JEOL 2100F) equipped with an image-side CS-corrector and Gatan Tridiem system was used in the high-resolution TEM (HRTEM) study, which demonstrates a resolution of 1.2 Å at 200 kV. The aberration coefficient is set close to zero, under which the HRTEM images were taken under slightly over-focus conditions (close to the Scherzer defocus). The point spectra and electron energy-loss spectrum (EELS) mapping were recorded under scanning TEM (STEM) mode with a camera length of 2 cm and a dispersion of 0.2 eV per channel. The spectra were processed in a Digital Micrograph (DM version 3.42). The background was subtracted using the power-law model. The specimen thickness was estimated to be less than 0.5 (thickness (t)/mean free path(λ)) using zero-loss peak. All the spectra were calibrated using zero-loss spectra. EELS core-loss spectra were smoothed using low-pass filtering (per 2 channels) in DM.

Indentation modulus and hardness were obtained through computer-controlled nanoindentation using a UMIS II System equipped with a diamond Berkovich tip (calibrated using a fused silica standard sample). To minimize the substrate influence, we excluded data points with indentation depths larger than 10% of the coating thickness. To obtain the film-only Young's modulus, the raw modulus data were fitted and extended towards zero indentation depth, following the instructions given in [28,29]. Biaxial residual stresses of the coatings on sapphire substrates were obtained by measuring their curvature using a Nanovea PS50 profilometer and applying the Stoney equation [30].

(5.2)

The fracture toughness in terms of the critical intensity factor (K_{IC}) was derived from in-situ microcantilever bending tests with a Hysitron PI-85 SEM PicoIndenter inside the above-mentioned FEI Quanta 250 FEGSEM. For this, fracture cross-sections of samples grown on Si (100) were mechanically polished with a 1 µm diamond lapping film, after which, at a larger region, the Si substrate was chemically removed through etching with a 40 wt.% aqueous KOH at a temperature of 70 °C. The resulting freestanding Ti-B-N thin film region was machined with a focused Ga ion beam (FEI Quanta 200 3D DBFIB) to obtain microcantilevers with dimensions of $7 \cdot w \times w \times w$ (i.e., the length-to-width ratio $l/w = 7$ and the breadth $b = w$) including a pre-notch with the depth a across the breadth by leaving material-bridges on each side of the notch. The cantilever shape was coarse-machined with 3 nA, and the final step was made with 0.5 nA to minimize the impact of FIB damages on the investigation; the pre-notch was milled with 50 pA to reduce geometrical errors and to ensure a small notch-radius. These cantilevers were loaded with a spherical diamond indenter with a tip radius of ~ 1 μm in displacement-controlled mode (5 nm s^{-1}) until fracture. The maximum load P_{max} and the cantilever dimensions were used to calculate K_{IC} after Matoy et al. [31]:

$$K_{1C} = \frac{P_{max} \cdot l}{b \cdot w^{\frac{3}{2}}} \cdot f\left(\frac{a}{w}\right) \tag{5.1}$$

with:

$$f\left(\frac{a}{w}\right) = 1.46 + 24.36 \cdot \left(\frac{a}{w}\right) - 47.21 \cdot \left(\frac{a}{w}\right)^2 + 75.18 \cdot \left(\frac{a}{w}\right)^3 \tag{5.2}$$

A total of 8 cantilever tests per Ti–B–N specimen was conducted, with a success rate of 72 % and w values (after machining) of ~2 μm.

Density function theory (DFT) calculations were conducted employing the Vienna ab initio simulation package (VASP) [32,33] together with projector augmented plane-wave (PAW) pseudopotentials [34] and the Perdew-Burke-Ernzerhof generalized gradient approximation (GGA) [35]. A plane-wave cutoff energy of 600 eV was used together with an automatically generated Γ-centered k-point mesh (length parameter of 60 Å). The equilibrated structure of fcc-TiN (Fm-3m, a = 4.255 Å) served as a building block of a 64-atom (2×2×2) model for $TiN_{1-x}B_x$, $TiN_{1-2x}B_x$, and $Ti_{1-x}NB_x$ solid solutions, corresponding to compositions along the TiN–TiB, TiN–$TiB_{0.5}$, and TiN–BN tie lines, respectively. The B atoms were distributed at the N and Ti sublattice according to the special quasirandom structure (SQS) approach [36]. All structures were fully optimized until forces on atoms were below 10^{-4} eV/Å and the total energies of two successive ionic steps did not differ by more than 10^{-5} eV/supercell.

Polycrystalline Young's moduli, E, of selected solid solutions (with compositions close to the experimental findings) were evaluated from elastic constants obtained by the stress-strain method [37,38]. Assuming a brittle cleavage of the first-neighbor Ti–N/B bonds, cleavage energies, $E_{cl(001)}$, were estimated using the rigid block displacement method [39]. With the directional Young's modulus, $E_{[001]}$, and cleavage energy, $E_{cl(001)}$, we calculated the theoretical K_{IC} according to Griffith's formula [40]:

$$K_{IC(001)} = 2\sqrt{E_{cl(001)} \cdot E_{[001]}} \tag{5.3}$$

As our supercell size allowed deriving eight $E_{cl(001)}$ values for a given B content x in $TiN_{1-x}B_x$ (due to eight (001) planes in each supercell differing only by local distribution of B), we used these to calculate error bars of DFT $K_{IC(001)}$.

5.3 Results and Discussion

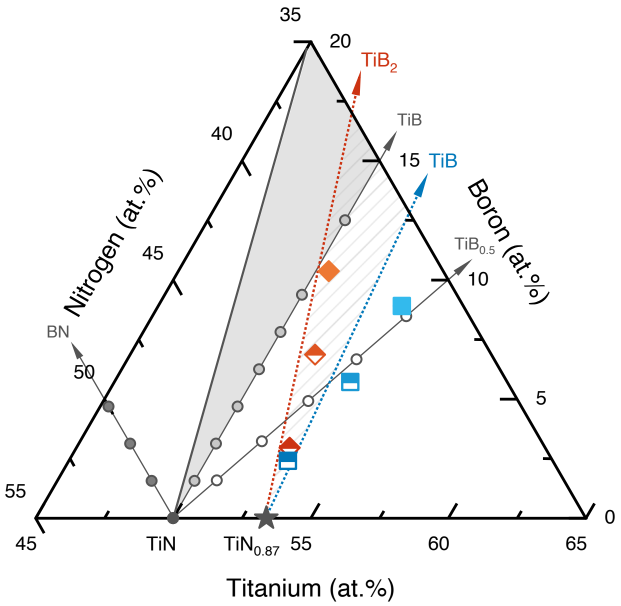

Figure 5.1. Part of the isothermal Ti–B–N phase diagram, including the chemical compositions of the deposited samples as determined by ToF-ERDA (coatings marked as full-filled symbols) and XRF (the four indicated with half-filled symbols). The orange diamond symbols (close to the $TiN_{0.87}$–TiB_2 tie line) represent the TiN–TiB_2 coatings obtained by co-sputtering TiN and TiB_2, while the blue cube symbols (close to the $TiN_{0.87}$–TiB tie line) represent the Ti(N,B) coatings obtained by co-sputtering TiN, TiB_2, and Ti. From the non-reactively sputtered $TiN_{0.87}$ specimen (N/Ti ratio, y, of 0.87, determined with ERDA)—represented by the gray star symbol—to the highest B-containing sample of each series (TiN–TiB_2 and Ti(B,N)), the color becomes lighter. Gray round symbols represent an excerpt from the DFT calculations contrasting the experimental values. White-filled round symbols track $TiN_{1-2x}B_x$ values along the TiN–$TiB_{0.5}$ line, indicating that for each B substituting N, an N-vacancy is "added". Gray-filled symbols correspond to $TiN_{1-x}B_x$ values along the TiN–TiB tie line, where B substitutes N. Dark gray-filled symbols follow $Ti_{1-x}NB_x$ along the TiN–BN tie line, indicating that B-substitutes Ti.

To assess the impact of chemistries either along the TiN–TiB_2 or TiN–TiB tie line on the solubility of B within the TiN-based lattice—and consequently on the evolving microstructure and mechanical properties—we developed two non-reactively prepared Ti–B–N series, one co-sputtered from TiN and TiB_2 targets (referred to as TiN–TiB_2) and one co-sputtered from TiN, TiB_2, and Ti targets (with synchronized sputtering current at the TiB_2 and Ti target, referred to as Ti(B,N) samples), detailly described in the experimental part of the manuscript.

Fig. 5.1 shows that the TiN–TiB_2 samples are chemically close to the TiN–TiB_2 tie line, while the Ti(N,B) samples are close to the TiN–TiB tie line. Consequently, the Ti content of the latter is nearly constant with 52.9, 53.0, 53.6, and 52.7 at.%, for B contents of 0.0, 2.4, 5.7, and 8.9 at.%, respectively. The solely TiN+TiB_2 co-sputtered ones have decreasing Ti contents of 52.9, 52.7, 51.7, and 49.6 at.%, and increasing B-contents of 0.0, 3.0, 6.9, and 10.4 at.% with increasing I_{TiB2} from 0.0 to 0.6 A. The N-deficiency of the non-reactively sputtered film from the TiN target (i.e., the $TiN_{0.87}$–sample) mainly stems from different gas-scattering and sputter-angle distributions of N and Ti [41–43]. Therefore, the chemical compositions of our coatings are closer to the $TiN_{0.87}$–TiB_2 respectively $TiN_{0.87}$–TiB tie-line (bordering the hatched region in Fig. 5.1) than to the TiN-TiB_2 respectively TiN–TiB tie-lines (bordering the gray-shaded region in Fig. 5.1). Fig. 5.1 further shows that the coatings obtained by co-sputtering TiN+TiB_2+Ti deviate further from the corresponding $TiN_{0.87}$-TiB tie line (towards the Ti-corner) with increasing B content than the coatings obtained by co-sputtering TiN+TiB_2 do deviate from their corresponding $TiN_{0.87}$–TiB_2 tie line. The gray round data points in Fig.1 represent the course of our DFT calculations, highlighting the coherence of our deposited coatings and theoretically calculated data points (discussed below).

XRD analyses of the TiN–TiB_2 and Ti(N,B) coatings indicate that both series maintain the single-phase cubic fcc-TiN structure without the formation of other crystalline phases with increasing B content, see Fig. 5.2. While the TiN–TiB_2 coatings show no distinct oriented growth, the Ti(N,B) coatings indicate a 200-oriented growth for both highest B contents (5.7 and 8.9 at.%).

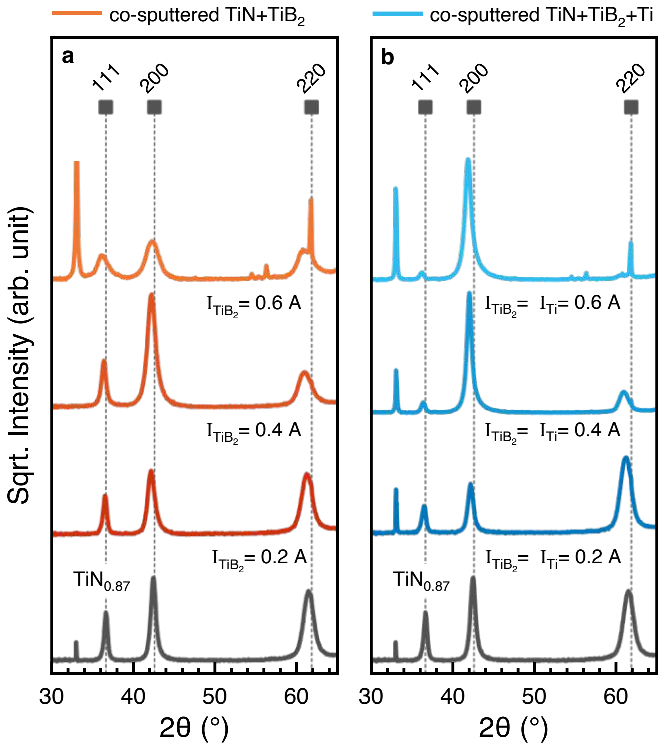

Figure 5.2. X-ray diffraction (XRD) patterns of Ti–B–N coatings co-sputtered from TiN+TiB$_2$ and those co-sputtered from TiN+TiB$_2$+Ti, given in orange and blue, respectively. XRD patterns of the (a) TiN–TiB$_2$ and (b) Ti(N,B) coatings with labeled currents applied to the TiB$_2$ target, I_{TiB2}. For TiN–TiB$_2$ I_{Ti} = 0 A and for Ti(N,B) I_{Ti} was synchronized with I_{TiB2}, I_{TiN} was always 0.75 A. Standard positions of TiN (111), (200), and (220) crystal planes (JCPDS no. 00-038-1420) are indicated.

More detailed peak profile analysis with respect to lattice plane distance d_{200} (Fig. 5.3a) and full width at half maximum Γ_{200} (Fig. 5.3b) highlights significant differences between the two coating series. For TiN–TiB$_2$, d_{200} initially increases from 2.129 to 2.142 Å upon adding 3.0 at% B, after which it slightly decreased again to 2.136 Å (at 10.4 at% B), while Γ_{200} continuously increased. Contrary, the Ti(N,B) samples experience a continuously increasing d_{200} (up to 2.158 Å at 8.9 at% B) while their Γ_{200} stayed at 0.55°±0.08° upon increasing the B content to 8.9 at%, compare Figs. 3a and b. Increasing lattice plane distances of the Ti–N–B coatings with increasing B content indicate that B is incorporated in the TiN lattice, due to the larger covalent bonding radii of B as compared to N [14], rather than being segregated to the grain boundaries. As discussed later, the change towards smaller 2θ is not attributed to increased residual stresses.

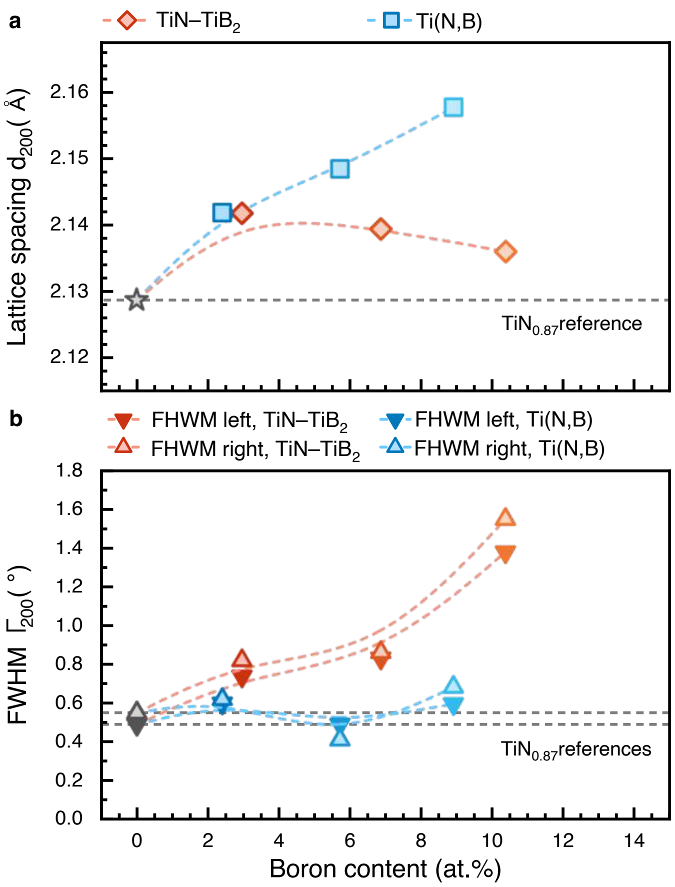

Figure 5.3. (a) Lattice plane distances d_{200} and (b) full width at half maximum (FWHM) of the 200-peak. The orange diamond (a) and triangular (b) symbols represent the TiN–TiB_2 coatings, while the blue cube (a) and triangular symbols represent the Ti(N,B) coatings. The values were determined through peak profile fitting using a Pearson 7 function and an asymmetry type of peaks by split width and shape. The gray star symbol represents the data point for sputtered $TiN_{0.87}$.

More detailed peak profile analysis with respect to lattice plane distance d_{200} (Fig. 5.3a) and full width at half maximum Γ_{200} (Fig. 5.3b) highlights significant differences between the two coating series. For TiN–TiB_2, d_{200} initially increases from 2.129 to 2.142 Å upon adding 3.0 at% B, after which it slightly decreased again to 2.136 Å (at 10.4 at% B), while Γ_{200} continuously increased. Contrary, the Ti(N,B) samples experience a continuously increasing d_{200} (up to 2.158 Å at 8.9 at% B) while their Γ_{200} stayed at 0.55°±0.08° upon increasing the B content to 8.9 at%, compare Figs. 3a and b. Increasing lattice plane distances of the Ti–N–B coatings with increasing B content indicate that B is incorporated in the TiN lattice, due to the larger covalent bonding radii of B as compared to N [14], rather than being segregated to the grain boundaries. As discussed later, the change towards smaller 2θ is not attributed to increased residual stresses.

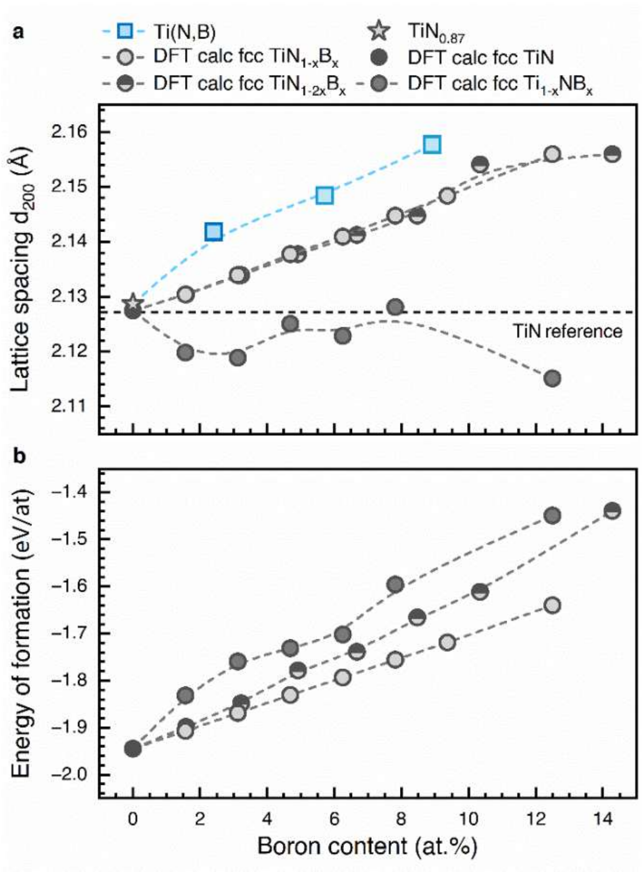

Figure 5.4. DFT-calculated (a) d_{200} lattice spacing, and (b) energy of formation (E_f) as a function of B content for three Ti-B-N structural variants: (i, round gray-filled symbols) $TiN_{1-x}B_x$, where B replaces N at the non-metal sublattice, (ii, round dark gray-filled symbols) $Ti_{1-x}NB_x$, where B replaces Ti at the metal sublattice, (ii, half-filled gray circular symbols) $TiN_{2-x}B_x$, where B occupies the non-metal sublattice with the formation of N-vacancies. The blue trend line (starting from $TiN_{0.87}$, symbolized by a gray star) reflects the Ti(N,B) coatings from Figure 3a.

Consistent with the observed trendline for our Ti(N,B) coatings (Fig. 5.3a), ab initio calculations in Fig. 5.4a show that the d_{200} lattice spacing almost linearly increases with increasing B content in the case of fcc-$TiN_{1-x}B_x$ and fcc-$TiN_{1-2x}B_x$ structures, where the latter exhibits N vacancies (having a very minor effect on d_{200}). Contrarily, the opposite trend—qualitatively inconsistent with our experimental observations for Ti(N,B)—is predicted for fcc-$Ti_{1-x}NB_x$. Mind that we do not expect a perfect quantitative agreement between DFT and experimental d_{200} due to many effects omitted by our DFT models, such as finite temperatures, residual stresses, and the coating's inherent microstructure. In combination with the comparison between ab initio and experimental d_{200} variation, the preferential B-for-N substitution—if B is incorporated in the fcc-TiN lattice—is provided by assessing relative chemical stability, as estimated by (zero Kelvin) formation energy, E_f, see Fig. 5.4b. The least negative E_f of fcc-$Ti_{1-x}NB_x$ (compared to fcc-$TiN_{1-x}B_x$ and fcc-$TiN_{1-2x}B_x$) again points towards that B substitutes for Ti is the least likely scenario. The N-vacancy-containing fcc-$TiN_{1-2x}B_x$ yields E_f slightly above that of fcc-$TiN_{1-x}B_x$. These differences may further diminish at finite temperatures when considering configuration entropy contribution, thus, fcc-$TiN_{1-2x}B_x$ becoming energetically closer (or even favored) over fcc-$TiN_{1-x}B_x$. However, we focus exclusively on fcc-$TiN_{1-x}B_x$ for comparison with our subsequent experimental results. The slightly decreasing d_{200} values of TiN–TiB_2 samples upon increasing their B-content beyond 3.0 at.% in combination with the continuously increased Γ_{200} values, compare Figs. 3a and b, suggest that only approx. 3 at.% B is substituting for N in the TiN_y lattice, while the surplus promotes the formation of an additional X-ray amorphous boundary phase. The mechanisms are similar to what has been studied in detail for TiN–SiN_y [44–46]. Such segregations during film growth interfere with coalescence and promote re-nucleation, leading to smaller crystallite sizes. These would result in larger Γ_{200} values, as observed for TiN–TiB_2. Contrary, the small and nearly constant Γ_{200}, in combination with increasing d_{200} as the B content increases for Ti(N,B), indicates that B is fully incorporated in the crystal lattice (as mentioned above, substituting for N).

To underpin the difference in B solubility for the TiN–TiB_2 respectively Ti(N,B) samples, those with the highest B content were studied in detail by TEM. The 10.4 at.% B-containing TiN–TiB_2 coating's cross-section (Fig. 5.5a) exhibits a compact, dense growth morphology with small grains, on average 18 ± 7 nm; see the dark-field cross-sectional TEM Fig. 5.5b. This additionally shows a more featherlike microstructure. Contrary, the 8.9 at.% B-containing Ti(N,B) coating's cross-section (Fig. 5.5c) exhibits a more columnar growth morphology with column diameters of 54 ± 15 nm on average (see the dark-field image, Fig. 5.5d). Complementary top-view images display the overall morphology of the grains, revealing a refined microstructure with distinct and thick grain boundaries of the TiN–TiB_2 sample (Fig. 5.5e and 5.5f), as a result of segregation effects inhibiting also the columnar growth during film deposition. In contrast, the plane view microstructure of the Ti(N,B) sample showcases larger grains arranged with significantly less-distinct and also much thinner grain boundaries, as shown in Fig. 5.5g and 5.5h. The microstructural differences between the two Ti–B–N coatings suggest that the additional Ti increases the solubility of B within the TiN-lattice during film growth, resulting in reduced segregation processes and thus larger-grained microstructure with prominent columnar growth.

The selected area electron diffraction (SAED) pattern in Fig. 5.6a—obtained with a 750 nm diameter aperture positioned in the center of the cross-section, including the integrated intensity of the full ring pattern—demonstrates a TiN structure without signs of another crystalline phase. The nearly closed diffraction rings, which are relatively broad, mark a small grain size.

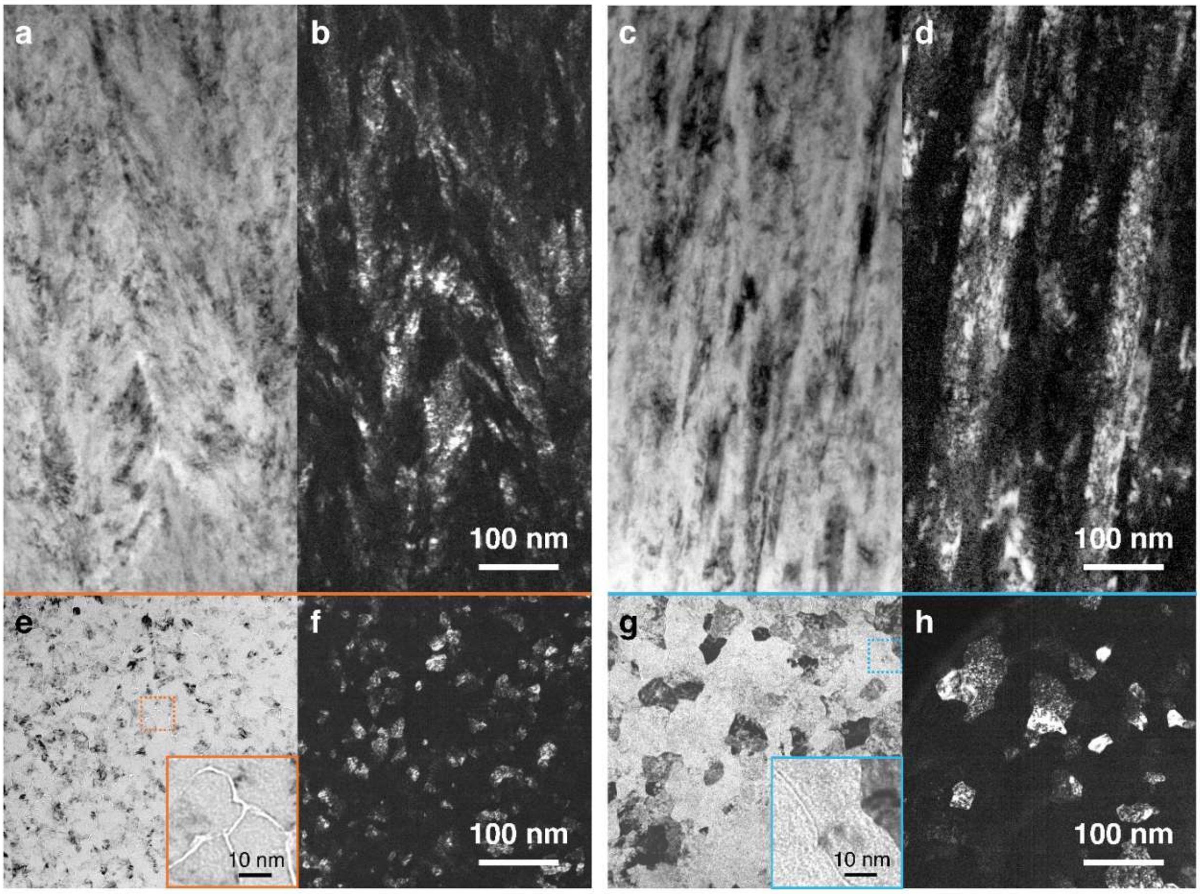

Figure 5.4. TEM investigations of the TiN–TiB_2 coating with 10.4 at.% B. (a) Bright-field TEM image from the middle region of the coating's cross-section. (b) Dark-field TEM variant with 111 and 200 reflections of the same area as in (a). Same for Ti(N,B) coating with 8.9 at.% B. (c) Bright-field and corresponding (d) dark-field TEM image. (e) Top-view TEM bright-field micrograph from a near-surface region of the same TiN-TiB_2 sample and (f) dark-field TEM image highlighting the 111 and 200 reflections of the same area as in (e). The inset in (e) framed in solid-orange is a higher magnification of the section indicated with dashed-orange and illustrates the distinct and thick grain boundaries. Analogous top-view bright-field (g) (with corresponding blue framed inset) and dark-field (h) TEM images for the Ti(N,B) sample with 8.9 at.% B are provided.

Similar to the TiN–TiB_2 coating sample, SAED investigations of Ti(N,B) (Fig. 5.6b, with an overlay of the integrated intensity) show no other crystalline phases than fcc-TiN, in agreement with XRD measurements. Contrary to the TiN–TiB_2 coating, the diffraction rings for Ti(N,B) are sharper with even distinct diffraction spots, indicating (again in agreement with XRD) higher crystalline quality and larger grains/columns. Similar results can be seen in the top-view SAED patterns (obtained with a 200 nm diameter aperture) of both Ti–B–N thin films (compare Fig. 5.6c and 5.6d). The combination of the SAEDs also indicates smaller diffraction ring radii for Ti(N,B) than for TiN–TiB_2, which is equivalent to larger lattice parameters, especially seen when comparing the larger diffraction rings and the peak positions of the integrated intensity.

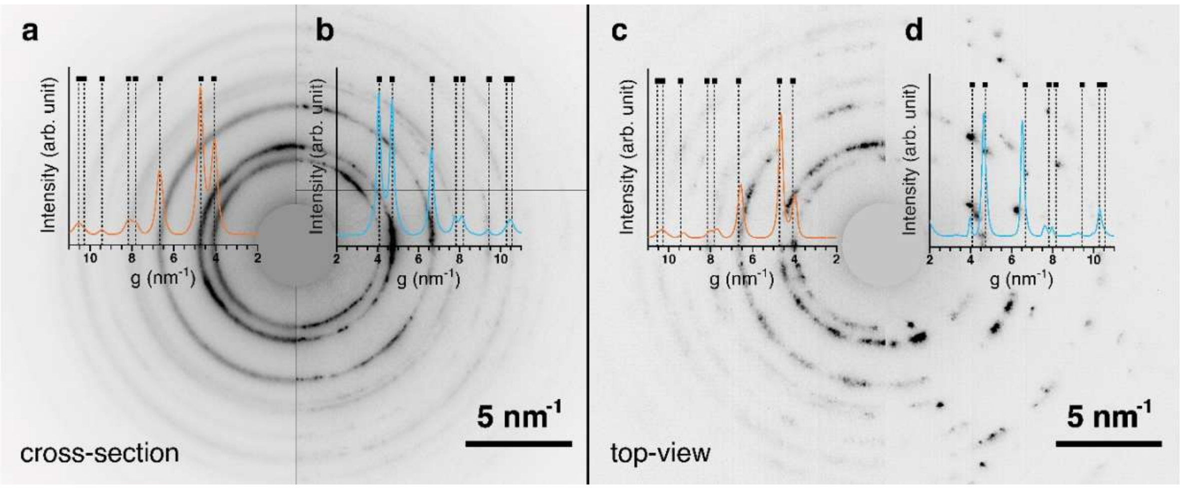

Figure 5.6. Comparative selected-area electron diffraction (SAED) analysis from cross-section TEM-samples of (a) TiN–TiB$_2$ coating with 10.4 at.% B and (b) Ti(N,B) coating with 8.9 at.% B, including an overlay of the integrated intensity in orange (a) and blue (b), respectively (CrystBox [38]). A similar SAED analysis is compared for the top-view TEM samples for TiN–TiB$_2$ (c) in orange and Ti(N,B) (d) in blue. The squared symbols mark the fcc-TiN reference (JCPDS no. 00-038-1420).

These SAED investigations for TiN–TiB$_2$ and Ti(N,B) are in excellent agreement with XRD. Because the SAED is obtained from the cross-section, no preferred growth orientation is visible for the 8.9 at.% B-containing Ti(N,B), contrary to the XRD studies. However, the preferred [200] and [220] orientations can be seen in the SAED obtained from the top-view sample (Fig. 5.6d).

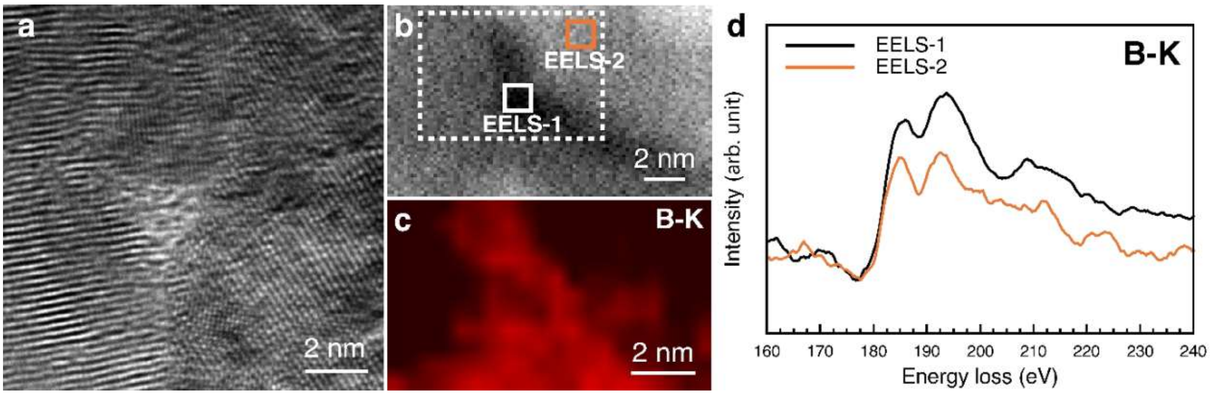

Figure 5.7. (a) Top-view high-resolution TEM (HRTEM) image showing TiN–TiB$_2$ coating with 10.4 at.% B of a triple junction. (b) and (c) show high-angle annular dark-field (HAADF) images covering the area around a triple junction and EELS B-K edge mapping of the corresponding area indicated by a white-lined box, respectively. (d), EELS spectral (B-K edge) results of the triple junction (EELS-1) and the nearby grain (EELS-2).

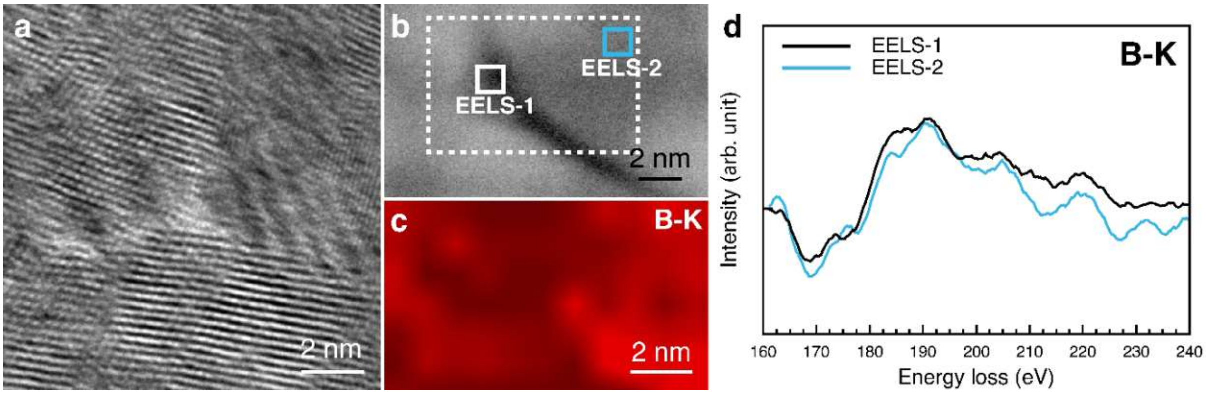

Figure 5.8. (a) Top-view high-resolution TEM (HRTEM) image at the triple junction of the 8.9 at.% B fcc-Ti(N,B) columnar grains. (b) and (c), HAADF imaging and EELS B-K edge mapping of the corresponding white dashed area. (d), EELS spectral (B-K edge) results of a region within the triple junction (EELS-1) and a nearby grain (EELS-2).

To further substantiate the difference in B solubility of the two differently co-sputtered Ti–B–N series, we compare the grain boundary structures and the B distribution of the TiN–TiB_2 and Ti(N,B) coatings with 10.4 and 8.9f at.% B, respectively, by high-resolution top-view TEM investigation. Fig. 5.7a shows the atomic-scale HRTEM image HRTEM image displaying a triple junction with amorphous phases. By EELS mapping the selected area outlined in Fig. 5.7b, the elemental distribution of B is visualized in Fig. 5.7c, significantly highlighting the B enrichment at the triple junction. In addition, individual core-loss spectra (Fig. 5.7d) illustrate an enhanced intensity of the B-K edge at the triple junction compared to the nearby grain. In contrast, the HRTEM image of the Ti(B,N) coating, shown in Fig. 5.8a, shows an overall crystalline microstructure with no amorphous grain boundary phases. Furthermore, the corresponding EELS mapping and individual spectra (Figs. 5.8b-5.8d) do not show any significant B enrichment at the triple junctions of the columnar grains. This observation indicates that B is distributed homogeneously—akin to being fully soluted—in the fcc-Ti(N,B) coating, compared to the pronounced B segregation in the TiN–TiB_2 coating. We further suggest that the B segregation promotes the amorphization of the grain boundary structure.

How these differences in microstructure and soluted B content between TiN–TiB_2 and Ti(N,B) are reflected in the mechanical properties and fracture toughness was studied with nanoindentation and in-situ micromechanical bending tests. Despite the difference in grain size, preferred growth orientation, and soluted B, both coating series show a similar increase in H with increasing B content, Fig. 5.9a. The hardness of TiN–TiB_2 with the highest B content (10.4 at.%) is 36.9±1.9 GPa while that of Ti(N,B) with the highest B content (8.9 at.%) is 37.1±1.9 GPa.

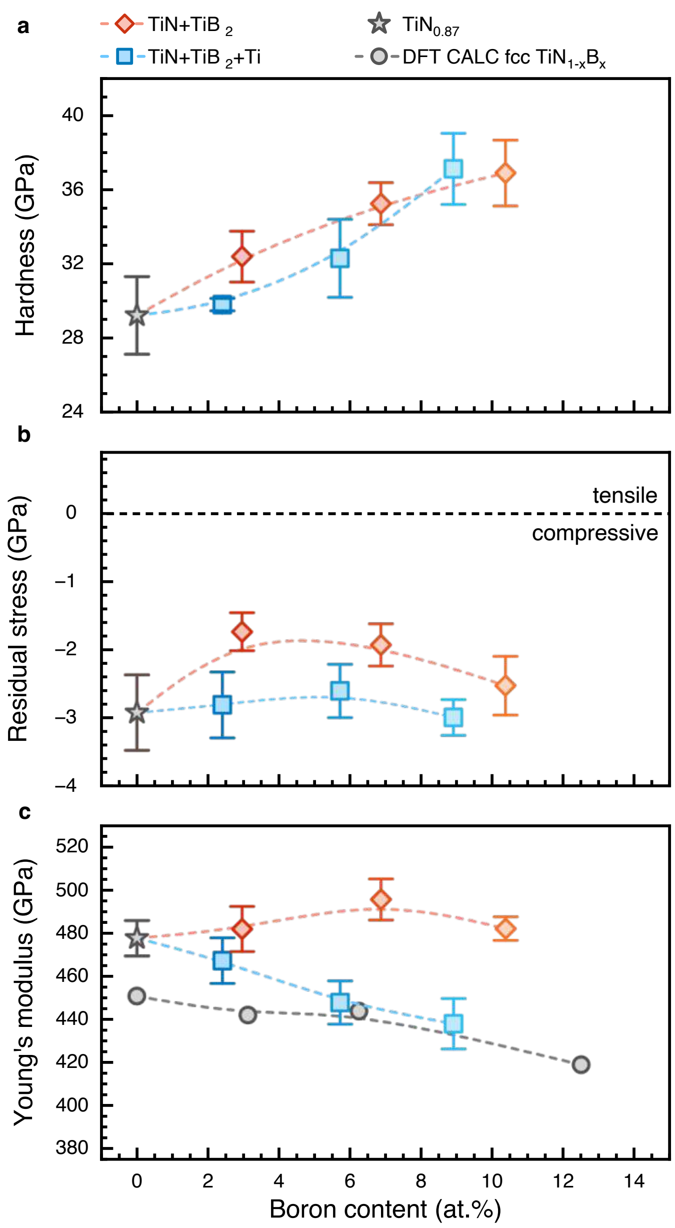

Figure 5.9. Relationship between B content and hardness (a), residual stresses (b), and Young's modulus (c) of TiN–TiB_2 (orange diamond data points) and Ti(N,B) (blue cube data points) thin films. The gray star data point represents $TiN_{0.87}$. The ab initio calculated Young's moduli for fcc-$TiN_{1-x}B_x$ (gray circular symbols) are added to (c).

The unchanged Γ_{200} (Fig. 5.3b) and nearly unchanged compressive residual stresses (Fig. 5.9b) indicate comparable grain sizes and micro stresses for Ti(N,B) regardless of their B content. Hence, the steady shift in peak position, see Fig. 5.3a, is linked to the increasing amount of B incorporated within the lattice rather than caused by residual stresses. On the contrary, the TiN–TiB_2 coatings exhibit an initial decline in compressive residual stresses from -2.92 GPa (for $TiN_{0.87}$) to -1.74 GPa upon adding 3.0 at.% B, after which σ slightly increased to -2.53 (for 10.4 at.% B). Contrary to the residual compressive stresses, the Young's modulus (*E*) only slightly varies for the individual TiN–

TiB_2 coatings but markedly decreases for Ti(N,B) from 478 GPa ($TiN_{0.87}$) to 438 GPa upon increasing the B content to 8.9 at.%, Fig. 5.9c. This decline in E with increasing B content is also captured by ab initio calculations for fcc-$TiN_{1-x}B_x$. Together, these data indicate that the TiN–TiB_2 coatings experience solid solution strengthening (up to 3 at.% B) and grain refinement strengthening. For the Ti(N,B) coatings, solid solution strengthening is dominating up to their maximum B content of 8.9 at.%, because their grain size is essentially unchanged and B is fully soluted, as mentioned above during the discussion of their XRD and TEM results. Ab initio investigations furthermore suggest N with B substitution for these Ti(N,B) samples through their excellent agreement with fcc-$TiN_{1-x}B_x$ structures. As suggested by the classical Fleischer equation, the deviation of the hardness increase from a $B^{0.5}$ dependence suggests other contributions, which could be an additional increase in dislocation density and increased vacancy content.

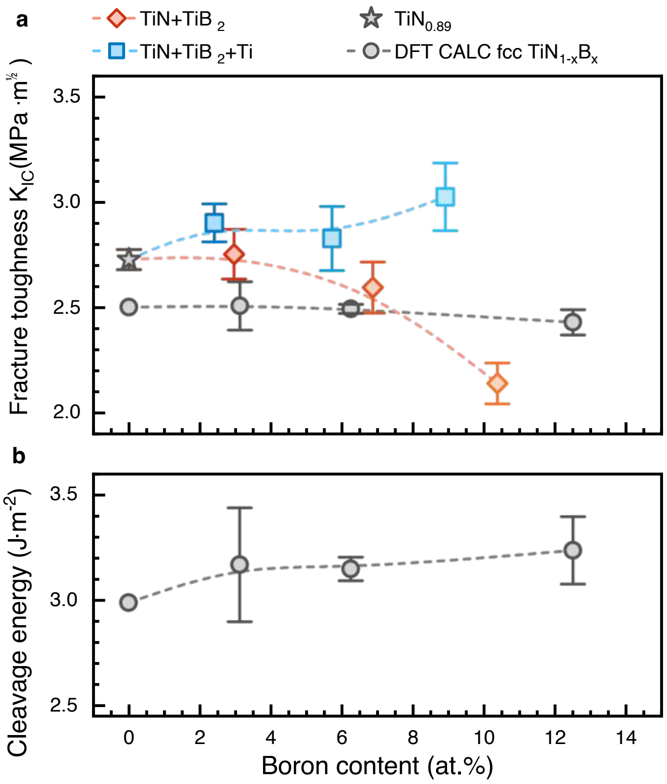

Figure 5.10. (a) Fracture toughness (K_{IC}) for TiN–TiB_2 and Ti(N,B) samples. The gray star symbol represents the data point for $TiN_{0.87}$. (b) DFT-predicted cleavage energy, E_{cl}, of fcc-$TiN_{1-x}B_x$, with error bars representing standard deviation of E_{cl} values for all (100) planes in the simulation cell (due to random distribution of B atoms at the N sublattice, the planes exhibit locally slightly different chemistry). The corresponding calculated $K_{IC(100)}$ is added to (a).

The two coating series, TiN–TiB_2 and Ti(N,B), provide an opposing trend for their fracture toughness K_{IC} with increasing B content. The $TiN_{0.87}$ coating exhibits a K_{IC} of 2.7±<0.1 MPa·$m^{1/2}$, which decreases to 2.1±0.1 MPa·m$^{1/2}$ upon increasing B to 10.4 at.% for the TiN–TiB_2 samples but increases to 3.0±0.2 MPa·m$^{1/2}$ upon increasing B to 8.9 at.% for the Ti(N,B) samples, Fig. 5.10a. The ab initio derived cleavage energy for fcc-$TiN_{1-x}B_x$ also provides such a trend of increasing values with increasing B content, Fig. 5.10b. Again, in addition to d_{200} and Young's modulus, there is a nice agreement between Ti(N,B) samples (with chemistries along the $TiN_{0.87}$–TiB tie line) and the fcc-$TiN_{1-x}B_x$ solid solution where B substitutes for N. Thus, for these Ti(N,B) samples the provided B (here studied up to 8.9 at.%) is fully soluted in the TiN_y lattice. On the contrary, the TiN–TiB_2 coatings with compositions along the $TiN_{0.87}$–TiB_2 tie line can only solute up to approx. 3 at.% B, as suggested by the comparison between XRD and DFT calculated d_{200} of fcc-$TiN_{1-x}B_x$ solid solutions. A surplus in B is accommodated by an amorphous B-rich grain boundary phase, as detected by EELS (Figs. 7b-7d). This excess amount of B at the grain boundaries obviously negatively influences their fracture toughness, because the TiN–TiB_2 sample with the highest B content (10.4 at.%) provides the lowest K_{IC} value of only 2.1±0.1 MPa·m$^{1/2}$, regardless of providing one of the highest H and E values combined with smallest grain size and dense growth morphology. Classically, the combination of such characteristics (while the residual stresses are comparable) would favor an increased fracture toughness if no additional weaker phase is present.

5.4 Summary and Conclusion

This study addressed the open question on B-solubility in TiN_y by developing two Ti–B–N series, one along the TiN–TiB_2 and one along the TiN–TiB tie line. Experimentally, this was achieved through non-reactive co-sputtering of TiN and TiB_2 respectively TiN, TiB_2, and Ti. Accurate assessment of the chemical composition by ERDA proved a N/Ti ratio of 0.87 for the film prepared by non-reactive sputtering the TiN target and a max. B content of 10.4 and 8.9 at.% in the TiN–TiB_2 and Ti(N,B) coatings, respectively. Together with XRF analysis, this showed that while the TiN–TiB_2 films are chemically very close to the $TiN_{0.87}$–TiB_2 line, the Ti(N,B) films deviate from the $TiN_{0.87}$–TiB tie line towards the Ti corner with increasing B content (as the sputtering current applied to the Ti target was synchronized with that applied to the TiB_2 target). The latter should turn out to be decisive for an increased B solubility within TiN_y in the end.

Detailed XRD, TEM, SAED, and HRTEM studies indicated that the only crystalline phase present is fcc-TiN_y-based and that the highest B-containing TiN–TiB_2 and Ti(N,B) film has a grain size of 18±7 nm and column diameter of 54±15 nm, respectively. This 10.4 at.% B containing TiN–TiB_2 was randomly oriented with rather equiaxed grains while the 8.9 at.% B containing Ti(N,B) has a pronounced (200) growth orientation with columnar grains.

Comparison of their d_{200} lattice spacings with theoretical (DFT-predicted) values for fcc-$Ti_{1-x}NB_x$, fcc-$TiN_{1-x}B_x$, and fcc-$TiN_{1-2x}B_x$ pointed out that the Ti(N,B) coatings can completely dissolve the provided 8.9 at.% B in the fcc lattice, whereas this is only possible with about 3 at.% for TiN–TiB_2. Consistently, the full width at half maximum of the XRD peaks, which increased continuously with increasing B content for TiN–TiB_2, but remained constant for Ti(N,B). Finally, our HRTEM and EELS mapping results have conclusively confirmed our XRD results and DFT predictions that only with additional co-sputtering of Ti an fcc-Ti(N,B) solid solution with 8.9 at.% B is achieved–evidenced by the distinct crystalline microstructure and homogeneous B distribution observed in the EELS mapping. In contrast, for the TiN–TiB_2 coating (10.4 at.% B), we showed that most of the B accumulates at the grain boundaries, forming an amorphous B phase, rather than being fully incorporated into the fcc-TiN crystalline grains. This surplus B interferes with coalescence processes during nucleation and growth of the TiN–TiB_2 thin film, resulting in a reduced columnar structure (nearly equiaxed grains for the max. B content) and smaller grains.

The hardness evolution with the B content was similar for both coating series since solid-solution strengthening prevails for Ti(N,B) and grain-refinement strengthening for TiN–TiB_2. In addition to the structural similarities between Ti(N,B) and ab initio fcc-$TiN_{1-x}B_x$, their Young's moduli agreed with the theoretical DFT values and their decrease with increasing B content, too. The TiN–TiB_2 ones provide almost constant values across the B variation studied.

Regardless of the similar hardness values (and trend) but even larger Young's moduli combined with smaller grains, the TiN–TiB_2 coatings provide a lower fracture toughness than Ti(N,B). The difference was most pronounced for the highest B-containing coatings because K_{IC} increases with B for Ti(N,B) to 3.0 ± 0.2 $MPa\cdot m^{1/2}$ but decreases for TiN–TiB_2 to 2.1 ± 0.1 $MPa\cdot m^{1/2}$. For B-free fcc-$TiN_{0.87}$, $K_{IC} = 2.7\pm<0.1$ $MPa\cdot m^{1/2}$.

Based on our findings, successfully incorporating advantageous elements into crystal lattices must account for their needed space. In this case, the larger B atom relative to N requires understoichiometric TiN.

5.5 References

[1] J. -E. Sundgren, A. Rockett, J.E. Greene, U. Helmersson, Microstructural and microchemical characterization of hard coatings, Journal of Vacuum Science & Technology A: Vacuum, Surfaces, and Films. 4 (1986) 2770–2783.

[2] I. Petrov, L. Hultman, U. Helmersson, J.E. Sundgren, J.E. Greene, Microstructure modification of TiN by ion bombardment during reactive sputter deposition, Thin Solid Films. 169 (1989) 299–314.

[3] J. Neidhardt, Z. Czigány, B. Sartory, R. Tessadri, M. O'Sullivan, C. Mitterer, Nanocomposite Ti-B-N coatings synthesized by reactive arc evaporation, Acta Mater. 54 (2006) 4193–4200.

[4] P.H. Mayrhofer, M. Stoiber, Thermal stability of superhard Ti-B-N coatings, Surf Coat Technol. 201 (2007) 6148–6153.

[5] P.H. Mayrhofer, M. Stoiber, C. Mitterer, Age hardening of PACVD TiBN thin films, Scr Mater. 53 (2005) 241–245.

[6] P.H. Mayrhofer, C. Mitterer, J.G. Wen, I. Petrov, J.E. Greene, Thermally induced self-hardening of nanocrystalline Ti-B-N thin films, J Appl Phys. 100 (2006).

[7] W. Gissler, Structure and properties of Ti-B-N coatings, Surf Coat Technol. 68 (1994) 556–563.

[8] R.F. Zhang, S.H. Sheng, S. Veprek, Stability of Ti-B-N solid solutions and the formation of nc-TiN/a-BN nanocomposites studied by combined ab initio and thermodynamic calculations, Acta Mater. 56 (2008) 4440–4449.

[9] W. Sun, C.J. Bartel, E. Arca, S.R. Bauers, B. Matthews, B. Orvañanos, B.R. Chen, M.F. Toney, L.T. Schelhas, W. Tumas, J. Tate, A. Zakutayev, S. Lany, A.M. Holder, G. Ceder, A map of the inorganic ternary metal nitrides, Nat Mater. 18 (2019) 732–739.

[10] M. Aykol, S.S. Dwaraknath, W. Sun, K.A. Persson, Thermodynamic limit for synthesis of metastable inorganic materials, 2018.

[11] B. Cordero, V. Gómez, A.E. Platero-Prats, M. Revés, J. Echeverría, E. Cremades, F. Barragán, S. Alvarez, Covalent radii revisited, Journal of the Chemical Society. Dalton Transactions. (2008) 2832–2838.

[12] R.L. Fleischer, Substitutional solution hardening, Acta Metallurgica. 11 (1963) 203–209.

[13] W. Hume-Rothery, J Inst Metals, 1926, 35, 319–335.

[14] S. Yang, T. Guo, X. Yan, K. Gao, X. Pang, High-density twin boundaries in transition metal nitride coating with boron doping, Acta Mater. 255 (2023).

[15] E.O. Hall, The Deformation and Ageing of Mild Steel: III Discussion of Results, Proceedings of the Physical Society. Section B. 64 (1951) 747–747.

[16] N.J. Petch, The influence of grain boundary carbide and grain size on the cleavage strength and impact transition temperature of steel, Acta Metallurgica. 34 (1986) 1387–1393.

[17] H.D. Männling, D.S. Patil, K. Moto, M. Jilek, S. Veprek, Thermal stability of superhard nanocomposite coatings consisting of immiscible nitrides, Surf Coat Technol. 146–147 (2001) 263–267.

[18] P.H. Mayrhofer, H. Willmann, C. Mitterer, Recrystallization and grain growth of nanocomposite Ti–B–N coatings, Thin Solid Films. 440 (2003) 174–179.

[19] R. Hahn, A. Tymoszuk, T. Wojcik, A. Kirnbauer, T. Kozák, J. Čapek, M. Sauer, A. Foelske, O. Hunold, P. Polcik, P.H. Mayrhofer, H. Riedl, Phase formation and mechanical properties of reactively and non-reactively sputtered Ti-B-N hard coatings, Surf Coat Technol. 420 (2021).

[20] I. El Azhari, J. Garcia, M. Zamanzade, F. Soldera, C. Pauly, L. Llanes, F. Mücklich, Investigations on micro-mechanical properties of polycrystalline Ti(C,N) and Zr(C,N) coatings, Acta Mater. 149 (2018) 364–376.

[21] M. Tkadletz, N. Schalk, A. Lechner, L. Hatzenbichler, D. Holec, C. Hofer, M. Deluca, B. Sartory, A. Lyapin, J. Julin, C. Czettl, Influence of B content on microstructure, phase composition and mechanical properties of CVD Ti(B,N) coatings, Materialia (Oxf). 21 (2022).

[22] Y.H. Lu, P. Sit, T.F. Hung, H. Chen, Z.F. Zhou, K.Y. Li, Y.G. Shen, Effects of B content on microstructure and mechanical properties of nanocomposite Ti–B[sub x]–N[sub y] thin films, Journal of Vacuum Science & Technology B: Microelectronics and Nanometer Structures. 23 (2005) 449.

[23] C. Kainz, N. Schalk, M. Tkadletz, C. Mitterer, C. Czettl, The effect of B and C addition on microstructure and mechanical properties of TiN hard coatings grown by chemical vapor deposition, Thin Solid Films. 688 (2019).

[24] A.B. Mei, H. Kindlund, E. Broitman, L. Hultman, I. Petrov, J.E. Greene, D.G. Sangiovanni, Adaptive hard and tough mechanical response in single-crystal B1 VNx ceramics via control of anion vacancies, Acta Mater. 192 (2020) 78–88.

[25] P. Ström, D. Primetzhofer, Ion beam tools for nondestructive in-situ and in-operando composition analysis and modification of materials at the Tandem Laboratory in Uppsala, Journal of Instrumentation. 17 (2022).

[26] M. Janson, CONTES conversion of time-energy spectra—A program for ERDA data analysis, (2004).

[27] R.M. Langford, M. Rogers, In situ lift-out: Steps to improve yield and a comparison with other FIB TEM sample preparation techniques, Micron. 39 (2008) 1325–1330.

[28] W.C. Oliver, G.M. Pharr, An improved technique for determining hardness and elastic modulus using load and displacement sensing indentation experiments, J Mater Res. 7 (1992) 1564–1583.

[29] A.C. Fischer-Cripps, Critical review of analysis and interpretation of nanoindentation test data, Surf Coat Technol. 200 (2006) 4153–4165.

[30] G.C.A.M. Janssen, M.M. Abdalla, F. van Keulen, B.R. Pujada, B. van Venrooy, Celebrating the 100th anniversary of the Stoney equation for film stress: Developments from polycrystalline steel strips to single crystal silicon wafers, Thin Solid Films. 517 (2009) 1858–1867.

[31] K. Matoy, H. Schönherr, T. Detzel, T. Schöberl, R. Pippan, C. Motz, G. Dehm, A comparative micro-cantilever study of the mechanical behavior of silicon based passivation films, Thin Solid Films. 518 (2009) 247–256.

[32] G. Kresse, J. Furthmüller, Efficient iterative schemes for ab initio total-energy calculations using a plane-wave basis set, Phys Rev B. 54 (1996) 11169–11186.

[33] G. Kresse, D. Joubert, From ultrasoft pseudopotentials to the projector augmented-wave method, Phys Rev B. 59 (1999) 1758–1775.

[34] W. Kohn, L.J. Sham, PHYSICAL REVIEW Self-Consistent Equations Including Exchange and Correlation Effects*, n.d.

[35] J.P. Perdew, K. Burke, M. Ernzerhof, Generalized Gradient Approximation Made Simple, 1996.

[36] D. Nöger, A command line tool written in Python/Cython for finding optimized SQS structures, (2019).

[37] Y. Le Page, P. Saxe, Symmetry-general least-squares extraction of elastic data for strained materials from ab initio calculations of stress, Phys Rev B Condens Matter Mater Phys. 65 (2002) 1–14.

[38] R. Yu, J. Zhu, H.Q. Ye, Calculations of single-crystal elastic constants made simple, Comput Phys Commun. 181 (2010) 671–675.

[39] P. Lazar, J. Redinger, R. Podloucky, Density functional theory applied to VN/TiN multilayers, Phys Rev B Condens Matter Mater Phys. 76 (2007).

[40] M. Bielawski, K. Chen, Computational evaluation of adhesion and mechanical properties

of nanolayered erosion-resistant coatings for gas turbines, J Eng Gas Turbine Power. 133 (2011).

[41] K. Xu, Y.L. Meng, S.M. Liu, J. Tan, Controllable Optical Characteristics of TiN Films Prepared by Magnetron Sputtering, in: Lecture Notes in Electrical Engineering, Springer Science and Business Media Deutschland GmbH, 2021: pp. 131–138.

[42] D. Martínez-Martínez, C. López-Cartes, A. Fernández, J.C. Sánchez-López, Exploring the benefits of depositing hard TiN thin films by non-reactive magnetron sputtering, in: Appl Surf Sci, Elsevier B.V., 2013: pp. 121–126.

[43] P.H. Mayrhofer, F. Kunc, J. Musil, C. Mitterer, A comparative study on reactive and non-reactive unbalanced magnetron sputter deposition of TiN coatings, 2002.

[44] L. Shizhi, S. Yulong, P. Hongrui, Ti-Si-N Films Prepared by Plasma-Enhanced Chemical Vapor Deposition, 1992.

[45] S. Vepřek, S. Reiprich, L. Shizhi, Superhard nanocrystalline composite materials: The TiN/Si3N4 system, Appl Phys Lett. (1995) 2640.

[46] J. Patscheider, T. Zehnder, M. Diserens, Structure-performance relations in nanocomposite coatings, 2001.

6 Strategic Lattice Manipulation in Transition Metal Nitrides for Improved Solubility

In this study, we propose a new concept for achieving metastable ternary transition metal nitride solid solutions, focusing on face centered cubic (fcc) structured Ti(N,B) as a model system. Combining non-reactive magnetron sputtering with computational analysis, we develop a microalloying strategy to manipulate the metallic sublattice, thereby influencing the solubility of B in the non-metal sublattice. We show that imposed tensile strain on the fcc-TiN lattice facilitates the solubility of B, with a 1.5% strain enabling the incorporation of ~28.5 at.% B at the non-metal sublattice. Conversely, compressive strain hinders the formation of the fcc-Ti(N,B) solid solution, highlighting the importance of lattice manipulation in controlling solubility. At the same time, our experimental findings reveal that adding larger atoms, such as Zr, to the metal sublattice enhances the solubility of B in fcc-TiN more effectively (~2 at.% Zr proves to be sufficient to solute 10 at.% B in the fcc-TiN lattice) than smaller atoms, like Cr or similar-sized Ti atoms. The size effect of the alloying atoms on the B solubility is further supported by radial distribution function analysis, showing lower local lattice distortions for Zr compared to Cr.

6.1 New Concept

We present a new perspective on synthesis challenges inherent to most ternary transition metal nitride solid solutions. Using face centered cubic (fcc) structured Ti(N,B) as a model system, we explore new avenues for achieving a complete solubility of non-metal alloying elements, particularly B, in the fcc-TiN lattice. Through a combination of physical vapor deposition techniques and ab initio calculations, we propose a microalloying approach to manipulate the metallic sublattice and thereby influence the solubility of B in the non-metal sublattice. By systematically adding smaller or larger atoms to the metal lattice, we account for the size-dependent effects of the alloyed atoms and provide new insights into the spatial constraints limiting the solubility of B in the fcc-TiN lattice. Our microalloying approach highlights the importance of the space conditions in the binary host lattice that are critical for achieving ternary solid solutions from a thermodynamic stability viewpoint. Bridging the gap between theory and experiment, we propose that this synthesis strategy can be generalized beyond the material class of ternary transition metal nitrides.

6.2 Introduction

The growing demand for materials tailored to the dynamic needs of diverse industries continually pushes the boundaries of modern materials science. In the field of ceramic hard coatings, forming solid solutions contribute to the development of materials with improved mechanical and thermal properties—particularly crucial in industries where wear, corrosion, and further environmental conditions can impact the functionality and reliability of materials and equipment. By carefully selecting and controlling the composition of the solid solution, engineers can design coatings with desired characteristics, such as hardness, thermal stability, and chemical inertness[1–5]. Especially in applications demanding superior durability and performance, transition metal nitride hard coatings have emerged as a vital subset, renowned for their exceptional hardness and wear resistance[6–10]. Mainly, titanium nitride (TiN)—achieved through plasma-assisted PVD techniques[11–14]—stands out as a paradigm material system that evolved immensely from its initial use as a protective layer for cutting tools in the mid-20th century to one of today's most prominent and widely used (and studied) coating system in industry (and science), driven by its exceptional range of advantageous functionalities[15–17]. Based on its crystal structure TiN can be explained as an interstitial compound. According to Hägg's rule[18,19], the smaller N atoms occupy the octahedral sites (interstitials) between the larger atoms (Ti) in a face centered cubic (fcc) structured arrangement (according to the NaCl prototype; therefore TiN sometimes has the pre-index of rs for rocksalt). The mix of strong covalent Ti–N and metallic Ti–Ti bonding is what gives TiN high hardness and electrical conductivity[20].

The alloy design of fcc-TiN-based coatings, has demonstrated success with well-established ternary systems such as fcc-(Ti,Al)N[21,22] alongside fcc-Ti(N,C)[23], where solid solutions form upon the introduction of additional elements to the titanium nitride matrix. In case of ternary transition metal nitrides system, we have to compare substitution on the metal-sublattice with substitution on the non-metal-sublattice[3]: For fcc-(Ti,Al)N, Al randomly substitutes for Ti on the metal-sublattice[24,25], whereas the non-metal C atoms replace N in the non-metal sublattice[26,27]. In the case of Ti–Si–N[28], the reverse is desirable; ideally, no Si-solubility should occur in this material system to precipitate a Si-rich phase at the grain boundaries and thus lead to Hall-Petch hardening[29–31]. The synthesis of ternary transition metal nitride thin films is an enticing prospect, as it offers the potential of superior properties compared to their thermodynamically stable binary phases[32,33]. The inherently meta-stable nature of many ternary nitride phases, however, complicates their feasibility[34–36]. Although their structural arrangement does not align with the lowest-energy states—akin to points above the convex hull—metastable phases can persist due to kinetic barriers that impede their transition to the thermodynamically stable configuration[37–41]. Modern methods of plasma-assisted Physical Vapor Deposition (PVD) techniques facilitate the formation of metastable phases due to limited kinetics and non-equilibrium conditions during deposition, explained by pioneering research from W.-D. Münz[42–44], A. Anders[45,46], and D. Depla[47–49]. These conditions of PVD contribute to its popularity for transition metal nitride synthesis by enabling controlled stoichiometry and the ability to fine-tune film properties. While PVD techniques offer unique pathways to access metastable phases[39,40], our research focuses on challenges in synthesizing single-phase fcc-Ti(N,B) thin films. Unlike for ternary nitride systems such as fcc-(Ti,Al)N, where vapor deposition techniques allow for substituting even ~80 at% of Ti with Al on the metal sublattice[24,50], the solubility of B within the fcc structure of Ti(N,B)[51] coatings is rather limited and preferably TiN+TiB_2 or TiN+BN nanocomposites or mixtures thereof with (amorphous) B-rich grain boundary phases form[3,52–56]. We previously revealed that attaining improved solubility of B within fcc-TiN requires a deviation from the TiN–TiB tie line towards Ti-richer compounds, (i.e., the promoted formation of vacancies on the non-metal sublattice). This deviation was accomplished by non-reactive co-sputtering a Ti target alongside TiN and TiB_2 targets, where 8.9 at.% B could be fully soluted in the fcc-TiN lattice (for a non-metal-to-metal = 1:1 stoichiometry, this equals that the non-metal sublattice holds 17.8 at.% B)[52]. In contrast, reactive sputtered coatings tend towards compositions along the TiN–BN tie line[57]. The oversupply of less reactive N_2^+ ions (relative to Ti^+ and Ti^{2+}) along with an excessive presence of N_2 inhibits the formation of the fcc-Ti(N,B) solid solution and instead forms BN-rich boundary phases[58]. We further concluded that accounting for the required space is necessary when fully incorporating B (0.84 Å)[59] into the fcc-TiN lattice due to its larger size, i.e., larger covalent radius, compared to N (0.71 Å)[59].

By substituting the larger B atoms for the smaller N atoms on the octahedral site, being the preferred lattice site as confirmed by DFT calculations[52,53], the lattice dimensions expand with increasing B concentration. Consequently, this lattice expansion leads to an increase in the lattice parameter—indicated by a shift towards smaller 2θ values in the X-ray diffraction (XRD) patterns—referring to fcc-TiN (a=4.255 Å, calculated). Excess B, however, segregates at the grain boundaries, refining the microstructure of the coating. This incomplete B solubility is also reflected in the XRD analysis, where broader peaks and relatively smaller (or absent) peak shifts appear[52]. Building on our previous research, here we address the confined spatial conditions for B at the non-metal sublattice that inhibit the formation of the fcc-Ti(N,B) solid solution. Specifically, we aimed at non-reactive deposition of Ti–Me–B–N coatings (Me=Ti, Zr, or Cr) by strategically increasing the metal content (alloying Ti, Zr, or Cr to a Ti–B–N composite target), while keeping the B content at ~10 at%. Supported by ab initio density functional theory calculations, we explain how the manipulation of the metal sublattice by smaller or larger atoms affects the solubility of B in the non-metal sublattice. Unravelling the size-dependent effects of alloyed atoms on the local stress state of the lattice—where fcc-Ti(N,B) serves as a model system—we provide a new target-driven microalloying concept to facilitate the synthesis of metastable ternary nitrides.

6.3 Experimental

6.3.1 Thin Film Deposition

The 24 different Ti–Me–B–N (Me = Ti, Cr, or Zr) coatings, in addition to one Ti–B–N coating (prepared from the plain TiN+TiB_2+Ti composite target without additional alloying, referred to as $TiB_{0.2}N_{0.8}$), were deposited on single crystalline sapphire substrates $(1\bar{1}02)$ 10×10×0.53 mm^3 using a modified Leybold Hereaus LH Z400 MS PVD machine equipped with a 3" unbalanced magnetron source holding a TiN+TiB_2+Ti composite target with an elemental composition of 50 at.% Ti, 40 at.% N, and 10 at.% B, sourced from Plansee Composite Materials GmbH. To facilitate a controlled variation in the deposition of coatings towards higher metal concentrations, we placed an increasing number of Ti, Cr, or Zr pieces (~3×3×3 mm^3) on the target's racetrack. Following ultrasonic cleaning in acetone and ethanol for 5 min each, the substrate preparation commenced inside the chamber after reaching the base pressure below $1\cdot10^{-4}$ Pa ($1\cdot10^{-6}$ mbar). The substrates were thermally cleaned at ~400 °C for 25 min, and afterwards Ar-ion-etched for 15 min at an Ar pressure (60 sccm Ar-flow) of 67 Pa. At the same time, a negative pulsed voltage of 150 V (150 kHz and 2496 ns on time) was applied to the non-rotating substrate holder with a target-to-substrate distance of 38 mm. Subsequently, all coatings were obtained by non-reactive DC magnetron sputtering at 400 °C by continuously operating the 3-inch Ti–B–N target in current-controlled mode at $I_{Ti\text{–}B\text{–}N}$=0.5 A and keeping the Ar pressure at 0.4 Pa (33 sccm Ar-flow). The deposition time was adjusted between 75 and 90 min to prepare coatings with a thickness t of ~3 μm.

6.3.2 Chemical Analysis

We determined the chemical composition of our coatings (individual elemental concentrations are listed in the Supplementary materials in Table S1) by conducting Time-of-Flight Elastic Recoil Detection Analysis (ToF-ERDA) at the 5 MV Pelletron Tandem accelerator at Uppsala

University[60], employing $^{127}I^{8+}$ projectiles with a primary energy of 36 MeV. The beam incident angle was 67.5° to the surface normal, with recoils reaching the detector at a 45° angle relative to the direction of the incident beam. The raw experimental data were processed using the CONTES software package[61]. Total systematic and statistical uncertainties were estimated to be below 5% of the deduced value for the major constituents. Additional chemical information was obtained from X-ray fluorescence (XRF) measurements using a PANalytical AxiosmAX-Advanced spectrometer with a rhodium (Rh) X-ray tube operating at 50 kV and 55 mA under vacuum conditions. The instrument was calibrated using the results of the ERDA-analyzed samples.

6.3.3 Structural Analysis

For structural characterization of the thin films, we performed X-ray diffraction using a PANalytical Empyrean (θ-θ diffractometer) with Cu($K\alpha_{1,2}$) radiation, equipped with a GaliPIX3D detector. X-ray diffraction patterns were collected over a 2θ angle ranging from 5° to 120° with respect to the sample surface. The lattice plane distances, d_{200}, and full width at half maximum, Γ_{200}, of the 200-peak were determined through peak profile fitting in MalvernPanalytical's HighScore plus software[62] using a Pearson 7 function and an asymmetry type of peaks by splitting width and shape. All diffraction patterns were processed by aligning the prominent [024] sapphire substrate peak to its reference position at 2θ=52.534° (JCPDS no. 00-035-0803)[63].

6.3.4 DFT Calculations

Density function theory (DFT) calculations were performed using the Vienna ab initio simulation package (VASP) [64,65], combined with projector augmented plane-wave (PAW) pseudopotentials[66] and the Perdew-Burke-Ernzerhof generalized gradient approximation (GGA)[67]. These calculations were carried out with a plane-wave cutoff energy of 600 eV and employed an automatically generated Γ-centered k-point mesh with a length parameter of 60 Å.

The 4-atom equilibrated structure of fcc-TiN (Fm-3m, with a lattice constant of 4.255 Å) served as basis for a 64-atom (2×2×2) model for fcc-$TiN_{1-x}B_x$ as well as fcc-$Ti_{1-y}Me_yN_{1-x}B_x$ solid solutions, where B replaces N on the non-metal sublattice and Me={Cr,Zr} replaces Ti on the metal sublattice. The distribution of B atoms followed the special quasirandom structure (SQS) approach[68].

The structures underwent a full optimization (volume, shape, and ionic positions) until forces on atoms were reduced to below 10^{-4} eV/Å, and the total energies of two consecutive ionic steps exhibited a difference of less than 10^{-5} eV per supercell. For volumetric tension/compression simulations, the supercells were kept at a fixed volume and only the atoms inside were allowed to relax.

Formation energy, E_f, was evaluated consistently with our previous work[52].

The radial distribution functions (RDFs) were calculated using the OVITO package[69]. Subsequently, the misfit strain, ε, was evaluated by fitting a Gaussian function to obtain the average bond distance of two individual bonds, the first nearest neighbor distance of the solvent (fcc-TiN lattice) and solute (B), Ti–N and Ti–B, for each material system, and calculated by $\varepsilon = d_{\text{Ti-B}} - d_{\text{Ti-N}}) / d_{\text{Ti-N}}$[70].

6.4 Results

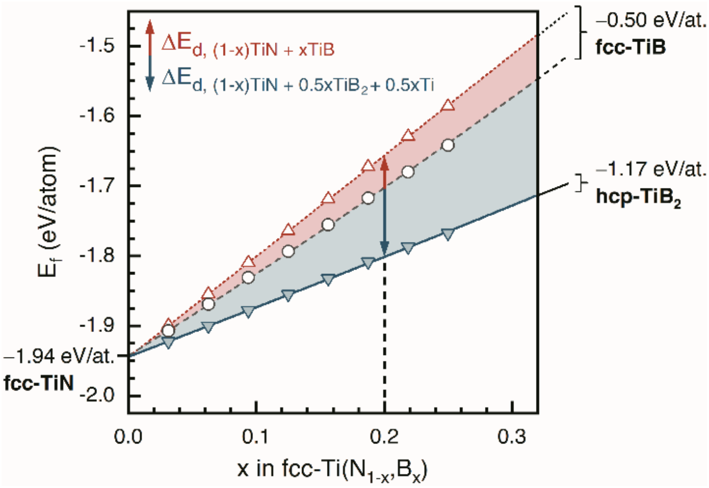

Figure 6.1. Thermodynamic stability quantified by the formation energy, E_f, of fcc-Ti$N_{1-x}B_x$ compared to its competing decomposition products. The black circular symbols denote E_f for fcc-Ti$N_{1-x}B_x$ solid solution along the quasi-binary TiN–TiB tie line. For each composition (shown as a function of x), the location of the energetically more (or less) favorable binary components fcc-TiN+hcp-TiB_2+hcp-Ti (or fcc-TiN+fcc-TiB) is indicated as blue (or red) triangles. The vertical distance between the points, illustrated by a blue and red arrow for x=0.2, equals ΔE_f. Note that the decomposition products are stoichiometrically balanced according to the elemental composition of the educt fcc-Ti$N_{1-x}B_x$.

To visualize the thermodynamic landscape, we have constructed a quasi-binary convex hull phase diagram (illustrated in Fig. 6.1), highlighting the metastable nature of the fcc-Ti(N,B) solid solution. Our ab initio Density Functional Theory (DFT) calculations, reveal that the fcc-Ti$N_{1-x}B_x$ solid solution is energetically unfavorable compared to the stoichiometrically balanced combination of fcc-TiN, hexagonal close packed (hcp) TiB_2, and hcp-Ti (representing the thermodynamically stable state). Notably, the decomposition reaction into fcc-TiN and fcc-TiB is even less energetically favorable than the formation of the ternary solid solution, considering that fcc-TiB itself is a metastable compound[71]. In Fig. 6.1, we highlight the impact of B content on the synthesis of fcc-Ti(N,B) by directly correlating the increasing B-to-N ratio with the rising energy barrier (ΔE_f) that needs to be overcome to achieve the ternary solid solution. The energy gap between the fcc-$TiN_{1-x}B_x$ and its decomposition components (illustrated in blue) widens steadily with increasing B content, approaching the maximum for x=1 ($E_{f,\text{hcp-TiB}_2}$-$E_{f,\text{fcc-TiB}}$=0.67 eV/at.). For 10 at.% B (equivalent to 20 at.% on the non-metal sublattice), the fitted data yield a difference of 0.10 eV/at. Although PVD inherently provides a kinetic handle to overcome small ΔE_f, 0.10 eV/at. is rather large for standard PVD processes but not impossible. Considering the E_f barrier of ~0.18 eV/at. between the rock-salt (B1) and wurtzite (B4) AlN allotropes[72] we know that B1 AlN can form e.g. via the template effect from fcc-TiN in a superlattice[73]. Although advances in computational materials science enable to predict the stability of solid solutions[5,35,36,74,75], empirical solubility rules stated by Pauling[76–78], Hume-Rothery[79–81], and Hägg[18,19] further allow reasonably estimating the solubility of crystalline materials. Based on Hägg's rule—which predicts the stability of the closest packing for interstitial compounds (Hägg phases)—the ratio of atomic radii of the non-metal and transition-metallic components (r_x/r_{Me}) must be within the range of 0.41–0.59. The closest packed TiB (r_x/r_{Me}=0.67) clearly exceeds the limit of 0.59. To meet the limit values of the rule, we used the atomic radii published by Hägg in 1931[19]. Consequently, it is clear that incorporating B into the fcc-TiN lattice requires a larger metal atom radius, i.e., a larger fcc lattice, further illustrated by comparing the lattice parameters between fcc-TiN (a=4.255 Å) and fcc-TiB (a=4.534 Å), both calculated by DFT.

Having outlined the challenges of synthesizing fcc-Ti(N,B) thin films, we further employ ab initio DFT calculations to address the spatial constraints. Fig. 6.2 compares formation energies, E_f, and stresses, $\sigma_{[100]}$, of fcc-Ti(N,B) solid solutions under volumetric tension/compression to those of the fully relaxed system. Specifically, the lattice parameter, a, is fixed to a 1.5% or 3% larger respectively smaller value with respect to that of the equilibrium fcc-TiN (i.e., a={4.319; 4.383} Å and a={4.191; 4.127} Å model the system under tensile and compressive strain, respectively, where the reference fcc-TiN exhibits a=4.255 Å.

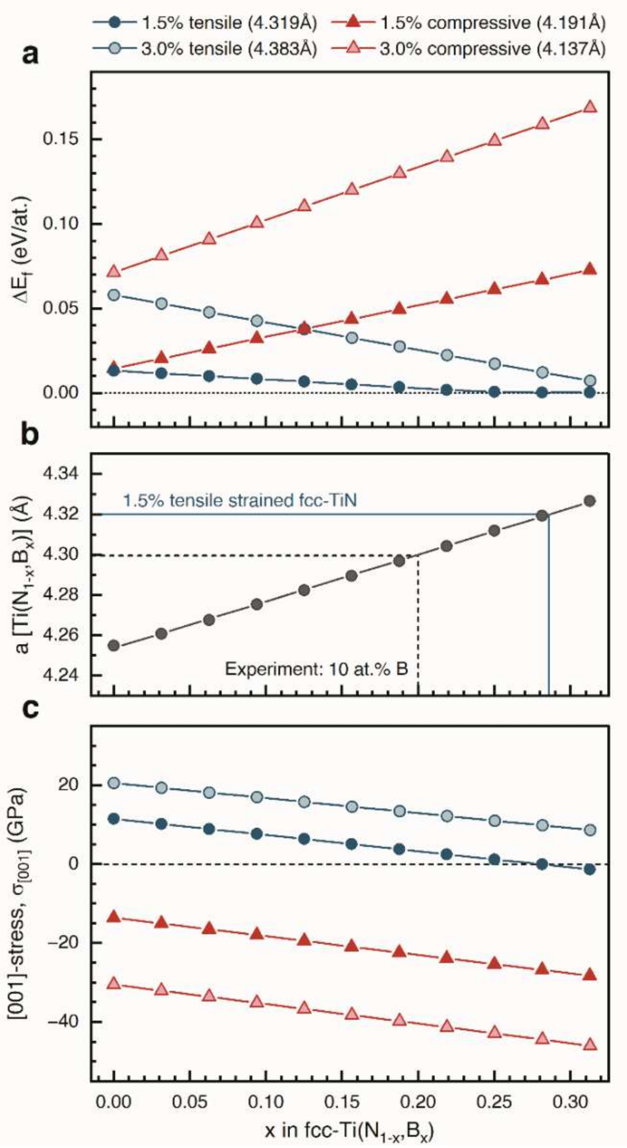

Figure 6.1. The impact of volumetric tensile/compressive strain on the energetic stability and stress state of fcc-Ti(N,B) solid solutions as a function of the B content. (a) Formation energy differences, ΔE_f, between volumetrically strained and fully relaxed systems. Taking the parameter of fcc-TiN (a=4.255 Å) as a reference, tensile strain (blue circular data points)/compressive strain (red triangular data points) is applied by enlarging/shortening the lattice parameter (by 1.5% and 3%). (b) Lattice parameter of a fully relaxed fcc-Ti($N_{1-x}B_x$) plotted against the B content. The B content for which the lattice parameter overlaps with that of the 1.5% strained system is highlighted by a blue line. The black line denotes the resulting lattice parameter corresponding to the 10 at.% B in our experiment. Likewise, if the solubility of B is reduced purely to its size, a necessary minimum size of the fcc-TiN unit cell modified by microalloying can be determined for certain B alloy contents. (c) Strain-induced stress along the [001] crystallographic direction, i.e., along the applied (tensile/compressive) strain, evaluated for the supercells in (a).

Though having a fixed volume, all strained fcc-Ti(N,B) solid solutions are relaxed in terms of ionic positions (for details see the Methodology). Starting from fcc-TiN, all its strained variants are energetically more costly, as indicated by positive formation energy differences, ΔE_f, from the fully relaxed fcc-TiN. For either tensile or compressive strain, the larger the deviation from the equilibrium lattice parameter, the higher the energetic costs (see the ΔE_f of the 3% strained TiN being above that of the 1.5% strained TiN), as we are further away from the thermodynamic equilibrium. Adding B to the N sublattice, ΔE_f gradually increases for all fcc-Ti(N,B) solid solutions under compression. This is because the lattice parameter of fcc-Ti(N,B)—with no strain applied—increases with rising B content, i.e., increasingly deviates from that of the compressed system (see Fig. 6.2b). Contrarily, the lattice parameter of fcc-Ti(N,B) under tension steadily approaches that of the fully relaxed system—mirrored by decreasing ΔE_f—until reaching the equilibrium value. In case of 1.5% tensile strain, the overlap occurs at ~28.5 at.% of B where $\Delta E_f \sim 0$eV/at. (the corresponding lattice parameter is marked in Fig. 6.2b). Note that in order to match the lattice parameter of fcc-TiB (a=4.534 Å), the lattice parameter of fcc-TiN would have to be 6.6% larger (corresponding to a 6.6% volumetric tension).

Trends in the formation energy differences between volumetrically strained and fully relaxed fcc-Ti(N,B) solid solutions (Fig. 6.2a) are further underpinned by evolution of the corresponding stress states. Specifically, Fig. 6.2c shows the stress tensor component along the strained direction, [001], which is (nearly) equal to the stress tensor components along [010] and [001] (differences come from the numeric). Although at higher B contents, these volumetrically-strained systems exhibit also non-zero shear stresses (0–1.3GPa), we analyze only (the dominant) tensile or compressive stresses. Concerning volumetric compression, the [001] stresses increasingly deviate from the fully relaxed (thus, stress-free) fcc-Ti(N,B), consistent with increasing ΔE_f in Fig. 6.2a. Contrarily, stresses on the tensile-strained system diminish with increasing the B content until they nullify. In combination with (approx.) zero E_f difference from the stress-free fcc-Ti(N,B), this mirrors the fact that lattice parameter of the stress-free and tensile-strained system are equal (at this B content). To experimentally address the spatial constraints on B in the fcc-TiN lattice, we conducted our study using a composite target of TiN, TiB_2, and Ti with an elemental composition of 50 at.% Ti, 40% at.% N, and 10% at.% B. By microalloying additional metals Me = Ti, Cr, or Zr (achieved by placing metal pieces on the racetrack of the target), we progressively increased the metal concentration. In order to focus, in particular, on the effects of the metallic microalloying, we have deliberately set the B content to 10 at.% in the specified target composition. Figs. 6.3a-c illustrate the chemical compositions of the deposited coatings (as determined by ToF-ERDA and XRF), displaying a nearly linear progression toward the metal corner within the partial section of the ternary phase diagram. However, the B content of each of the 25 Ti–Me–B–N coatings was maintained at almost 10 at% (which corresponds to ~20 at% on the non-metal sub-lattice if B is solely substituting N). The elemental composition of all deposited coatings is listed in the Supplementary Materials in Table S1. The decrease in B and N with increasing alloying content is because upon adding Ti, Cr, and Zr metals onto the target-race-track also the B and N source (the target itself) is partly covered.

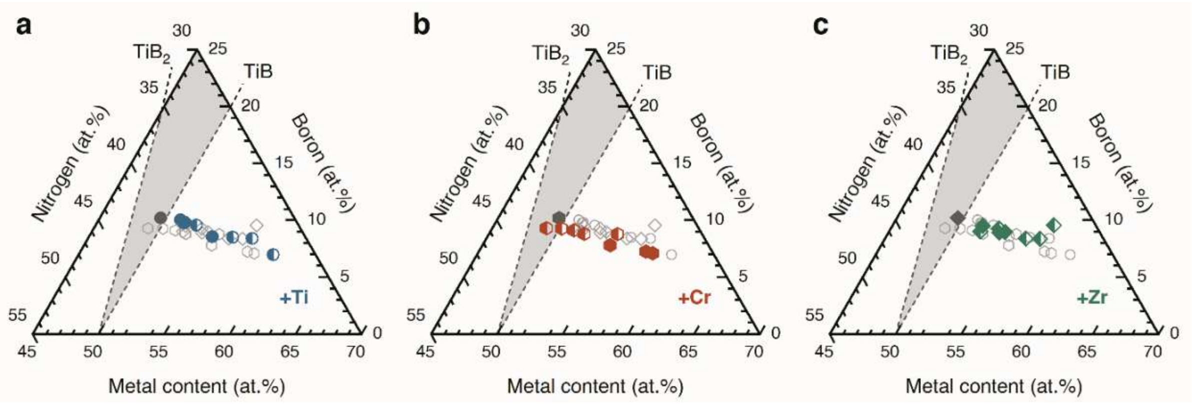

Figure 6.3. (a), (b), and (c) each shows a part of the (quasi)ternary phase diagram for Ti–B–N, Ti–Cr–B–N, and Ti–Zr–B–N including the chemical compositions of the deposited samples [as determined by ToF-ERDA (coatings marked as full-filled symbols) and XRF (indicated with half-filled symbols)]. In each diagram the gray full-filled symbol (determined by ToF-ERDA) represents the $TiB_{0.2}N_{0.8}$ coating obtained from the non-reactively sputtered $TiN+TiB_2+Ti$ composite target. For clarity, the element-specific alloys are each shown in a single diagram and distinguished by color and shape: The addition of Ti is indicated by round symbols in blue, Cr by hexagonal symbols in red, and Zr by diamond-shaped symbols in green. Grey-framed symbols (within the individual panels) indicate the composition of the other alloyed coatings. The gray-shaded triangle with the dashed line boarders indicates the TiN-TiB_2-TiB phase field.

According to our previous DFT calculations[52], B substitutes for N on the non-metal sublattice, while Ti, Cr, and Zr atoms occupy the metal side. Microalloying shifts the chemical composition of the deposited Ti–Me–B–N thin films towards an overstoichiometric metal content (see S1), compensated by vacancies on the non-metal sublattice. This circumstance in itself should already increase the solubility of B, as already shown in the previous study[52]. We deliberately decided to carry out an additional series with the addition of Ti in order to confirm the previous results and also to be able to better describe the effect of alloying with an additional element, i.e. to better separate the two effects (vacancies on the non-metal sublattice and tuned lattice parameter). For clarity, the three series are shown in separate plots (a, b, and c), each color-coded for easy differentiation.

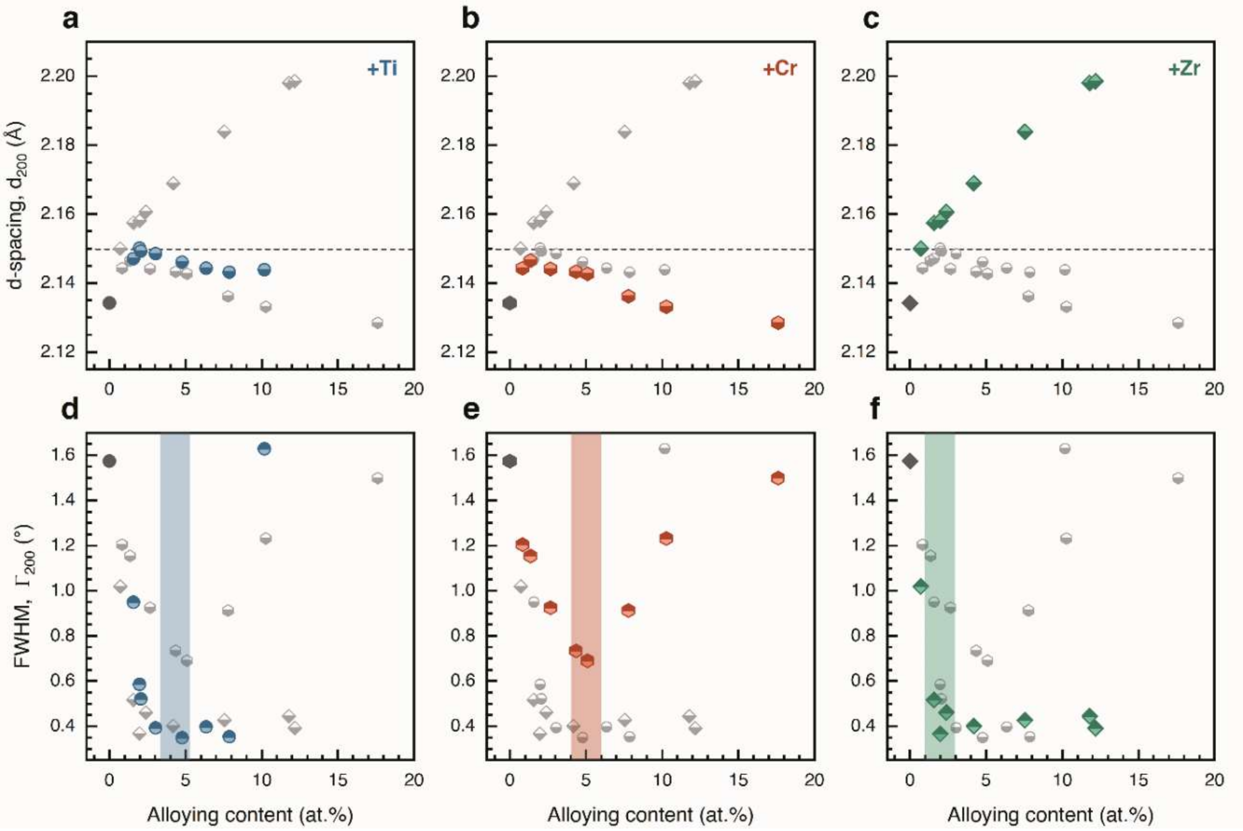

Figure 6.2. (a), (b), and (c) lattice plane distances d_{200} and (d), (e), and (f) full width at half maximum (FWHM, Γ_{200}) of the 200 peaks (at 2θ ~42°). Values were determined by peak profile fitting using a Pearson 7 function and an asymmetry type of peaks by split width and shape. The blue circular symbols represent the Ti–B–N coatings with incremental Ti content. The Cr- and Zr-alloyed Ti–Me–B–N coatings are represented by red hexagons and green diamonds, respectively. The gray full-filled symbol (either round, hexagonal, or diamond-shaped) represent the data point for $TiB_{0.2}N_{0.8}$. Each value for the other two alloying elements is shown as half-shaded gray symbols outlined in their corresponding shape. The dashed horizontal line in (a), (b), and (c) marks the ab initio DFT calculated relaxed d_{200} lattice plane distance for fcc-Ti(N,B) (d_{200}=2.150 Å) with 20 at.% B solved at the non-metal sublattice (see Fig. 6.2b). The alloy concentration range where the minimum FWHM is reached is indicated by the colored range in (d), (e) and (f).

XRD analyses of the Ti–Me–B–N coatings reveal that each alloying series preserves the single-phase cubic face-centered cubic TiN structure consistently, without the emergence of additional crystalline (metallic) phases with increasing metal content (XRD patterns are provided in the Supplementary Materials in Fig. S6.1). Detailed XRD peak profile analysis gives the lattice plane distances and FWHM values of the 200-peak (d_{200} and Γ_{200}) as a function of the respective alloy content. The importance of these two parameters for the validation of a solid solution has already been proved in our previous study using HRTEM investigations[52] and is now applied here in a similar fashion.

Starting with Fig. 6.4a (Ti addition), the lattice spacing increases from d_{200}=2.134 Å (0 at.%) with rising alloying content, reaching its maximum value (d_{200}=2.150 Å) by adding 2.0 at.% Ti. A further addition of Ti causes d_{200} to slightly decrease again (presumably due to vacancies on the non-metal sublattice and the slightly decreasing B-content in the coatings, see Figs. 6.3a-c as well as supplementary table S1, caused by the experimental setup). Simultaneously, as d_{200} increases, Γ_{200} (Fig. 6.4d) decreases concurrently until reaching a minimum at ~5 at.% Ti (corresponding to an amount of ~54.5 at.% Ti in the coating). A more pronounced decline in d_{200}, after an initial increase, is obtained by adding Cr (see Fig. 6.4b).

The maximum lattice spacing attained, reaching 2.146 Å at 1.4 at.% Cr, is below the calculated d_{200} value for fcc-Ti(N,B) with 10 at.% B in the lattice (illustrated by the dashed horizontal line). Although Cr alloying results in a minimum FWHM of the 200-peak of Γ_{200} = 0.69° at 5.1 at.% Cr, this is clearly above the minimum value of 0.35° obtained when adding Ti instead of Cr. Additionally, also the alloying range where Γ_{200} is minimal is much narrower when adding Cr. Γ_{200} rapidly increases when adding more than 5.1 at.% Cr, whereas for Ti addition an increase in Γ_{200} is only observed above 10 at.% Ti. Adding Zr results in a significant increase in d_{200} and a comparatively steep decrease in Γ_{200} (Figs. 6.4c, f), reaching a minimum Γ_{200} by adding at least 1.8 at.% Zr. More Zr leads to a flattening of the increase in d_{200}, reaching 2.198 Å at 12.2 at.% Zr. Already with the addition of 0.7 at.% Zr the d_{200} value is 2.150 Å, thus meeting the value for a fcc-Ti(N,B) with 10 at.% B, as indicated by the intersection with the dashed horizontal line. Notably, even at alloy concentrations above 10 at.%, Γ_{200} remains small with values consistently around 0.40°.

6.5 Discussion

The (initial) increase in d_{200} upon alloying the $TiB_{0.2}N_{0.8}$ coating with Ti and Cr (Figs. 6.4a and b) indicates that more of the available B is soluted within the fcc-TiN lattice, because the concomitant decreasing non-metal/metal ratio as well as substitution of Ti with Cr would suggest for a decreased d_{200}, which is the case for a higher alloying content. The lattice parameter of fcc-CrN (4.15 Å)[82] is much smaller as that of fcc-TiN. When alloying $TiN_{0.8}B_{0.2}$ with Zr, the lattice spacing continuously increases (Fig. 6.4c), because the substitution of Ti with Zr would also cause the lattice parameter to increase (a_{ZrN} = 4.59 Å[82]) and not just the promoted incorporation of B to the fcc-lattice. Consequently, for the Zr alloying case, we have two contributions for an increased lattice parameter

(1: Zr substituting Ti and 2: additional B substitution of N) and one for a reduced lattice parameter (the decreasing non-metal/metal ratio like for the other two cases). A reduction of the non-metal/metal ratio (upon the addition of Ti, Cr, or Zr to $TiN_{0.8}B_{0.2}$) below 1 promotes the formation of vacancies at the non-metal sublattice, which also facilitates the incorporation of additional B at the non-metal sub-lattice—in agreement with our previous results[52]. Thus, for the Zr alloying case, the separation of the two effects (1: Zr substituting Ti and 2: increasing vacancy content at the non-metal sublattice) promoting the B solubility is difficult when solely investigating d_{200}. As the N-content nearly linearly decreases with increasing Zr content, the non-metal-vacancy-induced reduction in d_{200}[83–85] as well as the Zr-for-Ti substitution-induced increase (according to Vegard's rule[86]) in d_{200} is suggested to be nearly linear as well. Thus, the positive deviation of d_{200} from such a linear slope is contributed by the additional incorporation of the provided B into the fcc-lattice than Ti addition.

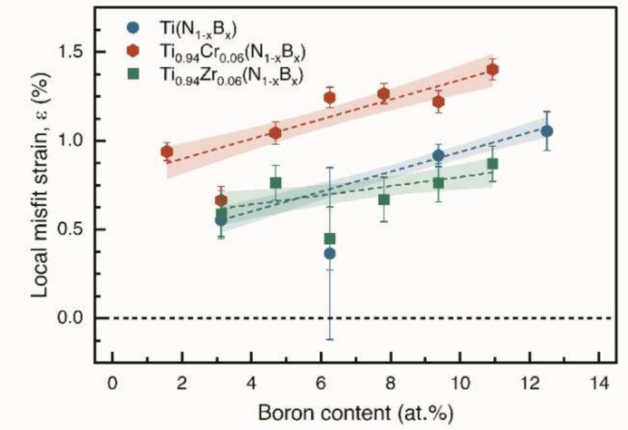

Figure 6.3. DFT calculated local misfit strain ($\varepsilon = d_{Ti\text{-}B} - d_{Ti\text{-}N}) / d_{Ti\text{-}N}$) as a function of the B content for three fcc-TiN structural variants: 1) fcc-$TiN_{1-x}B_x$ (round blue-filled symbols), 2) fcc-$Ti_{0.94}Cr_{0.06}N_{1-x}B_x$ where 6 at.% Cr substitute for Ti on the metal sublattice (hexagonal red-filled symbols), and 3) fcc-$Ti_{0.94}Zr_{0.06}N_{1-x}B_x$ where 6 at.% Zr substitute for Ti on the metal sublattice (squared green symbols). Each calculated data point series is linearly fit and displayed with a color-coded 68% confidence band.

Our alloying strategy has shown that—alongside with the vacancy formation on the non-metal sublattice—the alloying element's size affects the B solubility in the fcc-TiN lattice, presumably by altering the spatial conditions for B on the non-metal sublattice. To support this reasoning, we again employ ab initio calculations to evaluate the radial distribution function (RDF) of Ti–N ($d_{Ti\text{-}N}$) and Ti–B ($d_{Ti\text{-}B}$) bonds (the nearest neighbor distance, corresponding to a local d_{200}), in the fcc-$TiN_{1-x}B_x$ or fcc-$Ti_{0.94}Me_{0.06}N_{1-x}B_x$ lattice. Noteworthily, there is no strain applied and all structures are fully relaxed in terms of volume, shape, and ionic positions (see Methodology). The RDF analysis allows quantifying the local misfit strains[70] in case of Me = Cr or Zr substitute for Ti at the metal sublattice. Based on our experimental results showing improved B solubility when 2–12 at.% Zr, 3–10 at.%Ti, and ~5 at.% Cr is alloyed to $TiB_{0.2}N_{0.8}$, we did calculations of fcc-$Ti_{1-y}Me_yN_{1-x}B_x$ supercells with y=0.06 (which is equivalent to the addition of 3 at.% to the fcc-TiN lattice). By maintaining a 1:1 non-metal-to-metal ratio, our calculations focus exclusively on the size effect of the alloying element on the local misfit strain in the lattice, deliberately excluding the influence of non-metal-vacancies (which we studied previously in detail[52]). Fig. 6.5 shows that the local misfit strain, ε, almost linearly increases with increasing B content in case of fcc-$TiN_{1-x}B_x$, fcc-$Ti_{0.94}Cr_{0.06}N_{1-x}B_x$, and fcc-$Ti_{0.94}Zr_{0.06}N_{1-x}B_x$ structures. While ε is initially lower for the fcc-$TiN_{1-x}B_x$ solid solution, the fcc-$Ti_{0.94}Zr_{0.06}N_{1-x}B_x$ structure becomes more favorable with >5.3 at.% solute B. For incorporating increasing amounts of B in fcc-$Ti_{0.94}Cr_{0.06}N_{1-x}B_x$, ε ranges between 0.94–1.40%, thus significantly higher than in case of fcc-$TiN_{1-x}B_x$ and fcc-$Ti_{0.94}Zr_{0.06}N_{1-x}B_x$. Notably, even for solving 1.6 at.% B in fcc-$Ti_{0.94}Cr_{0.06}N_{1-x}B_x$ (ε=0.94%), ε is 15% (relatively) higher than for the case of a fcc-$Ti_{0.94}Zr_{0.06}N_{1-x}B_x$ solid solution with 11.0 at.% B (ε=0.82%). Comparing the local misfit strains resulting from B addition in fcc-$Ti_{0.94}Zr_{0.06}N_{1-x}B_x$ and fcc-$Ti_{0.94}Cr_{0.06}N_{1-x}B_x$ to the basic fcc-$TiN_{1-x}B_x$ lattice, it is evident that the Zr-substituted structure becomes most favorable with increasing B content. Although the introduction of B induces local misfit strains in all three cases (as indicated by an increase in ε with increasing B content), the replacement of 6 at.% Ti with larger Zr in the metal sublattice results in a less steep increase in ε than in the case of fcc-$TiN_{1-x}B_x$ and fcc-$Ti_{0.94}Cr_{0.06}N_{1-x}B_x$. In the case of fcc-$Ti_{0.94}Cr_{0.06}N_{1-x}B_x$, substituting 6 at.% Ti with smaller Cr atoms in the metal sublattice already introduces local lattice strains that provide even less favorable spatial conditions for B-incorporation than fcc-$TiN_{1-x}B_x$. Simplifying the situation by representing atoms as rigid spheres, we aim to illustrate how the size of alloying elements affects spatial conditions for B within the fcc-TiN lattice while also considering the effect of N-vacancies. A detailed summary concerning the data from the RDF analysis utilized for this illustration is given in the Supplementary Materials listed in Tables S6.2–S6.4.

Fig. 6.6a shows the fcc-$TiN_{0.70}B_{0.20}$ lattice having 10 at.% vacancies at the non-metal sublattice. Building on our prior findings, we considered a simple model with one N vacancy added for each B atom (not necessarily in the vicinity of this B). In the fcc-TiN lattice, N occupies the octahedral interstitial site built by six Ti atoms, which themselves construct an fcc-cell.

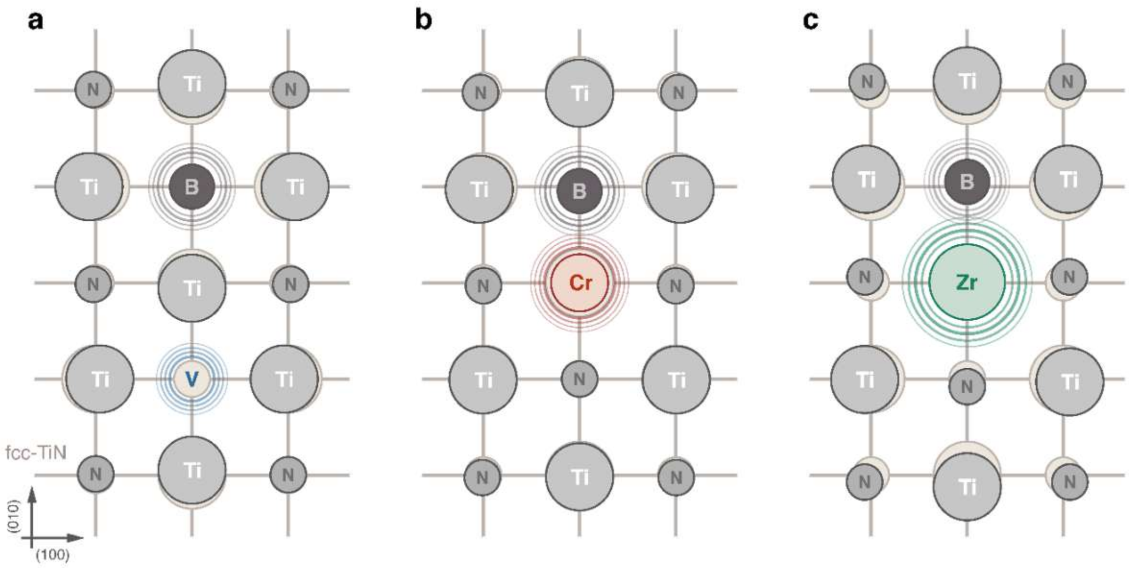

Figure 6.6. Two-dimensional graphical representation of the (100) plane of (a) the fcc-$TiN_{0.70}B_{0.20}$ lattice with 10 at.% vacancies at the non-metal sublattice, (b) the fcc-$Ti_{0.94}Cr_{0.06}N_{0.80}B_{0.20}$ lattice, and (c), the fcc-$Ti_{0.94}Zr_{0.06}N_{0.80}B_{0.20}$ lattice. The N vacancy as well as Cr and Zr are placed as the nearest neighbor to B. The underlying lattice construction represents the initial fcc-TiN lattice with 0 at.% B. The ratio between atomic radii[59] and bond length—based on our RDFs as listed in the Supplementary Materials in Tables S6.2–S6.4—are slightly exaggerated for clarity.

Only four of these Ti atoms are visible from the (100) plane, since the other two sit vertically, one plane above and below the N atom. Based on our calculations, the absence of an N atom induces local contractions at the metal sublattice (as seen in shorter Ti–Ti bonds listed in Table S6.2). In particular, the neighboring Ti atoms experience tensile strain to compensate for the missing N atom, resulting in local misfit strains. These local tensile strains caused by the non-metal vacancy, compensate—to some extent—for the compressive strain induced by the larger B atom at the non-metal sublattice. Although B substitutes for N on the non-metal sublattice, our RDF calculations do not result in significant changes in the Ti–N bond lengths (Table S6.2). Rather, we observe shorter (near N-vacancies) and larger (near B-atoms) Ti–Ti bonds for the introduction of B into the fcc-TiN lattice. Although non-metal vacancies compensate for some of the compressive strains induced by B, the fcc-TiN lattice expands by ~1% when forming an fcc-$TiN_{0.60}B_{0.20}$ solid solution[52]. Fig. 6.6b illustrates the case of fcc-$Ti_{0.94}Cr_{0.06}N_{0.80}B_{0.20}$ solid solution, where Cr and B atoms are nearest neighbors in the lattice. The substitution with smaller Cr atoms causes adjacent Ti atoms to move slightly closer together, thereby reducing the size of the octahedral sites (or the space at the non-metal sublattice); please compare Tables S6.2 and S6.3. Consequently, the B atoms have even less space as for fcc-$TiN_{0.80}B_{0.20}$, consistent with our previously discussed results of Fig. 6.2b. As derived from DFT, the lattice parameter of fcc-$Ti_{0.94}Cr_{0.06}N_{0.80}B_{0.20}$ (where 6 at.% Cr replace Ti),

a=4.291 Å (calculated), is smaller than that of fcc-$TiN_{0.80}B_{0.20}$, a=4.304 Å (calculated). Compared to that, the calculated lattice parameter of fcc-$Ti_{0.94}Zr_{0.06}N_{0.80}B_{0.20}$ is even a=4.329Å. However, these parameters need to be rationalized with those of the B-free lattices, TiN (4.255 Å), $Ti_{0.94}Cr_{0.06}N$ (4.247 Å), and $Ti_{0.94}Zr_{0.06}N$ (4.267 Å). The data analysis suggests, as shown in Fig. 6.6c, that the size of the Zr atom stretches the surrounding Ti–Ti and Ti–N bonds so much that the additional B incorporation only slightly affects the lattice (see Table S6.3). Expanding the fcc-TiN lattice by substituting a larger Zr atom for Ti on the metal sublattice (and ZrN easily forms a solid solution with TiN) partly compensates for the local strains induced by the B atom taking the place of N at the non-metal sublattice. Conversely, replacing Ti atoms with smaller Cr atoms (also, CrN easily forms a solid solution with TiN) further restricts the spatial conditions for replacing N with a larger B atom at the non-metal sublattice. These data indicate (in combination with our previous findings on the effects of non-metal-sublattice vacancies on the B solubility) that a shared loading of the sublattices benefits the overall situation. Replacing N on the non-metal sublattice with B induces compressive strains on it. These are partly compensated by the two effects leaving the non-metal sublattice with tensile strains: 1) vacancies on the non-metal sublattice and 2) larger substitutional atoms on the metal sublattice (like Zr vs. Ti). On the contrary, replacing Ti with the smaller Cr induces compressive strains on the non-metal sublattice, which are even further increased upon the substitution of N with B.

6.6 Summary and Conclusion

This study addresses synthesis challenges in obtaining single-phase materials of immiscible phases by overcoming spatial constraints, using Ti–B–N as model material system. First, ab initio density functional theory (DFT) calculations are employed to demonstrate the metastable nature of fcc-$TiN_{1-x}B_x$ solid solution. By illustrating its energetic landscape in a quasi-binary convex hull phase diagram, we highlight the thermodynamic barrier that inhibits B incorporation into the fcc-TiN lattice. Our ab initio predictions further reveal the critical role of lattice strain in modulating the stability of fcc-Ti(N,B) solid solution. The models of fcc-Ti(N,B) solid solution with a tensile-strained or compressively-strained lattice parameter, indicate that the former can promote the incorporation of B to the non-metal sublattice. Specifically, a 1.5% tensile strain facilitates an incorporation of up to ~28.5 at.% B. The proposed experimental microalloying approach meets with our theoretical predictions regarding the spatial constraints on B incorporation within the fcc-TiN lattice. We progressively increased the metal concentration while maintaining the B content close to 10 at% in the 25 Ti–Me–B–N coatings by adding additional Me=Ti, Cr, or Zr pieces (0-

15 at%) to a Ti–B–N composite target (consisting of 50 at% Ti, 40 at% N, and 10 at% B). Although the formation of vacancies at the non-metal sublattice facilitates the substitution of N with B within the fcc-TiN lattice, the size of the metal alloying elements further defines the spatial conditions affecting the B incorporation. This observation is supported by experimental data showing that the lattice parameter increases more by alloying with Zr compared to Ti and Cr. As can be seen from the FWHM, alloying with Zr has the greatest effect on the solubility of B (the addition of only 2 at.% Zr is sufficient to fully incorporate the ~10 at.% B provided), while Cr is even less helpful than the addition of Ti. The observed slightly increased solubility of B in fcc-TiN by alloying with Cr is thus exclusively due to the resulting increased proportion of vacancies on the non-metal sublattice. This effect (due to the additional vacancies) is even lower than in the fcc-Ti(B,N) coatings alloyed with additional Ti. Notably, by alloying Ti it was possible to isolate the effect of vacancies on B solubility in the non-metal sublattice. The reduced solubility can be explained by the fact that the substitution of Ti by the smaller Cr induces additional contracting strains on the non-metal sublattice, by which the substitution of N with the larger B becomes more difficult. Through a detailed RDF analysis we compared the local misfit strains induced by increasing the B concentration for 16 fcc-$Ti_{0.94}Me_{0.06}N_{1-x}B_x$ structures; where Me is either Ti, Cr, or Zr. We show that the size of a larger alloying element directly affects the spatial conditions for B within the lattice, providing more space—not only through the introduction of N-vacancies—but also through an enlarged metal sublattice. In particular, when larger atoms can substitute for Ti on the metal sublattice the formation of the fcc-Ti(N,B) solid solution is favored by reducing the local misfit strain.

In summary, we introduced a novel microalloying concept aimed at manipulating the metallic sublattice to influence the solubility of B in the non-metal sublattice. By systematically introducing smaller or larger atoms into the metal lattice, we addressed the size-dependent effects of alloying atoms in forming an fcc-Ti(N,B) solid solution. The here-presented results hold promise for advancing the synthesis and design of novel materials with tailored properties and functionalities, not only within the Ti–B–N system, but also potentially in other metastable material systems.

6.7 References

1 H. Holleck, *J Vac Sci Technol A*, 1986, **4**, 2661–2669.

2 L. Hultman, *Vacuum*, 2000, **57**, 1–30.

3 P. H. Mayrhofer, C. Mitterer, L. Hultman and H. Clemens, *Prog Mater Sci*, 2006, **51**, 1032–1114.

4 D. Holec, L. Zhou, H. Riedl, C. M. Koller, P. H. Mayrhofer, M. Friák, M. Šob, F. Körmann, J. Neugebauer, D. Music, M. A. Hartmann and F. D. Fischer, *Adv Eng Mater*, 2017, **19**, 1600688.

5 F. Therrien, E. B. Jones and V. Stevanović, *Appl Phys Rev*, 2021, **8**, 031310.

6 R. Kieffer and F. Benesovsky, *Hartstoffe*, Springer Wien, Wien, 1963.

7 H. J. Goldschmidt, *Interstitial Alloys*, Springer New York, New York, 1967.

8 O. Knotek, M. Böhmer and T. Leyendecker, *J Vac Sci Technol A*, 1986, **4**, 2695–2700.

9 A. Höling, L. Hultman, M. Odén, J. Sjölén and L. Karlsson, *Surf Coat Technol*, 2005, **191**, 384–392.

10 E. Santecchia, A. M. S. Hamouda, F. Musharavati, E. Zalnezhad, M. Cabibbo and S. Spigarelli, *Ceram Int*, 2015, **41**, 10349–10379.

11 A. E. van Arkel and J. H. de Boer, *Z anorg allg Chem*, 1925, **148**, 345–350.

12 D. R. Glasson and S. A. A. Jayaweera, *J Appl Chem*, 1968, **18**, 65–77.

13 I. Petrov, L. Hultman, U. Helmersson, J.-E. Sundgren and J. E. Greene, *Thin Solid Films*, 1989, **169**, 299–314.

14 G. Hâkansson, L. Hultman, J.-E. Sundgren, J. E. Greene and W.-D. Munz, *Surf Coat Tech,* 1991, **48**, 51–67.

15 L. Hultman, C. Engström, J. Birch, M. P. Johansson, M. Oden, L. Karlsson and H. Ljungcrantz, *Int J Mater Res*, 1999, **90**, 803–813.

16 P. H. Mayrhofer, F. Kunc, J. Musil and C. Mitterer, *Thin Solid Films*, 2002, **41**, 151–159.

17 P. H. Mayrhofer, M. Geier, C. Löcker and L. Chen, *Int J Mater Res*, 2009, **100**, 1052–1058.

18 G. Hägg, *Z Phys Chem B*, 1929, **6B**, 221–232.

19 G. Hägg, *Z Phys Chem B*, 1931, **12**, 33–56.

20 P. Blaha, J. Redinger and K. Schwarz, *Phys Rev B*, 1985, **31**, 2316–2325.

21 K. Wasa and S. Hayakawa, *Thin Solid Films*, 1971, **10**, 367–375.

22 O. Knotek, W. Bosch, and T. Leyendecker, *Verschleißmindernde Schichten im System Ti-Al-C-N-O durch Kathodenzerstäubung*, Proceedings of the 11th International Plansee Seminar, Reutte, 1985.

23 T. Takahashi, K. Sugiyama and K. Tomita, *J Electrochem Soc*, 1967, **114**, 1230–1235.

24 P. H. Mayrhofer, D. Music and J. M. Schneider, *J Appl Phys*, 2006, **100**, 094906.

25 D. Holec, R. Rachbauer, L. Chen, L. Wang, D. Luef and P. H. Mayrhofer, *Surf Coat Technol*, 2011, **206**, 1698–1704.

26 H. Leiste, M. Stüber, V. Schier and H. Holleck, *Materials Science Forum*, 1999, **308–311**, 467–475.

27 S.-H. Jhi, J. Ihm, S. G. Louie and M. L. Cohen, *Nature,* 1999*,* **399**, 132–134.

28 S. Vepřek, S. Reiprich and L. Shizhi, *Appl Phys Lett*, 1995, **66**, 2640–2642.

29 E. O. Hall, *Proc Phys Soc B,* 1951, **64**, 747–747.

30 N. J. Petch, *Acta Metall*, 1986, **34**, 1387–1393.

31 S. Vepřek and S. Reiprich, *Thin Solid Films*, 1995, **268**, 64–71.

32 A. L. Greenaway, C. L. Melamed, M. Brooks Tellekamp, R. Woods-Robinson, E. S. Toberer, J. R. Neilson and A. C. Tamboli, *Annu Rev Mater Res*, 2021, **51**, 13.1–13.28.

33 S. Yu, Q. Zeng, A. R. Oganov, G. Frapper and L. Zhang, *Phys Chem Chem Phys*, 2015, **17**, 11763–11769.

34 W. Sun, S. T. Dacek, S. P. Ong, G. Hautier, A. Jain, W. D. Richards, A. C. Gamst, K. A. Persson and G. Ceder, *Sci Adv*, 2016, DOI: 10.1126/sciadv.1600225.

35 C. J. Bartel, *J Mater Sci*, 2022, **57**, 10475–10498.

36 W. Sun, C. J. Bartel, E. Arca, S. R. Bauers, B. Matthews, B. Orvañanos, B. R. Chen, M. F. Toney, L. T. Schelhas, W. Tumas, J. Tate, A. Zakutayev, S. Lany, A. M. Holder and G. Ceder, *Nat Mater*, 2019, **18**, 732–739.

37 M. Aykol, S. S. Dwaraknath, W. Sun and K. A. Persson, *Sci Adv*, 2018, DOI: 10.1126/sciadv.aaq0148

38 C. M. Caskey, R. M. Richards, D. S. Ginley and A. Zakutayev, *Mater Horiz*, 2014, **1**, 424–430.

39 S. Siol, *Phys Status Solidi A*, 2019, **216**, 1800858.

40 W. Sun, A. Holder, B. Orvañanos, E. Arca, A. Zakutayev, S. Lany and G. Ceder, *Chemistry of Materials*, 2017, **29**, 6936–6946.

41 M. Bianchini, J. Wang, R. J. Clément, B. Ouyang, P. Xiao, D. Kitchaev, T. Shi, Y. Zhang, Y. Wang, H. Kim, M. Zhang, J. Bai, F. Wang, W. Sun and G. Ceder, *Nat Mater*, 2020, **19**, 1088–1095.

42 O. Knotek, W. D. Münz and T. Leyendecker, *J Vac Sci Technol A*, 1987, **5**, 2173–2179.

43 J. Musil, S. Kadlec and W.-D. Münz *J Vac Sci Technol A*, 1991, **9**, 1171–1177.

44 J. Paulitsch, M. Schenkel, T. Zufraß, P. H. Mayrhofer and W.-D. Münz, *Thin Solid Films*, 2010, **518**, 5558–5564.

45 A. Anders, *Thin Solid Films*, 2010, **518**, 4087–4090.

46 A. Anders, *J Appl Phys,* 2017*,* **121**, 171101.

47 D. Depla and W. P. Leroy, *Thin Solid Films*, 2012, **520**, 6337–6354.

48 S. Mahieu and D. Depla, *J Phys D Appl Phys*, 2009, **42**, 053002.

49 D. Depla, S. Mahieu and J. E. Greene, in *Handbook of Deposition Technologies for Films and Coatings: Science, Applications and Technology*, ed. P. M. Martin, Elsevier Science, Norwich, New York, Oxford, 3rd ed, 2009, ch. 5, pp. 253–296.

50 R. Prange, R. Cremer and D. Neuschütz, *Surf Coat Technol*, 2000, **133–134**, 208–214.

51 W. Gissler, *Surf Coat Technol*, 1994, **68–69**, 556–563.

52 R. Janknecht, R. Hahn, N. Koutná, T. Wójcik, E. Ntemou, A. Steiger-Thirsfeld, Z. Chen, A. Kirnbauer, P. Polcik, S. Kolozsvári, Z. Zhang, D. Primetzhofer and P. H. Mayrhofer, *Acta Mater*, 2024, **271**, 119858.

53 R. F. Zhang, S. H. Sheng and S. Veprek, *Acta Mater*, 2008, **56**, 4440–4449.

54 H. D. Männling, D. S. Patil, K. Moto, M. Jilek and S. Veprek, *Surf Coat Technol*, 2001, **146–147**, 263–267.

55 P. H. Mayrhofer, C. Mitterer, J. G. Wen, I. Petrov and J. E. Greene, *J Appl Phys*, 2006, **100**, 044301.

56 C. Mitterer, P. H. Mayrhofer, M. Beschliesser, P. Losbichler, P. Warbichler, F. Hofer, P. N. Gibson, W. Gissler, H. Hruby, J. Musil and J. Vlček, *Surf Coat Technol*, 1999, **120–121**, 405-411.

57 J. Neidhardt, M. O'Sullivan, A. E. Reiter, W. Rechberger, W. Grogger and C. Mitterer, *Surf Coat Technol*, 2006, **201**, 2553–2559.

58 R. Hahn, A. Tymoszuk, T. Wojcik, A. Kirnbauer, T. Kozák, J. Čapek, M. Sauer, A. Foelske, O. Hunold, P. Polcik, P. H. Mayrhofer and H. Riedl, *Surf Coat Technol*, 2021, **420**, 127327.

59 B. Cordero, V. Gómez, A. E. Platero-Prats, M. Revés, J. Echeverría, E. Cremades, F. Barragán and S. Alvarez, *Dalton Trans*, 2008, **21**, 2832–2838.

60 P. Ström and D. Primetzhofer, *J Instrum*, 2022, DOI:10.1088/1748-0221/17/04/P04011.

61 M. Janson, CONTES conversion of time-energy spectra—A program for ERDA data analysis, Internal Report, Uppsala University, UPP, 2004.

62 T. Degen, M. Sadki, E. Bron, U. König and G. Nénert, in *Powder Diffraction*, Cambridge University Press, Cambridge, 2014, vol. 29, suppl. S2, pp. S13–S18.

63 S. Gates-Rector and T. Blanton, *Powder Diffr*, 2019, **34**, 352–360.

64 G. Kresse and J. Furthmüller, *Phys Rev B*, 1996, **54**, 11169–11186.

65 G. Kresse and D. Joubert, *Phys Rev B*, 1999, **59**, 1758–1775.

66 W. Kohn and L. J. Sham, *Phys Rev,* 1965, **140**, A1133–A1138.

67 J. P. Perdew, K. Burke and M. Ernzerhof, *Phys Rev Lett*, 1996, **77**, 3865–3868.

68 D. Nöger, A command line tool written in Python/Cython for finding optimized SQS structures, GitHub, 2019.

69 A. Stukowski, *Model Simul Mat Sci Eng*, 2010, DOI: 10.1088/0965-0393/18/1/015012.

70 T. Uesugi and K. Higashi, *Comput Mater Sci*, 2013, **67**, 1–10.

71 L. H. Andersson and R. Kiessling, *Acta chem scand*, 1950, **4**, 160-164.

72 D. Holec and P. H. Mayrhofer, *Scr Mater*, 2012, **67**, 760–762.

73 M. Fallmann, Z. Chen, Z. L. Zhang, P. H. Mayrhofer and M. Bartosik, *Surf Coat Technol*, 2019, **375**, 1–7.

74 Z. K. Liu, *Acta Mater*, 2020, **200**, 745–792.

75 R. V. Chepulskii and S. Curtarolo, *Acta Mater*, 2009, **57**, 5314–5323.

76 L. Pauling, *J Am Chem Soc*, 1929, **51**, 1010–1026.

77 L. Pauling, *J Am Chem Soc*, 1931, **53**, 3225–3237.

78 J. George, D. Waroquiers, D. Di Stefano, G. Petretto, G. Rignanese and G. Hautier, *Angew Chem*, 2020, **132**, 7639–7645.

79 U. Mizutani, H. Sato, T.B. Massalski, *Prog Mater Sci*, 2021, **120**, 100719.

80 W. Hume-Rothery, *J Inst Metals*, 1926, **35**, 319–335.

81 A. Martin and M. Thuo, *Acc Mater Res*, 2023, **4**, 809–813.

82 A. Jain, S. P. Ong, G. Hautier, W. Chen, W. D. Richards, S. Dacek, S. Cholia, D. Gunter, D. Skinner, G. Ceder and K. A. Persson, *APL Mater*, 2013, **1**, 011002.

83 C. S. Shin, D. Gall, N. Hellgren, J. Patscheider, I. Petrov and J. E. Greene, *J Appl Phys*, 2003, **93**, 6025–6028.

84 D. G. Sangiovanni, B. Alling, P. Steneteg, L. Hultman and I. A. Abrikosov, *Phys Rev B*, 2015, **91**, 054301.

85 Z. Zhang, A. Ghasemi, N. Koutná, Z. Xu, T. Grünstäudl, K. Song, D. Holec, Y. He, P. H. Mayrhofer and M. Bartosik, *Mater Des*, 2021, **207**, 109844.

86 L. Vegard, *Z für Physik*, 1921, **5**, 17–26.

S6 Supplementary Materials

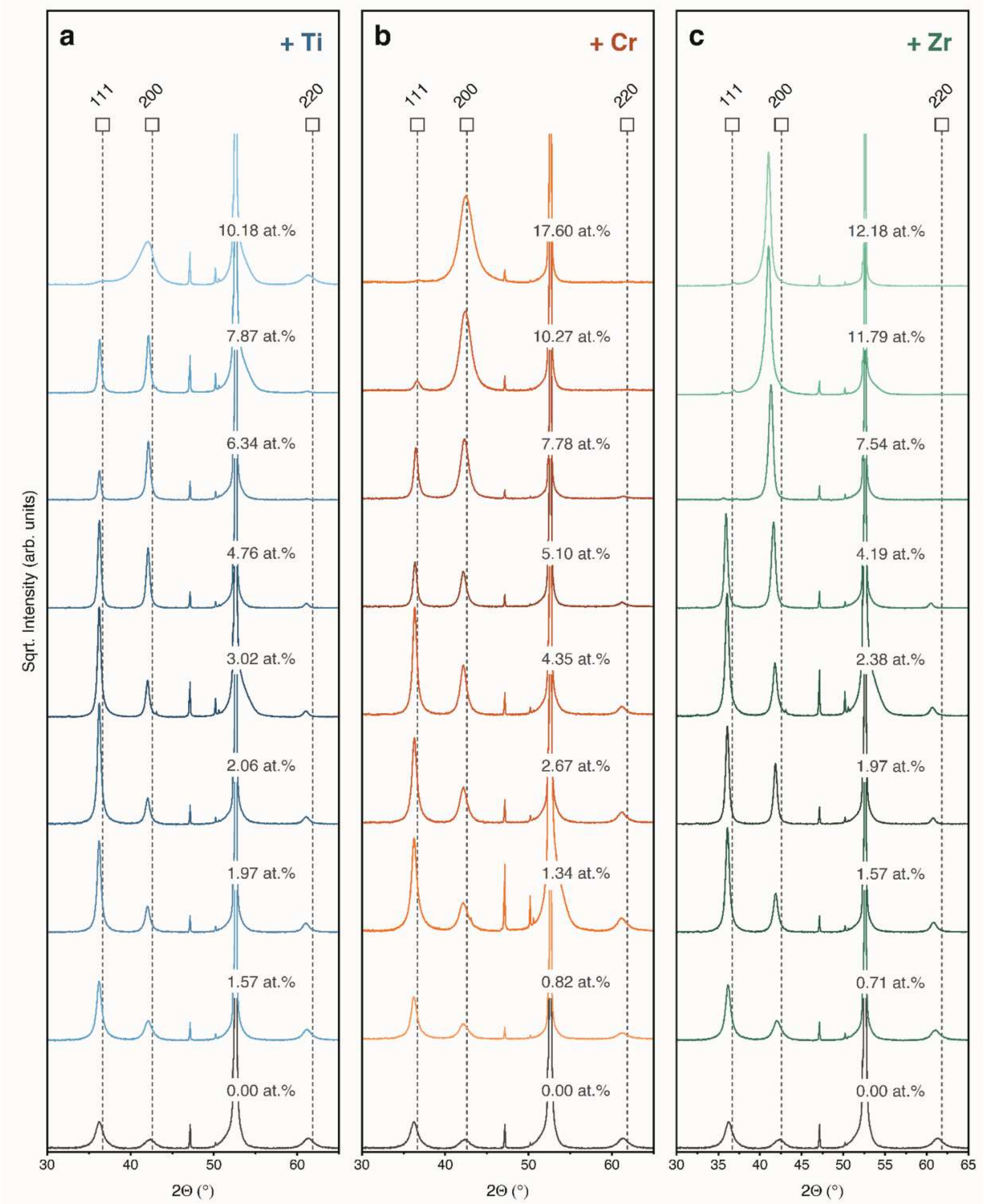

Supplementary Figure S6.1. X-ray diffraction (XRD) patterns of Ti–Me–B–N coatings sputtered from a TiN+TiB_2+Ti compound target with increasing Me=Ti, Cr and Zr alloy contents, shown in blue, red-orange and green, respectively. (a) XRD patterns for Ti–B–N (+Ti), (b) Ti–Cr–B–N, and (c) Ti–Zr–B–N coatings with labeled alloy contents determined by ERDA and XRF. The gray XRD pattern at the bottom of each panel represents the diffraction peaks for the unalloyed $TiB_{0.2}N_{0.8}$ coating. Standard peak positions of fcc-TiN for the (100), (200), and (220) crystal planes (JCPDS No. 00-038-1420)[1] are included for reference, highlighting the peak shift caused by the incorporation of B in the fcc-TiN lattice. A detailed analysis of the (200) diffraction peaks is provided in Fig. 6.4. No other crystalline phases are present. [1] S. Gates-Rector and T. Blanton, *Powder Diffr*, 2019, 34**,** 352–360

Supplementary Table S6.1. Summary of experimental results from chemical and XRD analysis of the deposited coatings in this study including $TiB_{0.2}N_{0.8}$, Ti–B–N, Ti–Cr–B–N and Ti–Zr–B–N, with the latter three each showing increasing alloy (Me=Ti, Cr, or Zr) concentrations. The alloying content of Ti is the difference of the measured Ti content to the reference coating $TiB_{0.20}N_{0.80}$.

Coating	Ti (at.%)	B (at.%)	N (at.%)	+ Me (at.%)	**(B+N)/Me**	d_{200} (Å)	FWHM (°2Θ)		
				Me=Ti, Cr, Zr			left	right	mean
$TiB_{0.2}N_{0.8}$	49.64	10.21	40.15	–	**1.01**	2.134	1.45	1.70	1.58
Ti–B–N	49.64	10.06	38.73	1.57	**0.92**	2.147	0.87	1.03	0.95
		9.78	38.61	1.97	**0.90**	2.150	0.54	0.63	0.59
		9.79	38.51	2.06	**0.90**	2.149	0.49	0.55	0.52
		9.57	37.77	3.02	**0.85**	2.149	0.42	0.36	0.39
		8.55	37.05	4.76	**0.77**	2.146	0.36	0.34	0.35
		8.49	35.53	6.34	**0.71**	2.144	0.38	0.42	0.40
		8.39	34.10	7.87	**0.65**	2.143	0.38	0.33	0.35
		6.96	33.22	10.18	**0.57**	2.144	2.21	1.05	1.63
Ti–Cr–B–N	49.45	9.29	40.44	0.82	**0.99**	2.144	1.07	1.34	1.21
	47.77	9.31	41.58	1.34	**1.04**	2.147	0.93	1.38	1.16
	48.63	9.12	39.58	2.67	**0.95**	2.144	0.88	0.97	0.92
	47.91	8.80	38.94	4.35	**0.91**	2.143	0.72	0.75	0.73
	49.64	7.79	37.47	5.10	**0.83**	2.143	0.68	0.70	0.69
	47.03	8.77	36.42	7.78	**0.82**	2.136	0.90	0.93	0.91
	47.44	7.26	35.03	10.27	**0.73**	2.133	1.14	1.32	1.23
	40.69	7.11	34.60	17.60	**0.72**	2.128	1.43	1.57	1.50
Ti–Zr–B–N	51.23	9.03	39.03	0.71	**0.93**	2.150	0.92	1.12	1.02
	50.31	9.51	38.61	1.57	**0.93**	2.157	0.51	0.53	0.52
	51.85	9.00	37.18	1.97	**0.86**	2.158	0.39	0.34	0.38
	50.84	9.29	37.49	2.38	**0.88**	2.161	0.46	0.47	0.46
	49.23	8.91	37.67	4.19	**0.87**	2.169	0.45	0.36	0.40
	48.16	8.40	35.90	7.54	**0.80**	2.184	0.48	0.38	0.43
	45.46	9.56	33.18	11.80	**0.75**	2.198	0.53	0.36	0.45
	44.63	8.36	34.83	12.18	**0.76**	2.199	0.46	0.33	0.39

Supplementary Table S6.2: Summary of RDF analysis results obtained for fcc-Ti(N$_{1-x}$,B$_x$) and fcc-Ti(N$_{1-2x}$,B$_x$) structures, with increasing B content evaluated for the nearest neighbor Ti–Ti, Ti-B, Ti–N, B–N, and N–N bonds, including the standard error (SE). B–B bonds are not listed because the B content is insufficient for two B atoms being nearest neighbors. Values corresponding to Fig. 6.5 are highlighted in blue. All data are used to illustrate and discuss the effect of microalloying on the fcc-Ti(B,N) lattice in Fig. 6.6.

fcc-Ti(N$_{1-x}$,B$_x$)

Ti	X	B	N	Ti–Ti (Å)		Ti–B (Å)		Ti–N (Å)		B–N (Å)		N–N (Å)	
(at.%)	(at.%)	(at.%)	(at.%)	d	SE	d	SE	d	SE	d	SE	d	SE
50.00	0.00	0.00	50.00	3.005	–	–	–	2.125	–	–	–	3.005	–
		3.13	46.88	3.018	<0.001	2.145	0.001	2.133	0.001	3.030	<0.001	3.016	<0.001
		6.25	43.75	3.044	<0.001	2.147	0.004	2.139	0.001	2.139	0.001	3.027	<0.001
		9.38	40.63	3.048	<0.001	2.162	0.001	2.143	0.001	2.143	0.001	3.036	<0.001
		12.50	37.50	3.067	<0.001	2.173	0.002	2.147	0.002	2.150	0.002	3.046	<0.001

fcc-Ti(N$_{1-2x}$,B$_x$)

Ti	X	B	N	Ti–Ti (Å)		Ti–B (Å)		Ti–N (Å)		B–N (Å)		N–N (Å)	
(at.%)	(at.%)	(at.%)	(at.%)	d	SE	d	SE	d	SE	d	SE	d	SE
50.79	0.00	1.22	36.58	3.009	0.001	2.124	<0.001	2.130	0.001	3.025	0.001	3.015	<0.001
51.61		2.45	34.12	2.994	0.001	2.145	0.001	2.133	0.001	3.038	<0.001	3.016	<0.001
52.46		3.68	31.65	3.013	0.001	2.152	0.001	2.133	0.001	3.043	<0.001	3.022	<0.001
53.33		4.92	29.18	2.979	0.001	2.177	0.001	2.133	0.002	3.040	<0.001	3.027	<0.001
54.24		6.15	26.70	3.012	0.002	2.156	0.001	2.137	0.002	3.054	<0.001	3.032	0.001
55.17		7.39	24.22	2.993	0.002	2.160	0.001	2.126	0.003	3.062	0.001	3.041	<0.001

Supplementary Table S6.3: Summary of RDF analysis results obtained for fcc-Ti$_{0.94}$Cr$_{0.06}$N$_{1-x}$B$_x$ and fcc-Ti$_{0.94}$Zr$_{0.06}$N$_{1-x}$B$_x$ structures, with increasing B content evaluated for the nearest neighbor Ti–Ti, Ti–B, Ti–N, B–N, and N–N bonds, including the standard error (SE). B-B bonds are not listed because the B content is insufficient for two B atoms being nearest neighbors. Values corresponding to Fig. 6.5 are highlighted in red and green. All data are used to illustrate and discuss the effect of microalloying on the fcc-Ti(N,B) lattice in Fig. 6.6.

fcc-Ti$_{0.94}$Cr$_{0.06}$N$_{1-x}$B$_x$

Ti	Cr	B	N	Ti–Ti (Å)		Ti–B (Å)		Ti–N (Å)		B–N (Å)		N–N (Å)	
(at.%)	(at.%)	(at.%)	(at.%)	d	SE	d	SE	d	SE	d	SE	d	SE
46.88	3.13	1.56	48.44	3.005	<0.001	2.143	0.001	2.124	0.001	3.020	0.002	3.004	<0.001
		3.13	46.88	3.011	<0.001	2.140	0.000	2.126	0.001	3.026	0.001	3.008	<0.001
		4.69	45.31	3.015	0.001	2.150	0.001	2.128	0.001	3.031	<0.001	3.011	<0.001
		6.25	43.75	3.020	0.001	2.157	0.001	2.131	0.001	3.033	<0.001	3.013	<0.001
		7.81	42.19	3.025	0.001	2.159	0.001	2.132	0.001	3.036	0.001	3.016	<0.001
		9.38	40.63	3.033	0.001	2.160	0.001	2.134	0.001	3.040	<0.001	3.022	<0.001
		10.94	39.06	3.035	0.001	2.166	0.001	2.136	0.002	3.047	0.001	3.023	<0.001

fcc-Ti$_{0.94}$Zr$_{0.06}$N$_{1-x}$B$_x$

Ti	Zr	B	N	Ti–Ti (Å)		Ti–B (Å)		Ti–N (Å)		B–N (Å)		N–N (Å)	
(at.%)	(at.%)	(at.%)	(at.%)	d	SE	d	SE	d	SE	d	SE	d	SE
46.88	3.13	3.13	46.88	3.050	0.001	2.173	0.001	2.157	0.002	3.067	0.001	3.043	0.001
		4.69	45.31	3.036	<0.001	2.164	0.001	2.148	0.001	3.053	0.001	3.040	0.001
		6.25	43.75	3.038	<0.001	2.162	0.001	2.152	0.001	3.058	0.001	3.042	0.001
		7.81	42.19	3.045	<0.001	2.168	0.001	2.154	0.002	3.063	0.001	3.040	0.001
		9.38	40.63	3.050	0.001	2.173	0.001	2.157	0.002	3.067	0.001	3.043	0.001
		10.94	39.06	3.054	0.001	2.178	0.001	2.159	0.001	3.072	0.001	3.044	0.001

Supplementary Table S6.4. Continuation of the summary of the RDF analysis for fcc-$Ti_{0.94}Cr_{0.06}N_{1-x}B_x$ and fcc-$Ti_{0.94}Zr_{0.06}N_{1-x}B_x$ structures, with increasing B content evaluated for the nearest neighbor Cr–Ti, Cr–B, Cr–N, Zr–Ti, Zr–B, and Zr–N bonds, including the standard error (SE). Cr–Cr and Zr–Zr bonds are not listed because the alloy content is insufficient for two Cr or Zr atoms being nearest neighbors

fcc-$Ti_{0.94}Cr_{0.06}N_{1-x}B_x$									
Ti	Cr	B	N	Cr–Ti (Å)		Cr–B (Å)		Cr–N (Å)	
(at.%)	(at.%)	(at.%)	(at.%)	d	SE	d	SE	d	SE
46.88	3.13	1.56	48.44	3.005	<0.001	2.143	0.001	2.124	0.001
		3.13	46.88	3.011	<0.001	2.140	0.000	2.126	0.001
		4.69	45.31	3.015	0.001	2.150	0.001	2.128	0.001
		6.25	43.75	3.020	0.001	2.157	0.001	2.131	0.001
		7.81	42.19	3.025	0.001	2.159	0.001	2.132	0.001
		9.38	40.63	3.033	0.001	2.160	0.001	2.134	0.001
		10.94	39.06	3.035	0.001	2.166	0.001	2.136	0.002

fcc-$Ti_{0.94}Zr_{0.06}N_{1-x}B_x$									
Ti	Zr	B	N	Zr–Ti (Å)		Zr–B (Å)		Zr–N (Å)	
(at.%)	(at.%)	(at.%)	(at.%)	d	SE	d	SE	d	SE
46.88	3.13	3.13	46.88	3.050	0.001	2.173	0.001	2.157	0.002
		4.69	45.31	3.036	<0.001	2.164	0.001	2.148	0.001
		6.25	43.75	3.038	<0.001	2.162	0.001	2.152	0.001
		7.81	42.19	3.045	<0.001	2.168	0.001	2.154	0.002
		9.38	40.63	3.050	0.001	2.173	0.001	2.157	0.002
		10.94	39.06	3.054	0.001	2.178	0.001	2.159	0.001

7 Actually Measuring Thin Film Elastic Constants by Combined X-ray Microdiffraction and Micromechanical Testing

Experimentally assessing direction-dependent elastic constants is still far from routine and poses significant technical and analytical challenges. While nanoindentation offers insights into reduced polycrystalline Young's moduli, directly measuring direction-dependent elastic constants in thin films necessitates innovative methodologies due to inherent challenges compared to bulk materials. Although ab initio Density Functional Theory calculations offer theoretical input, discrepancies persist between model systems and real-world properties, primarily due to a lack of available experimental data for newly emerging—and often chemically and structurally complex—material systems. Moreover, theoretical formulations typically rely on single-crystal elastic constants, overlooking microstructural influences that significantly impact material behavior. Recent advancements in in-situ micromechanical testing utilizing X-ray diffraction provide a powerful approach for studying the stress-strain distribution in thin films, however, the stress state imposed by these methods deviates from simple uniaxial conditions. Our study addresses this gap by proposing a novel experimental approach to measure direction-dependent elastic constants, combining synchrotron microdiffraction and micropillar compression testing. Our investigation focuses on the experimental determination of direction-dependent elastic constants in a polycrystalline face-centered cubic $TiN_{0.8}B_{0.2}$ thin film (H=32.1±1.9 GPa), where linear elastic failure prevails. We established an advanced in-situ testing environment where we continuously recorded the load-displacement of the indenter during loading, while simultaneously collecting the material's deformation response to uniform uniaxial compression in the form of full Debye-Scherrer Patterns for {111}, {200}, and {220} peaks. This dynamic approach allowed for the evaluation of the orientation-dependent elastic strain components as well as the macroscopic uniaxial compressive stresses, each over time, enabling a differential analysis to assess the elastic and X-ray elastic constants. By correlating our experimental results with ab initio calculations, we provide a robust and new method for validating theoretical predictions and advancing thin film material testing and design.

7.1 Introduction

While searching for new materials drives progress in materials science, the journey toward their target application requires careful evaluation and testing. In particular, ceramic coatings—fabricated via Physical Vapor Deposition (PVD) methods—have become a central focus of modern materials engineering owing to their superior mechanical properties, e.g., high hardness and wear resistance [1–5]. However, to optimize their performance and ensure reliability under—oftentimes—extreme operating conditions, it is critical to understand their mechanical behavior [6]. Among the commonly analyzed mechanical properties of ceramic thin films such as hardness, H, and fracture toughness, K_{IC}; Young's modulus, E, and Poisson's ratio, ν, serve as fundamental descriptors of a material's response to external forces, where ν quantifies the transverse deformation of a material in response to axial loading and E reflects the material's stiffness in resisting such deformation. In materials engineering, H and K_{IC} are technologically relevant quantities mainly accessible by experimental approaches, where H is usually measured using nanoindentation techniques and K_{IC} can be derived from micromechanical tests (e.g., micro-cantilever bending tests)[7–12].

However, the complex interplay of various contributing factors—including point defects and dislocation dynamics—across multiple length scales makes it difficult to approach these descriptors within the modeling framework. In ceramic coatings, H is not only determined by the ease of the dislocation movement (overcoming the Peierls barrier [13,14]) but also by several hardening mechanisms [15–20] related to the material's microstructure and defect density. Contrarily, theoretical hardness and fracture toughness formulas typically take single-crystal elastic constants as the main input [21–23], as these can be quite straightforwardly evaluated by ab initio methods (using the stress-strain [24,25] or the energy-strain method [26] or even machine-learned using suitable ab initio training sets [27–29]. Among the most widely used K_{IC} approximates is Griffith's formula [30], completely omitting plastic deformation [20,31] or any microstructural features that can significantly alter resistance to unstable crack propagation. Griffith's formula relies on the surface energy and the directional Young's modulus, hence, again, elastic constants.

Zero Kelvin *ab initio* elastic constants calculations, though computationally expensive for chemically complex materials, can nowadays be seen as routine and have been employed to screen across many material systems [32–34]. With the advance of computational power as well as the rapidly developing field of machine-learning interatomic potentials for molecular dynamics, also finite-temperature elastic constants are becoming accessible [35–37]. In a stark contrast, direct elastic constants measurements for ceramic-type coatings are still far from routine. Distinct from bulk materials, their inherent characteristic of being *thin* films introduces additional complexities that necessitate advanced testing methodologies. Crystallographic anisotropy and texture as well as typical columnar/fibrous grained morphology obtained from PVD thin film growth further complicates the mechanical behavior of ceramic coatings. Together, these structural characteristics lead to directional dependencies in elastic properties along different crystallographic planes, as well as direction dependence with respect to the film growth direction.

Nanoindentation, especially when performed according to Fisher-Cripps [38], provides a convenient approach to determine the reduced polycrystalline modulus of ceramic hard coatings. Using this method, the film-only reduced modulus at zero indentation depth can be extrapolated by fitting a power-law function to the load-displacement data from multiple indentations of varying depths. If the Poisson ratio of the material is known, the polycrystalline Young's modulus can be further calculated. The implementation of X-ray diffraction-based techniques can provide access to the X-ray elastic constants (DECs) of polycrystalline thin films, e.g., by coupling the $\sin^2\psi$ method with the substrate curvature technique [39]. The work of Martinschitz et al. [40] further accounted for the macroscopic elastic anisotropy in textured Cu and CrN thin films by extrapolating the moduli from the experimentally determined thin film DECs. In 2020, Alfreider et al. [41] performed in-situ micro-tensile testing in SEM in combination with a digital image correlation technique to map the true stress-strain state of a nanocrystalline high entropy alloy, enabling the evaluation of the polycrystalline Poisson's ratio. Another method that has been introduced in the last few years is the use of μ-mechanical spectroscopy to determine the elastic modulus of a material by cantilever bending. Examining the shape of the first resonance peak of the indentation setup used, it is possible to detect changes in the damping capability of confined volumes [42,43].

In-situ micromechanical testing methods provide a powerful tool to study material's response to various loading conditions, specifically tailored to investigate small-scale geometries [44]. One such approach combines micromechanical testing and X-ray diffraction, where synchrotron facilities provide advanced access to probe the crystallographic structure and lattice strain of thin films under mechanical stress with exceptional sensitivity [45,46]. Advances in optics and beamline instrumentation allow for intense and highly collimated X-ray beams of very small size—while maintaining high brilliance—that facilitate in-situ measurements of stress-strain distributions in thin films with unprecedented spatial resolution and accuracy, even at the nanoscale [47]. However, it is important to acknowledge that the stress state induced by previously reported in-situ micromechanical testing methods such as nanoindentation or micro-cantilever bending is inherently complex and deviates from the ideally simple uniaxial loading conditions typically assumed in classical mechanics [48–53].

In this study, we present a new methodology designed to accurately measure the direction dependent elastic constants in thin film ceramic hard coatings. Using the combined approach of X-ray microdiffraction and micropillar compression testing, a micropillar fabricated from a 15 µm polycrystalline face centered cubic (fcc) $TiN_{0.8}B_{0.2}$ hard coating (prepared by non-reactive DC PVD sputtering) to uniaxial compression testing while simultaneously recording its elastic response (to failure) for the {111}, {200}, and {220} crystallographic planes using a high-energy monochromatic synchrotron radiation source and fast acquisition times (0.55 s). By implementing a high-precision continuous stiffness measurement (CSM) nanoindentation setup, we enabled real-time monitoring of indenter displacement and force during testing. This dynamic approach allowed a differential analysis of the time-dependent elastic deformation of the material under uniform uniaxial loading condition, providing accurate experimental values of elastic and diffraction elastic constants for three independent crystallographic planes for a selected face-centered cubic polycrystalline ceramic thin film material. Supported by ab initio density functional calculations, the experimentally determined {*hkl*}-dependent Poisson's ratio, Young's modulus and X-ray elastic constants (DECs) were further compared with their theoretically derived values. By bridging experimental observations with theoretical modeling, we aim to step forward in the direction of a fundamental understanding of the mechanical properties of thin film ceramics, using Ti–B–N as a representative material system.

7.2 Materials and Methods

7.2.1 Thin Film Deposition

The $TiN_{0.8}B_{0.2}$ coating was deposited on single crystal sapphire $(1\bar{1}02)$ substrates with dimensions of 10×10×0.53 mm^3 using a modified Leybold Heraeus Z400 deposition system equipped with a 3” unbalanced magnetron sputtering source holding a $TiN+TiB_2+Ti$ composite target composed of 80 mol.% TiN + 15 mol.% TiB_2 + 5 mol.% Ti with 99.5 % purity from Plansee Composite Materials GmbH. The substrates were ultrasonically pre-cleaned in acetone and isopropyl alcohol for 5 min each, then mounted in the 3” substrate holder and loaded into the chamber. The target-to-substrate distance was fixed at 40 mm. After reaching the base pressure of $\leq 2 \cdot 10^{-4}$ Pa ($\leq 2 \cdot 10^{-6}$ mbar), the substrates were thermally cleaned at 400 °C for 20 min, followed by Ar ion etching using an Ar pressure (60 sccm Ar flow) of 1.6 Pa and applying a negative bias voltage of -150 V (pulsed DC, 150 kHz, 2496 ns pulse duration). The target was operated at 0.50 A (no substrate bias applied, floating potential -24 V) at an Ar pressure of 0.4 Pa (32 sccm Ar flow) and a substrate temperature of 400 °C for 400 min to achieve a thickness of t~15 µm.

7.2.1 Thin Film Characterization

Structural information was obtained by X-ray diffraction (XRD) analysis using a Malvern PANalytical XPert Pro MPD (θ-θ diffractometer) in Bragg-Brentano geometry equipped with a CuK_α radiation source operating at 45 kV and 40 mA monochromatized with a Malvern PANalytical BBHD mirror suppressing K_β. Fracture cross sections were imaged using a Zeiss SIGMA 500 VP Field Emission Gun-Scanning Electron Microscope (FEG-SEM) operating at 10 kV.

Hardness, H, and Young's modulus, E, were determined by instrumented nanoindentation using a FemtoTools FT-IO4 Femto-Indenter system equipped with a diamond Berkovich tip (calibration was performed on a standard fused silica sample) in Continuous Stiffness Measurement (CSM) mode. 25 load-displacement curves were analyzed according to Oliver and Pharr [54] using a maximum force of 20 mN. The reduced raw moduli data were fitted with a power law as a function of the penetration depth, extrapolated to zero indentation depth, and corrected according to Fischer-Cripps [38] to yield the film-only Young's modulus.

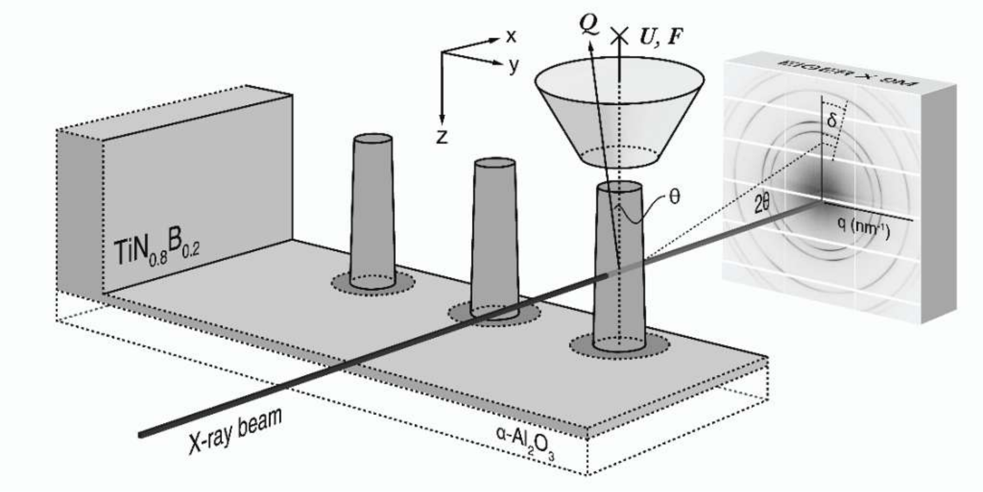

Figure 7.1. A schematic view of the in-situ X-ray microdiffraction experiment performed in transmission diffraction geometry using a monochromatic X-ray beam with a spot size of 1.5 × 1.5 µm², centered in the mid-section of the free-cut $TiN_{0.8}B_{0.2}$ micropillar sample. The micropillar (aspect ratio 3:1) was loaded in z direction using a diamond flat punch tip with a contact area of ~ 80 µm², positioned on top of the pillar along the z axis. The force, F, and the indenter displacement, U, were simultaneously recorded during testing. 2D diffraction data were collected during the experiment using an Eiger X 9M photon counting detector. The direction of the strain measurement is identified by the angles θ and δ, where θ is the angle of inclination of the diffraction vector, $\bar{Q}_{\theta\delta}$, with respect to the equatorial plane defined by the incident beam and δ denotes the azimuth angle within this plane.

7.2.3 Combined Synchrotron X-ray Microdiffraction and Micromechanical Testing

A cross-sectional lamella (~100 µm thick in the beam direction) of our $TiN_{0.8}B_{0.2}$ thin film was prepared by cutting and mechanically polishing the coated sapphire substrate. After preparation, the lamella was securely mounted on a sample holder designed for precise alignment in the beam direction without affecting the diffracted beam paths during the experiment. Cylindrical micropillar geometries were fabricated from the cross-sectional lamella by Focused Ion Beam (FIB) milling using a ThermoFisher Scios 2 DualBeam system operated at 30 kV. First, a selected area of the coating material (~120 × 100 × 15 μm^3) was removed with a probe current of 30 nA, except for three free-standing pillars of ~ 10 µm in diameter. By reducing the milling current stepwise to 500 pA, the pillar walls were refined to a final pillar diameter of ~ 5 µm with a height-to-diameter aspect ratio of ~ 3:1 and a taper angle of less than 2°. During the in-situ XRD experiment, one micropillar was compressed using a FemtoTools FT-NMT04 in-situ nanoindentation system operating in intrinsic displacement-controlled mode at a load rate of 5 $nm \cdot s^{-1}$, equipped with a FemtoTools FT-S200'000 diamond flat punch tip customized to a final diameter of ~ 10 µm using the FIB system mentioned above. Force and displacement data were collected throughout the experiment, including ~ 100 s after failure. The in-situ micropillar compression testing was conducted at the Nanofocus Endstation of the MiNaXS (P03) beamline at the PETRA III (3rd generation synchrotron radiation source) at Deutsches Elektronen-Synchrotron (DESY). The monochromatic X-ray beam with a photon energy of 19.7 keV was focused by a KB mirror setup [47] down to lateral dimensions of 1.5 × 1.5 μm^2. The nanoindentation system was built into the X-ray measurement setup to analyze the micropillar sample in transmission wide-angle diffraction geometry. Before testing, the diamond flat punch tip was centered directly over the pillar top surface to guarantee uniform conditions during loading (see Fig. 7.1). In order to center the pillar mid-section to the X-ray beam, the nanoindentation-sample holder assembly was positioned using a hexapod for tilt and rotational alignment, complemented by a linear nano-positioning high load stage for x-, y-, and z-alignment. The diffracted photons were collected using an Eiger X 9M Hybrid Photon Counting (HPC) 2D detector, with an acquisition time of 0.55 s per frame, positioned at a sample-detector distance of 0.236 m to record the full Debye-Scherrer ring including {111}, {200}, and {220} peaks. The exact parameters of the diffraction geometry were calibrated by measuring a LaB_6 standard reference powder.

7.2.4 Synchrotron X-ray Microdiffraction Data Analysis

Strain Analysis

From the collected Debye-Scherrer ring patterns at the pillar cross-sectional position (y, z) the orientation-dependent lattice plane spacing $d_{\theta\delta}^{hkl}(y, z)$ can be obtained from its relation to the diffraction angle $2\,\theta^{hkl}\,(\delta)$ and the wave length λ according to Bragg's law,

$$\lambda = 2d_{\theta\delta}^{hkl}(y, z)\sin\theta^{hkl} \tag{7.1}$$

whereas the X-ray elastic strain $\varepsilon_{\theta\delta}^{hkl}(y, z)$ has to be calculated from

$$\varepsilon_{\theta\delta}^{hkl}(y, z) = \frac{d_{\theta\delta}^{hkl}(y, z) - d_0^{hkl}}{d_0^{hkl}} \tag{7.2}$$

with d_0^{hkl} as the strain-free lattice plane spacing. Therefore, each of the recorded 2D patterns was subjected to azimuthal integration using the open-source software package DPDAK [55], where azimuthal angle δ segments of 10 deg–with δ ranging from -5 to 355°–were integrated. The lattice plane spacing $d_{\theta\delta}^{hkl}(y, z)$ of the $\{111\}$, $\{200\}$, and $\{220\}$ peaks was determined by fitting a pseudo-Voigt peak shape function to the 1D intensity profiles–obtained for 36 azimuthal angles δ sections as a function of $2\,\theta^{hkl}\,(\delta)$–according to Eq. (7.1). For each of the three crystallographic plane families, we identified the unstrained lattice plane spacing d_0^{hkl} from the intersection of the linear fits of the 36 previously calculated $d_{\theta\delta}^{hkl}(y, z)$ data points for 62 shots plotted against $\sin^2\delta$, i.e., 62 collected Debye-Scherrer ring patterns (up to one recording before failure) were considered for an initial evaluation of the d_0^{hkl} value (see Supplementary Material). Here, the rationale is that the $d_{\theta\delta}^{hkl}(y, z)$ which has shown to be independent on the applied load must be the strain-free value d_0^{hkl}.

Following the procedure from [51], the measured orientation-dependent elastic strain $\varepsilon_{\theta\delta}^{hkl}(y, z)$ obtained from Eq. (7.2) can be expressed as a function of six unknown strain components, $\varepsilon_{ij}^{hkl}(y, z)$, given by

$$\begin{aligned}\varepsilon_{\theta\delta}^{hkl}(y, z) = {} & \sin^2\theta\,\varepsilon_{xx}^{hkl}(y, z) + \cos^2\theta\,\sin^2\delta\,\varepsilon_{yy}^{hkl}(y, z) + \cos^2\theta\,\cos^2\delta\,\varepsilon_{zz}^{hkl}(y, z) \\ & - \sin 2\theta\,\cos\delta\,\varepsilon_{zx}^{hkl}(y, z) + \cos^2\theta\,\sin 2\delta\,\varepsilon_{zy}^{hkl}(y, z) - \sin 2\theta\,\sin\delta\,\varepsilon_{xy}^{hkl}(y, z)\end{aligned} \tag{7.3}$$

Under uniaxial loading conditions, the pillar experiences compressive strain, $\varepsilon_{zz}^{hkl}(y,z)$, along its longitudinal z-axis. Simultaneously, due to Poisson's effect and its cylindrical geometry, the pillar expands uniformly in all directions perpendicular to the applied load, resulting in equal lateral strain components in x and y direction, $\varepsilon_{xx}^{hkl}(y,z) = \varepsilon_{yy}^{hkl}(y,z)$, negligible off-axis shear strain, $\varepsilon_{xy}^{hkl}(y,z) = 0$, and equal but near-zero on-axis shear strain components, $\varepsilon_{zx}^{hkl}(y,z) = \varepsilon_{zy}^{hkl}(y,z) \approx 0$. These simplifications assume an elastic isotropic material behavior, facilitating/reducing the analysis of the pillar deformation from Eq. (7.3) to three unknown strain components

$$\begin{aligned}\varepsilon_{\theta\delta}^{hkl}(y,z) = \varepsilon_{yy}^{hkl}(y,z)\,[\sin^2\theta + \cos^2\theta\,\sin^2\delta] + \varepsilon_{zz}^{hkl}(y,z)\cos^2\theta\,\cos^2\delta \\ - \varepsilon_{zy}^{hkl}(y,z)[\sin 2\theta\cos\delta - \cos^2\theta\,\sin 2\delta]\end{aligned} \tag{7.4}$$

During the experiment, every 5.55 s a 2D diffractogram was recorded over a period of ~450 s. From a single Debye-Scherer ring, 36 strain values $\varepsilon_{\theta\delta}^{hkl}(y,z)$ were evaluated according to Eq. (7.2). For each measurement/shot, we calculated the three unknown strain components $\varepsilon_{yy}^{hkl}(y,z)$, $\varepsilon_{zz}^{hkl}(y,z)$, and $\varepsilon_{zy}^{hkl}(y,z)$ by solving the linear equation system (based on 36 linear equations) using a least-squares refinement method. Thus, the orientation-dependent Poisson's ratio, ν^{hkl}, can be extracted from

$$\nu^{hkl} = -\frac{\frac{d}{dt}\varepsilon_{yy}^{hkl}(y,z)}{\frac{d}{dt}\varepsilon_{zz}^{hkl}(y,z)} \tag{7.5}$$

Poisson's Ratio and Unstrained Lattice Parameter Refinement

From uniform unidirectional loading conditions, the Poisson's ratio $\nu_{d_0}^{hkl}(x,y)$ of an elastic material is related to the ratio of the transverse and axial strain components, $\varepsilon_{yy}^{hkl}(y,z)$ and $\varepsilon_{zz}^{hkl}(y,z)$, similar to Eq. (7.5)

$$\nu_{d_0}^{hkl}(x,y) = -\frac{\varepsilon_{yy}^{hkl}(y,z)}{\varepsilon_{zz}^{hkl}(y,z)} \tag{7.6}$$

where $\nu_{d_0}^{hkl}(x,y)$ can be calculated for each $\varepsilon_{yy}^{hkl}(y,z)$ and $\varepsilon_{zz}^{hkl}(y,z)$ value extracted from the periodic 2D diffraction patterns collected during the compression test. In particular, when ν^{hkl} is obtained from the ratio of the slope between the calculated $\varepsilon_{yy}^{hkl}(y,z)$ and $\varepsilon_{zz}^{hkl}(y,z)$ data points (according to Eqs. (7.2), (7.4), and (7.5)), ν^{hkl} is presumed to be independent of the precise determination of d_0^{hkl} from the $d_{\theta\delta}^{hkl}(y,z)$ vs. $\sin^2\delta$ relation. Notably, the slope-over-time approach is only valid if the rate of deformation is constant (as provided by our indentation setup). Using MATLAB's "fminsearch" optimization algorithm [56] for data points between 67 and 333 s we iteratively adjusted d_0^{hkl} in Eq. (7.4) to align the d_0^{hkl}-dependent $\nu_{d_0}^{hkl}(x,y)$ values from Eq. (7.6) by the method of least-squares to closely match the Poisson's ratio from Eq. (7.5), resulting in a more precise unstrained lattice plane spacing, $d_{0,\mathrm{r}}^{hkl}$, for each of the three reflections. Thus, only refined $d_{0,\mathrm{r}}^{hkl}$ were used for subsequent calculations including the evaluation of $\varepsilon_{ij}^{hkl}(y,z)$, $\sigma_{zz}^{hkl}(y,z)$, and from there ν^{hkl}, E^{hkl}, $\frac{1}{2}s_2^{hkl}$, and s_1^{hkl}.

Stress Analysis

Based on the continuously recorded load-displacement data from the indenter probe, the indentation stress, $\sigma_I(y,z)$, is calculated as the ratio between the applied force F and the area of the pillar mid-section, $A_m(y,z)$

$$\sigma_I(y,z) = -\frac{F}{A_m(y,z)} \tag{7.7}$$

Notably, the cross-sectional area of the pillar mid-section irradiated during loading is used instead of the top surface contact area, to account for the pillar's taper.

Considering the basic principle of Hooke's law, which connects the induced elastic strain to the applied mechanical stress,

$$\varepsilon_{ij} = \frac{1}{C_{ijkl}}\sigma_{kl} \tag{7.8}$$

where ε_{ij} is the strain tensor, C_{ijkl} is the stiffness tensor and σ_{kl} is the stress tensor, the linear relationship between the measured strain, $\varepsilon_{\theta\delta}^{hkl}(y,z)$, and the only non-zero deviatoric stress component $\sigma_{zz}(y,z)$— acting under uniaxial compression testing in z-direction—can be expressed according to

$$\varepsilon_{\theta\delta}^{hkl}(y,z) = \frac{1+\nu^{hkl}}{E^{hkl}}\sigma_{zz}(y,z)\sin^2\delta - \frac{2\nu^{hkl}}{E^{hkl}}\sigma_{zz}(y,z) \tag{7.9}$$

Where the proportionally constant E^{hkl} is the elastic modulus. Introducing the {*hkl*}-dependent (X-ray) elastic constants (DECs) [57],

$$s_1^{hkl} = -\frac{\nu^{hkl}}{E^{hkl}} \tag{7.10}$$

and

$$\frac{1}{2}s_2^{hkl} = \frac{1+\nu^{hkl}}{E^{hkl}} \tag{7.11}$$

the stress-strain relation from Eq. (7.9) is given by

$$\varepsilon_{\theta\delta}^{hkl}(y,z) = \frac{1}{2}s_2^{hkl}\sigma_{zz}(y,z)\sin^2\delta + 2s_1^{hkl}\sigma_{zz}(y,z) \tag{7.12}$$

Given the relatively small elastic anisotropy of our $TiN_{0.8}B_{0.2}$ coating material with an ab initio calculated Zener anisotropy ratio of 0.7873 [58] and assuming a uniaxial stress state within the radiated pillar mid-section during the experiment [59], we derive the out-of-plane stress for each of the three {*hkl*} reflections, $\sigma_{zz}(y,z)$, as follow [60]

$$\frac{\partial d_{\theta\delta}^{hkl}(y,z)}{\partial \sin^2\delta} = \sigma_{zz}(y,z)\frac{1}{2}s_2^{hkl}d_{0,\mathrm{r}}^{hkl} \tag{7.13}$$

Using the expression of $\varepsilon_{\theta\delta}^{hkl}(y,z)$ from the normalized lattice plane spacing difference, $d_{\theta\delta}^{hkl}(y,z) - d_{0,\mathrm{r}}^{hkl}$, from Eq. (7.2) and plotting $d_{\theta\delta}^{hkl}(y,z)$ against $\sin^2\delta$, the deviatoric stress, $\sigma_{zz}^{hkl}(y,z)$, can be determined from the slope of the curve, where $\frac{1}{2}s_2^{111} = 2.9879 * 10^{-3}\ \mathrm{GPa}^{-1}$, $\frac{1}{2}s_2^{200} = 2.6400 * 10^{-3}\ \mathrm{GPa}^{-1}$, and $\frac{1}{2}s_2^{220} = 2.9010 * 10^{-3}\ \mathrm{GPa}^{-1}$, and, in addition, the values for s_1^{hkl} are obtained using the ISODEC software package [61] based on the inverse Kröner model [62,63], considering the values from the ab initio calculated stiffness tensor for our deposited Ti–B–N material system with $C_{11} = 548.29$, $C_{12} = 133.15$, and $C_{44} = 163.43$ (cubic symmetry).

Elastic Modulus and Diffraction Elastic Constants

Theoretically, the obtained deviatoric stresses, $\sigma_{zz}(y,z)$, remain consistent across different crystallographic planes and correspond to the {*hkl*}-independent macro stresses, $\sigma_I(y,z)$, derived from the probe-to-sample response continuously recorded by the nanoindentation system during loading and calculated according to Eq. 7.7. By incorporating the discrete indentation stress values, $\bar{\sigma}_I(y,z)$, into Eq. (7.13), we accessed $\frac{1}{2}S_2^{hkl}$ directly from the experimental data. Alternatively, $\frac{1}{2}S_2^{hkl}$ can be expressed in Eq. (7.13) as:

$$\frac{\partial d_{\theta\delta}^{hkl}(y,z)}{\partial \sin^2\delta} = \bar{\sigma}_I(y,z)\left(\frac{1}{2}S_2^{hkl}\right)d_{0,\mathrm{r}}^{hkl} \tag{7.14}$$

to further determine the {*hkl*}-dependent Young's modulus, E^{hkl} (according to Eq. (7.11)). To synchronize the continuous $\sigma_I(y,z)$ values with the discrete strain, $\varepsilon_{\theta\delta}^{hkl}(y,z)$, and lattice parameter, $d_{\theta\delta}^{hkl}(y,z)$, data (recorded for 5.00 s adding 0.55 s acquisition time), we averaged the indenter stresses, $\bar{\sigma}_I(y,z)$, over 5.55 s time intervals. According to Eq. (7.12), S_1^{hkl}can be derived similarly to $\frac{1}{2}S_2^{hkl}$ by replacing $\sigma_{zz}^{hkl}(y,z)$ with $\bar{\sigma}_I(y,z)$. Notably, $\frac{1}{2}S_2^{hkl}$ and S_1^{hkl} denote the experimentally determined thin film diffraction elastic constants, where $\frac{1}{2}s_2^{hkl}$ and s_1^{hkl} refer to the single-crystal DECs derived from C_{ijkl}.

Additional information can be gathered by plotting the evaluated experimental and ab initio DFT simulated DECs against the parameter 3Γ [64], which is defined as follows

$$3\Gamma = 3\frac{h^2k^2 + k^2l^2 + l^2h^2}{(h^2+k^2+l^2)^2} \tag{7.15}$$

where h, k, and l are the Millers indices and 3Γ is a single parameter expression for the Miller indices in cubic crystal structures. Plotting the X-ray elastic constants obtained from the single-crystalline ab initio DFT data using the Reuss [57,65], Voigt [66] and Eshelby/Kröner [67] grain interaction models against the 3Γ parameter will lead to 3 lines with different slopes and a single intersection. The calculation of DECs from the single-crystalline stiffness tensor according to the three models was taken from literature and is presented in detail in [68]. Since the theoretical boundaries of possible X-ray elastic constants are set by (i) the Reuss and the Voigt grain-interaction models and (ii) at the intersection these culminate into a single point. In following it will be assumed, that this specific 3Γ value determined for the ab initio DFT data is also valid for the experimentally determined DECs, which will be interpolated to retrieve the experimental polycrystalline $\{hkl\}$-independent Young's modulus, E, and Poisson's ratio, ν.

7.2.5 Density Functional Analysis

The Vienna Ab-initio Simulation Package (VASP) [69,70] implementation of the Density Functional Theory (DFT) was used to carry out ab initio calculations. The Perdew-Burke-Ernzerhof generalized gradient approximation (GGA) [71] and the plane-wave projector augmented wave (PAW) pseudopotentials [72] were employed. Consistently with our previous study [6], the plane-wave cutoff energy was set to 600 eV, and the reciprocal space was sampled with Γ-centred k-point meshes with a length parameter of 60Å. All supercells were based on the cubic rocksalt ($Fm\bar{3}m$) TiN structure in which the desired number of B atoms was distributed on the N sublattice (to model the TiB_xN_{1-x} solid solution) using the Special Quasirandom Structure approach [73]. Three supercell orientations were considered: (i) x ∥ $[100]$, y ∥ $[010]$, z ∥ $[001]$ (total of 64 atoms); (ii) x ∥ $[110]$, y ∥ $[1\bar{1}0]$, z ∥ $[001]$ (total of 72 atoms); and (iii) x ∥ $[111]$, y ∥ $[1\bar{1}0]$, z ∥ $[11\bar{2}]$ (total of 72 atoms). The supercells (ii) and (iii), with different numbers of atoms, are visualized in Fig. 1 of [74]. All supercells were fully optimized by relaxing their volume, cell shape, and atomic positions.

The fourth-order elasticity tensor, $\mathbb{C}$, was evaluated for the supercell (i) using the stress-strain approach [24,25] with a strain magnitude of 1.9 %. Applying Voigt's formalism, the tensor was mapped onto a 6×6 matrix, C_{ij}, and subsequently projected onto that of a cubic crystal [75], yielding three independent elastic constants: C_{11}, C_{12}, and C_{44}. The polycrystalline Young's modulus, E, bulk modulus B, and shear modulus G, were calculated as Hill's average [76] of the upper bounds according to Reuss's approach (subscript "R") [65] and the lower Voigt's bounds (subscript "V") [66]. The polycrystalline Poisson ratio was calculated using:

$$\nu = \frac{3 \cdot B - 2 \cdot G}{6 \cdot B + 2 \cdot G} \tag{7.16}$$

The directional Young's modulus, E^{hkl}, was evaluated following formulas in Nye [77] (p. 143–145). Additionally, we used supercells (ii) and (iii) to simulate uniaxial $[001]$ and $[110]$ compression tests with a 1% strain step, where at each consecutive step the supercell and the ionic positions were allowed to relax in the directions orthogonal to the applied strain. The predicted lattice parameter changes along the main crystallographic directions allowed us to directly evaluate the (directional) Poisson ratio by calculating the negative first derivative of the resulting average orthogonal strain over the applied strain.

7.3. Results and Discussion

7.3.1 Materials Characterization

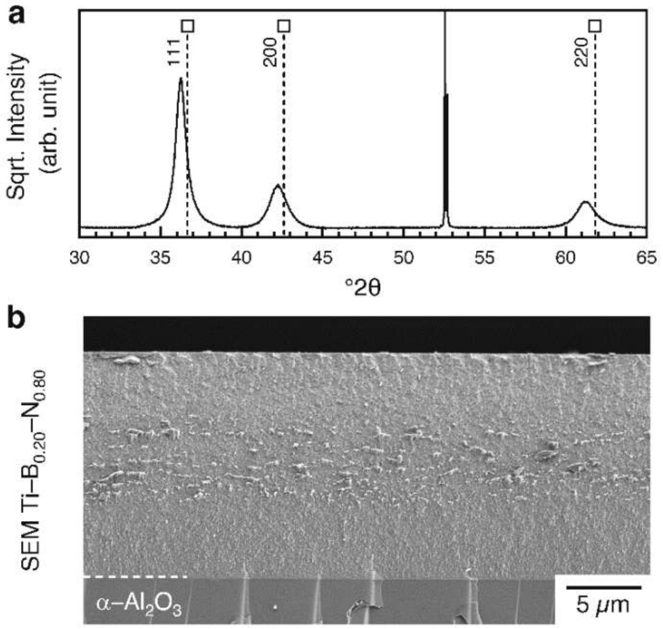

Figure 7.2. (a) XRD pattern recorded for $TiN_{0.8}B_{0.2}$ showing standard peak positions corresponding to the (111), 2θ = 36.663°, (200), 2θ = 42.597°, and (220), 2θ = 61.814° crystallographic planes of fcc-TiN (JCPDS No. 00-038-1420) [78]. (b) Cross section morphology of the deposited $TiN_{0.8}B_{0.2}$ coating with 15 μm film thickness on α-Al_2O_3 substrate.

To provide a suitable base coating for in-situ micropillar compression testing, we deposited a 15 μm thick polycrystalline $TiN_{0.8}B_{0.2}$ coating from a TiN+TiB_2+Ti composite target similar to the 3 μm version characterized by elastic recoil detection analysis (ERDA) reported in [6]. The XRD pattern, Fig. 7.2a, reveals three distinctive peaks corresponding to the crystallographic planes (111), (200), and (220) of fcc-TiN. The peak shift towards lower 2θ values is mainly due to the incorporation of B into the fcc TiN lattice, as described in detail in previous studies [6]. We further evaluated the residual compressive stresses in Ti–B–N films on the order of about 2.5 GPa, accounting for ~ 1% of the observed peak shift. Importantly, only the fcc-Ti(N,B) structure is identified, confirming the absence of any other crystalline phase.

The cross section of the $TiN_{0.8}B_{0.2}$ coating in Fig. 7.2b exhibits a compact, dense growth morphology different from the columnar structure commonly observed in polycrystalline hard coatings. Instead, a refined microstructure is present with an average grain size of 18 ± 7 nm [6]. We have recently addressed the effect of B-solubility on the microstructure and mechanical properties of Ti–B–N thin films [6], guiding our material selection for this experiment.

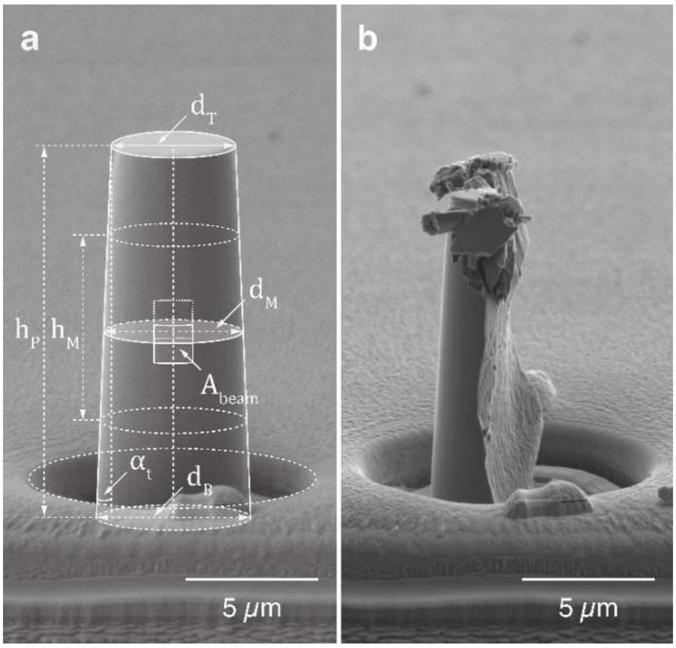

Figure 7.3. (a) Schematic representation of the micropillar's geometric parameters. The actual height of the pillar, $h_P = 15.01 \pm 0.05$ μm, aligns with the film thickness with a taper angle $\alpha_t < 2°$. The top surface diameter, d_T, measures 4.57 ± 0.05 μm, while the bottom diameter, d_B, is ≈ 5.5 μm; albeit with a slight circular foot transition that complicates precise determination. The mid-section of the pillar, measured at half its height has a diameter of $d_T = 5.04 \pm 0.05$ μm with a cross-sectional area $A_m = 19.96$ μm^2. The central region where the micropillar experiences a nearly uniaxial stress state is marked as $h_M = 7.51 \pm 0.05$ μm. During the experiment, the center of the pillar was fixed in transmission geometry perpendicular to the beam direction with a cross-section diameter $A_{beam} = 1.5 \times 1.5$ μm^2. Auxiliary lines were extrapolated to the foot level to illustrate the complete pillar geometry. (b) Fractured $TiN_{0.8}B_{0.2}$ micropillar after compression testing, displaying brittle behavior consistent with the ceramic nature of the material.

Micropillars were FIB milled from the deposited $TiN_{0.8}B_{0.2}$ thin film for subsequent compression testing. Fig. 7.3a shows the micropillar before testing, with its geometric specifications outlined in white. Our FIB milling protocol induces a nearly symmetrical taper (α_t, left side 1.94°, right side 1.81°) along the pillar, resulting in a slightly non-uniform cylinder with an aspect ratio $h_P : d_T \approx 3$, proven to be practical and suitable for compression testing [59]. Notably, the selected sample geometry should provide a sufficient probe volume (i.e., number of grains) to interact with the X-ray beam ($A_{beam} = 1.5 \times 1.5\ \mu m^2$) in order to facilitate a comprehensive characterization of the material response to applied loads (see Fig. 7.3a). In [59], Cornec and Lilleodon critically discussed the aspects of determining stress-strain curves from micropillar compression tests. Their computational models verified that a nearly uniaxial stress state occurs in the center of the micropillar over $\sim h_M$, see Fig. 7.3a. However, frictional forces and constrained deformation along the top (and bottom) surface of the micropillar result in lateral and shear stresses (i.e., non-uniform stress distributions) due to contact with the indenter during loading. We therefore chose to irradiate the specimen at its midpoint. Post-testing, the fracture surface of the $TiN_{0.8}B_{0.2}$ micropillar exhibits characteristic features associated with brittle failure. The SEM image in Fig. 7.3b shows a distinct fracture surface morphology characterized by smooth fracture lines, with the right side of the pillar separated from the remaining left part. This unilateral fracture indicates an abrupt and catastrophic failure event that propagated along the vertical axis of the pillar. The absence of significant plastic deformation features (e.g., distortion or shear bands), further confirms that the fracture mechanism is predominantly brittle.

7.3.2 X-ray Strain Analysis

In-situ compression testing was conducted at a constant loading rate of 5 nm·s^{-1} while recording a 2D diffraction pattern at regular intervals of 5.00 s (adding the acquisition time of the detector of 0.55 s) for a period of 450 s, ensuring controlled loading conditions for precisely monitoring the pillar material's mechanical response throughout the test. All experimental results were plotted for 400 s, with loading starting at ~42 s and failure occurring at ~350 s.

Fig. 7.4 presents the three resulting strain components ε_{zz}^{hkl}, ε_{yy}^{hkl}, and ε_{zy}^{hkl} for three crystallographic planes {*hkl*}, {111}, {200}, and {220}. The strain values were determined by 2D X-ray diffraction data analysis (as detailed in the experimental section) according to Eq. (7.4). The predominant axial strain component, ε_{zz}^{hkl}, corresponds to the loading direction, i.e., the out-of-plane direction of the pillar, reflecting the compression of the pillar along its z-axis due to the applied load until failure at ~2% strain; an expected value for ceramic hard coating materials [50]. Conversely, the Poisson effect implies lateral expansion in the x and y directions to accommodate the volume change resulting from the pillar compression in the z direction. Under uniform uniaxial loading conditions, the lateral strain components for a cylindrical pillar are equal in magnitude ($\varepsilon_{yy}^{hkl} = \varepsilon_{xx}^{hkl}$, i.e., $\varepsilon_{xy}^{hkl} = \varepsilon_{yx}^{hkl} = 0$ is valid) and represent the elastic deformation perpendicular to the direction of loading. Although the shear strain components ($\varepsilon_{zy}^{hkl} = \varepsilon_{zx}^{hkl}$) are expected be close to zero, the minimal shear deformations observed do not indicate significant deviation from uniform loading conditions or inelastic material behavior during the experiment.

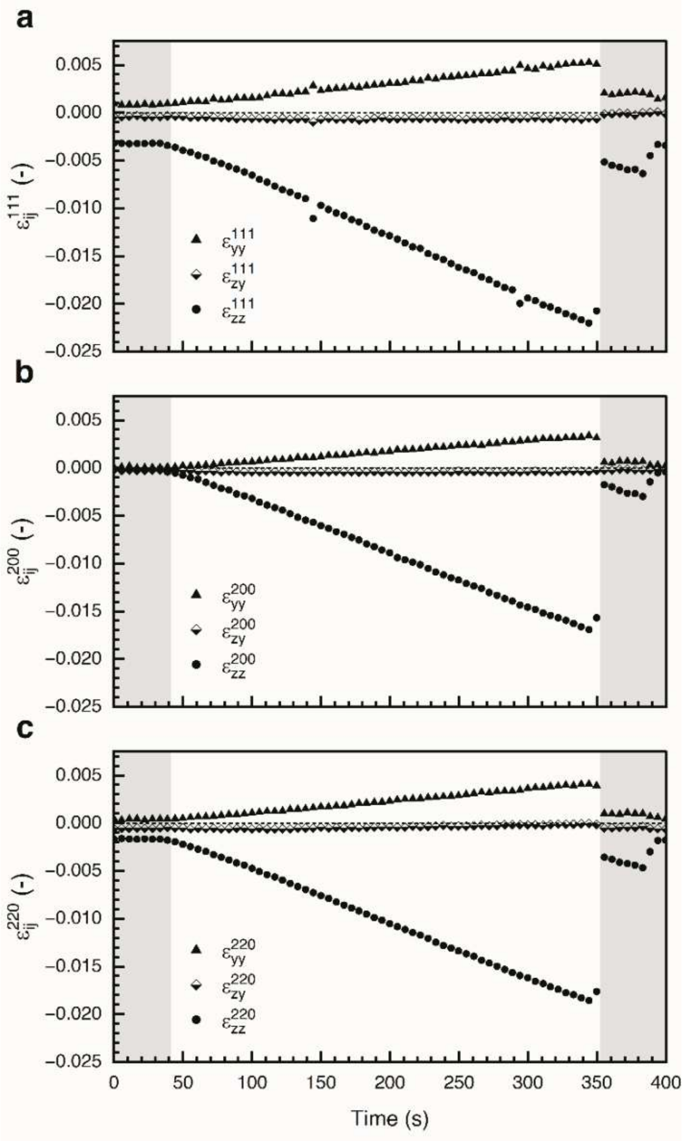

Figure 7.4. Elastic strain components of $TiN_{0.8}B_{0.2}$ derived from in-situ uniaxial pillar compression testing for three distinct crystallographic planes {*hkl*} are shown: (a) ε_{ij}^{111}, (b) ε_{ij}^{200}, and (c) ε_{ij}^{220}. Each plot illustrates the calculated strain data points at load time (i) in the loading direction z, ε_{zz}^{hkl} (indicated by filled circles,) (ii) in the lateral direction, $\varepsilon_{yy}^{hkl} = \varepsilon_{xx}^{hkl}$ (filled triangles), and (iii) the shear strain components, $\varepsilon_{zy}^{hkl} = \varepsilon_{zx}^{hkl}$ (shown as half-filled diamonds). The strain values recorded during pre-loading and post-failure of the pillar appear on a grey background.

The almost linear progression of ε_{yy}^{hkl} and ε_{zz}^{hkl} over the time of applied load suggests a predominantly linear elastic material behavior that is relatively consistent across the three crystallographic planes (Fig. 7.4a-c). However, we observe a nuanced elastic anisotropy in the material's response to uniaxial compression. Specifically, ε_{yy}^{111} and ε_{zz}^{111} propagated to slightly higher magnitudes compared to the in-plane and out-of-plane strain components recorded for the {220} and {200} planes (compare Fig. 7.3a-c). Note that in sputtered polycrystalline thin films, the presence of crystallographic textures can contribute to the macroscopic anisotropy of the material [40]. The presence of (virtual) residual strains, particularly notable in the z direction for the {111} peak, ε_{zz}^{111}, may also partly stem from lattice defects favoring specific crystallographic plane families. However, using free-standing pillar geometries for in-situ mechanical testing offer advantages over previously reported methods [44,79] in revealing the intrinsic coating material's mechanical properties by allowing the material to deform freely under applied load. Free-cutting a cylindrical shaped pillar out of the deposited coating material mitigates residual stresses—commonly observed in conventional sputtered PVD thin films—providing a uniform stress-strain distribution throughout the specimen and reducing frictional forces during deformation [59]. In combination with synchrotron X-ray microdiffraction this approach allowed us to in-situ collected detailed information on the pillar's deformation response to uniaxial compression in the lateral and longitudinal direction for three independent crystallographic plane families {111}, {200}, and {220}. The so-obtained elastic strain components ε_{ij}^{hkl} are essential for accessing the {*hkl*}-dependent elastic constants.

The Poisson's ratio for each crystallographic plane families {111}, {200}, and {220}, as shown in Fig. 7.5, was determined from the negative ratio of the slope between the transverse strain components, ε_{yy}^{hkl}, and the slope of the axial strain components, ε_{zz}^{hkl}, over a period of 61–327 s. Eq. (7.5). The ν^{hkl} values obtained for $\nu^{111} = 0.241$, $\nu^{200} = 0.199$, and $\nu^{220} = 0.222$ are in the range of 0.2—0.3 commonly observed for ceramic hard coatings and suggest a moderate level of anisotropy in the coating's elastic response. Although {*hkl*}-dependent Poisson's ratios for Ti—B—N coatings have not been studied so far, the values obtained from our experiment appear reasonable when compared to those reported for fcc-TiN thin films [80–82]. Complementarily, the {*hkl*}-dependent Poisson's ratios for $TiN_{0.8}B_{0.2}$ were calculated based on Eq. (7.6), where the negative ratio for each transverse and axial strain data point recorded over the time to failure was derived. However, the resulting 64 $\nu_{d_0}^{hkl}$ values for each crystallographic plane significantly deviated from the one ν^{hkl} value derived from Eq. (7.5), as clearly shown in Figs. 7.5a–c. To refine the determination of $\nu_{d_0}^{hkl}$, we iteratively adjusted the strain-free lattice parameter, $d_0^{hkl} \rightarrow d_{0,\mathrm{r}}^{hkl}$, to fit the $\nu_{d_0}^{hkl}$ values to ν^{hkl} by the method of least-squares, as detailed in the experimental part. The refined values are denoted as $d_{0,\mathrm{r}}^{hkl}$ and $\nu_{d_0}^{hkl}$.

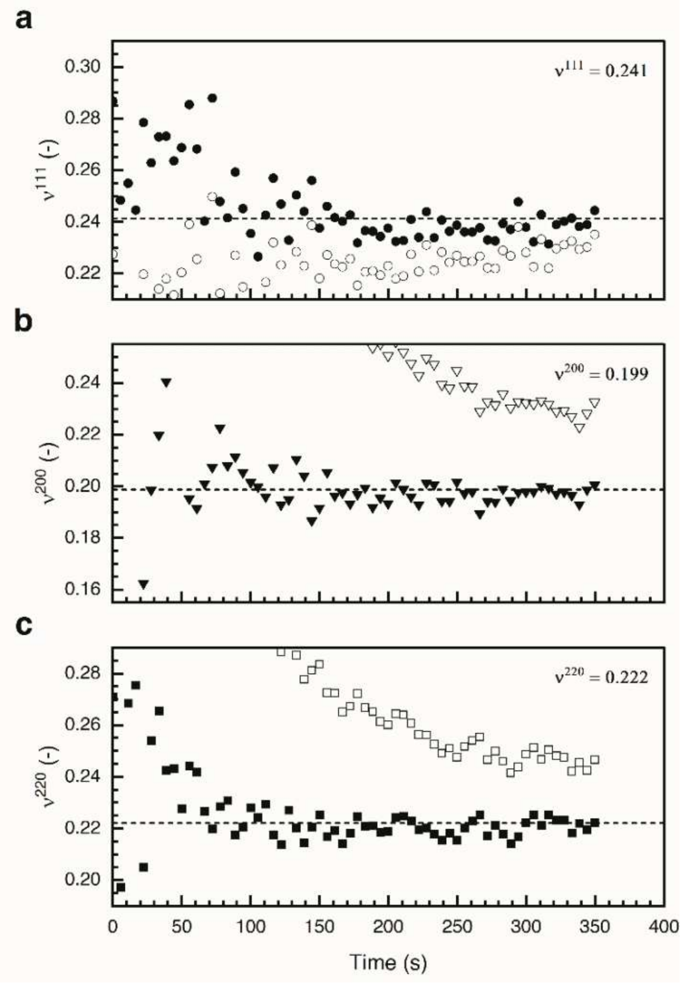

Figure 7.5. Poisson's ratio values of $TiN_{0.8}B_{0.2}$ obtained for three crystallographic plane families {111}, {200}, and {220} shown in panels (a) circular symbols, (b) triangular symbols, and (c) square symbols, respectively. The dashed horizontal line in each panel represents the ν^{hkl} value calculated from the negative ratio of the slope of the lateral and axial strain components, as indicated in the upper right corner. All framed symbols denote the initial $\nu_{d_0}^{hkl}$ values calculated pointwise from the negative ratio of ε_{yy}^{hkl} and ε_{zz}^{hkl}, while filled symbols show the least squares fitted $\nu_{d_{0,\mathrm{r}}}^{hkl}$ values after iterative "fminsearch" optimization of the strain-free lattice parameter from d_0^{hkl} to $d_{0,\mathrm{r}}^{hkl}$. Notably, certain initial $\nu_{d_0}^{hkl}$ values deviate strongly from the ν^{hkl} target value and appear (not visible) outside the plot.

Accurate determination of d_0^{hkl} is critical in diffraction-based stress-strain analyses, often presenting the primary source of uncertainty [83,84]. Even minor alterations in d_0^{hkl} significantly impact the calculated parameters. In this study, the uncertainties of $\nu_{d_0}^{hkl}$ associated with d_0^{hkl} (see Figs. 7.4a–c) were <0.1% underpinning the meticulous precision required in X-ray strain analysis. Ideally, adjusting d_0^{hkl} does not affect the slope of the strain data points (Fig. 7.3a-c), since the calculation of ν^{hkl} (expressed as in (Eq. 7.5)), remains invariant to variations in d_0^{hkl}. This independence arises from the fundamental nature of Poisson's ratio, a material constant that defines the material's transverse response under axial loading. Despite many other factors (i.e., instrumental limitations, sample preparation, or local changes in microstructure and chemical composition [citation]) that can complicate the experimental determination of d_0^{hkl}, optimizing d_0^{hkl} to ensure consistency between the calculated $\nu_{d_0}^{hkl} \rightarrow \nu_{d_{0,\mathrm{r}}}^{hkl}$ values obtained from Eq. (7.6) and ν^{hkl} appears to be a valid approach for $d_{0,\mathrm{r}}^{hkl}$-refinement and to enhance the precision of our results.

7.3.3 X-ray Uniaxial Stress Analysis

In our investigation of the mechanical elastic properties of the $TiN_{0.2}B_{0.8}$ coating, we further analyzed the deviatoric stress components of the micropillar under uniaxial compression loading along the z-direction. This required the use of Eq. (7.9-7.13), which facilitate the calculation of σ_{zz} based on the pre-determined strain components, ε_{ij}^{hkl}, as described in the Methodology section.

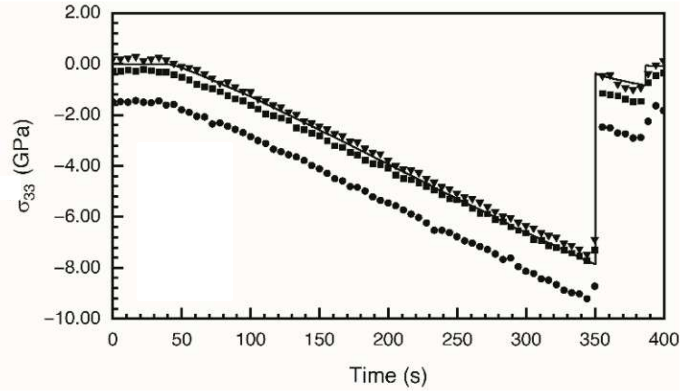

Figure 7.6: Uniaxial compressive stress analysis of a $TiN_{0.8}B_{0.2}$ micropillar showing the stress components evaluated for {111} (circular symbols), {200} (triangular symbols), and {220} (square symbols) evaluated for the three crystallographic planes along with the continuous stress measurements from the indenter, σ_I (continuous line). The plot illustrates stress evolution over load time to failure at 350s and -7.86 GPa.

Our results in Fig. 7.6 show that the calculated stresses for σ_{zz} {200} and σ_{zz} {220} closely match the indenter stress, σ_I, all in GPa. The deviation of σ_{zz} {111} from an initial ~zero stress state presumably prone to texture effects in {111} plane of the material system. Of particular interest, however, is the observed linear increase in compressive stress in the loading direction up to failure. The slope of the three deviatoric stresses, closely aligns with the macroscopic indenter stresses, suggesting a coherent loading response of the {*hkl*} crystallographic plane families inside the probing volume of the pillar. This observation is consistent with the assumption of uniform uniaxial loading conditions and suggests a linear elastic response in the micropillar during testing. Despite the shifted values for $\{111\}$ lattice plane families observed in the pre-loading state, as we are interested in how well our calculated $\frac{1}{2}s_2^{hkl}$ and s_1^{hkl} values match with the macroscopic stresses, σ_I, only the coherency of the slopes is relevant. The micropillar failure at 7.5 GPa (according to σ_I) adds credibility to the validation of the experiment and is in good agreement with fracture behavior observed in other ceramic hard coatings under similar compressive loading scenarios [50].

Since the compressive load is applied uniformly along the z axis, the resulting stress state is assumed to be homogeneously distributed in the mid-section of the pillar according to [59]. Therefore, the deviatoric stress components, σ_{zz}, in our experiment are expected—and shown—to be equal in slope compared to the macroscopic (i.e., {*hkl*}-independent) stress response derived from the indenter, σ_I, allowing the experimental determination of $\frac{1}{2}S_2^{hkl}$ by differentiating Eq. (7.14). In detail, we plotted $\frac{\partial d_{\theta\delta}^{hkl}}{\partial \sin^2\delta}$ over $\overline{\sigma_I}$ and calculated $\frac{1}{2}S_2^{hkl}$ from the first derivative of the linear fit. The polycrystalline directional-dependent X-ray elastic constants link the macro stresses, σ_I, with the directional-dependent strains, ε_{ij}^{hkl}, caused by them. Therefore, $\frac{1}{2}S_2^{hkl}$ and S_1^{hkl}can be inferred from the measured direction-dependent strain changes and the simultaneously recorded macroscopic stresses generated by compressing the pillar with a constant loading rate. The recording of data on the elastic behavior of a material over time allows for the calculation of elastic and diffraction (X-ray) elastic constants from the slope of underlying equations mentioned in the methodology section. This differential approach offers a more precise determination than discrete measurements, as previously demonstrated in the calculation of the Poisson ratio. Given that Eq. (7.12) is in the form of $y = k \cdot x + d$, where S_1^{hkl} is included in the in the y-intercept term, we plotted $\varepsilon_{\theta\delta}^{hkl}(y,z)$ at $\sin^2\delta$=0 against $\overline{\sigma_I}(y,z)$. The elimination of the $k \cdot x$ term allows for the linear fitting of the data points and to calculate S_1^{hkl} from the slope of the line (similar to the procedure for $\frac{1}{2}S_2^{hkl}$). Subsequent, E^{hkl} values were be calculated using the fundamental relationship between elastic and X-ray elastic constants (Eqs. (7.10) and (7.11)).

7.3.4 Thin Film Elastic Constants

Following the experimental determination of the direction dependent thin film elastic constants, ν^{hkl} and E^{hkl}, as well as the X-ray elastic constants $\frac{1}{2}S_2^{hkl}$ and S_1^{hkl}, our investigation extends to the derivation of the polycrystalline thin film elastic constants, ν and E. To interpolate the polycrystalline values from the single crystal X-ray elastic constants, we utilized the known coefficients from the stiffness tensor ($C_{11} = 548.29$, $C_{12} = 133.15$, and $C_{44} = 163.43$) for fcc-$TiN_{0.94}B_{0.06}$ to calculate $\frac{1}{2}s_2^{hkl}$ and s_1^{hkl} according to each of the three models proposed by, Reuss, and Eshelby/Kröner, as described in detail in [62,65–67,83]. Please note, that we used the stiffness tensor for a fcc-$TiN_{0.94}B_{0.06}$ crystal to account for the insufficient B incorporation in our deposited $TiN_{0.8}B_{0.2}$ coating. The peak shift observed in the XRD pattern in Fig. 7.2a indicates that ca. 3 at% B is incorporated in the fcc-TiN lattice with the surplus of B segregated amorphously at the grain boundaries [6]—only the crystals contribute to the analysis.

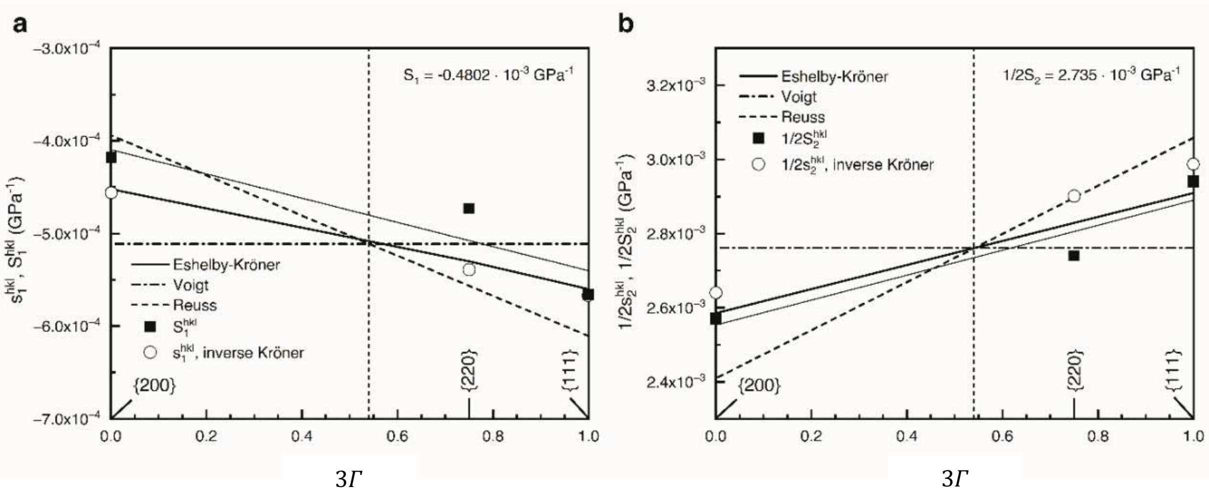

Figure 7.7. 3Γ plot of the single crystal diffraction elastic constants, (a) s_1^{hkl} and (b) $\frac{1}{2}s_2^{hkl}$, derived from the models of Voigt (dashed-dotted line), Reuss (dashed-line), and Eshelby/Kröner (solid line) using the ab into calculated coefficients of the stiffness tensor C_{11}, C_{12}, and C_{44} for fcc-$TiN_{0.94}B_{0.06}$. The experimentally determined X-ray elastic constants (squared symbols) for {111}, {200}, and {220} are predicted to be linear over 3Γ. The hypothetical 3Γ value (0.54) of the unknown quasi-isotropic polycrystalline thin film elastic constants is estimated to be similar to the calculated single crystal X-ray elastic constants (marked by the vertical small-dashed line). The circular symbols represent s_1^{hkl} and $\frac{1}{2}s_2^{hkl}$ calculated from ISDOEC software (based on the inverse Kröner model) and used for the deviatoric stress analysis.

The calculated single-crystal X-ray elastic constants can be represented by the orientation parameter, 3Γ, which expresses the three Miller indices *h*, *k*, and *l* as a single parameter and ranges from 0 to 1, where $3\Gamma\{200\} = 0$, $3\Gamma\{220\} = 0.75$, and $3\Gamma\{111\} = 1$. Specifically for cubic material systems, the Reuss and Eshelby/Kröner models show a linear distribution of $\frac{1}{2}s_2^{hkl}$ and s_1^{hkl} over the parameter 3Γ, whereas Voigt grain interaction model yields a single set of DECs that are independent of the {*hkl*}-plane families (Please note, that generally the Voigt model assumes all grains exhibit the similar strain). The intersection between the three models in Fig. 7.7 indicates where the {*hkl*}-dependent DECs, $\frac{1}{2}s_2^{hkl}$ and s_1^{hkl}, are assumed to be similar to the {*hkl*}-independent (macroscopic) quasi-isotropic polycrystalline thin film elastic constants, i.e., Young's modulus, E, and Poisson's ratio, ν. By interpolating the experimentally determined polycrystalline thin film X-ray elastic constants S_1^{hkl} (Fig. 7.7a) and $\frac{1}{2}S_2^{hkl}$ (Fig. 7.7b) to 3Γ = 0.54—obtained from the intersection of the ab initio DFT data—we can determine $E = 443$ GPa and $\nu = 0.213$ according to Eqs. (7.10) and (7.11).

The comparison in Fig. 7.7 indicates a strong agreement between experimentally determined thin film X-ray elastic constants, S_1^{hkl} and $\frac{1}{2}S_2^{hkl}$, and theoretical predictions, particularly for the Eshelby/Kröner model. Notably, the slopes of the linear fits match closely, especially for $\frac{1}{2}S_2^{hkl}$ and $\frac{1}{2}s_2^{hkl}$. This confirms previous findings indicating the improved performance of the Eshelby/Kröner model in predicting the mechanical elastic behavior of quasi-isotropic polycrystals [83] and that these parameters can be used for stress analysis. We further observe that the s_1^{hkl} values derived from the ISODEC software based on the inverse Kröner model follow those of Eshelby/Kröner. However, in the case of $\frac{1}{2}s_2^{hkl}$, the latter is in better agreement with the experimentally determined $\frac{1}{2}S_2^{hkl}$ values (compare Fig. 7.7a and 7.7b). The ab initio DFT data for $\frac{1}{2}s_2^{hkl}$ shows a slightly better agreement with the experimental data compared to s_1^{hkl}. This discrepancy suggests potential opportunities for refinement in the simulation methodologies, particularly in relation to Poisson's contraction, which will be the focus of future research.

Finally, summarized in Table 7.1, we present the results of our in-situ experimental approach to determine the {*hkl*}-dependent as well as the polycrystalline thin film elastic and X-ray elastic constants for $TiN_{0.8}B_{0.2}$ compared to the theoretically predicted single crystal values. Where possible, the standard error was calculated using Gaussian error propagation. The polycrystalline Young's modulus, E_I, was additionally extrapolated from nanoindentation measurements of the coating with $E_I = 454 \pm 33$ GPa (not added to the table) and matches the polycrystalline thin film Young's modulus interpolated from the in-situ pillar compression experiment (E=443 GPa) as well as the value obtained from the DFT calculations based on the Hill grain interaction model (E=442 GPa), as described in detail in the methodology section. The residual stresses of the $TiN_{0.8}B_{0.2}$ coating, measured at ~ 0.6 GPa, are relatively low compared to E_I. Therefore, the E_I

value can be considered a valid benchmark for comparison with the other experimental and theoretical results. The measured hardness, H = 32.1 ± 1.9 GPa, also falls within the expected range of ~ 35 GPa, in agreement with our previous experimental results [6,85]. The values are slightly higher than those reported for pure TiN in the literature [80–82], indicating a greater compliance for $\mathrm{TiN_{0.8}B_{0.2}}$ compared to TiN. As previously explained, increasing the B content in fcc-TiN results in a reduction of E [6]. This decrease in E can be attributed to the increase in lattice spacing, leading to severe lattice distortions. Furthermore, adding B introduces lattice defects such as N-vacancies or amorphous B-rich grain boundary phases. These irregularities disrupt the uniformity of the fcc-TiN lattice and consequently alter the material's stiffness.

Table 7.1. Summary of the experimental values for the {*hkl*}-dependent and macroscopic thin film elastic constants ν^{hkl}, ν, E^{hkl}, E, and the X-ray elastic constants $\frac{1}{2}S_2^{hkl}$ and S_1^{hkl} for $\mathrm{TiN_{0.8}B_{0.2}}$ compared to the theoretically derived {*hkl*}-dependent and macroscopic single-crystal elastic and X-ray elastic constants, $\frac{1}{2}s_2^{hkl}$ and s_1^{hkl} (derived from the inverse Kröner model) for fcc-$\mathrm{TiN_{0.94}B_{0.06}}$. $\frac{1}{2}S_2$ and S_1 correspond to {*hkl*}-independent experimental thin film X-ray elastic constants interpolated from the intersection of the $3\Gamma^{hkl}$ plot in Fig. 7.7ab, where $\frac{1}{2}s_2$ and s_1 are the theoretical {*hkl*}-independent single-crystal X-ray elastic constants from the Reuss model at the intersection.

Experimentally determined values for $\mathrm{TiN_{0.8}B_{0.2}}$ thin films					
{*hkl*}	{111}	{200}	{220}	macroscopic	
ν^{hkl} (-)	0.241±0.004	0.199±0.001	0.222±0.001	ν (-)	0.213
E^{hkl} (GPa)	422±2	467±2	446±2	E (GPa)	443
$\frac{1}{2}S_2^{hkl}$ (10^{-3} GPa^{-1})	2.94±0.01	2.57±0.01	2.74±0.01	$\frac{1}{2}S_2$ (10^{-3} GPa^{-1})	2.74
S_1^{hkl} (10^{-3} GPa^{-1})	-0.57±0.06	-0.42±0.02	-0.47±0.02	S_1 (10^{-3} GPa^{-1})	-0.48
Theoretically determined values for single crystal fcc-$\mathrm{TiN_{0.94}B_{0.06}}$.					
{hkl}	{111}	{200}	{220}	macroscopic	
ν^{hkl} (-)	-	0.218	0.251	ν (-)	0.229
E^{hkl} (GPa)	408	496	427	E (GPa)	442
$\frac{1}{2}s_2^{hkl}$ (10^{-3} GPa^{-1})	2.9879	2.6400	2.9010	$\frac{1}{2}s_2$ (10^{-3} GPa^{-1})	2.76
s_1^{hkl} (10^{-3} GPa^{-1})	-0.5669	-0.4556	-0.5390	s_1 (10^{-3} GPa^{-1})	-0.51

7.4 Summary and Conclusion

In this study, we aim to develop a new in-situ test routine to experimentally determine the direction dependent elastic constant of polycrystalline thin films using in-situ micro-pillar compression testing coupled with X-ray strain analysis. To provide a suitable quasi-isotropic ceramic coating for testing, we deposited a 15 µm $TiN_{0.8}B_{0.2}$ thin film (H = 32.1±1.9 GPa, E_I = 454±33 GPa), characterized by a dense, small-grained (non-columnar) microstructural cross section. X-ray diffraction analysis confirmed the presence of a single-phase crystalline fcc-TiN structure with peak shifts attributed to 3 at% B incorporation within the fcc-TiN lattice, while excess B is segregated as amorphous B-rich grain boundary phases. The micro-pillar (aspect ratio 3:1) fabricated by a conventional FIB milling process displayed a symmetric taper ($\alpha<2°$) and was qualified for controlled compression testing. By implementing an advanced in-situ nanoindentation setup, we subjected the $TiN_{0.8}B_{0.2}$-micropillar to uniform uniaxial compression with a constant deformation rate until failure, while simultaneously performing transmission X-ray microdiffraction to detect the {*hkl*}-dependent deformation response for the {111}, {200}, and {220} plane families. We directly obtained the direction-dependent Poisson ratio, ν^{hkl}, from the negative ratio of the slopes of the linear elastic strain response, $\frac{d}{dt}\varepsilon_{ij}^{hkl}$, to the applied load over time in the transverse and axial directions until the pillar failed with absence of plastic deformation. In addition, we refined the determination of the strain-free lattice spacing, $d_0^{hkl} \rightarrow d_{0,\mathrm{r}}^{hkl}$, by iteratively adjusting the $\nu_{d_0}^{hkl}$ values obtained from the negative strain ratio $-\frac{\varepsilon_{yy}^{hkl}}{\varepsilon_{zz}^{hkl}}$ to fit the differentially derived Poisson ratio ν^{hkl}. Considering this deviation, we were able to refine d_0^{hkl} with the required accuracy of 10^{-5} nm for X-ray diffraction stress-strain analysis. The unique ability of our experiment to simultaneously record deformation changes, $\frac{\partial d_{\theta\delta}^{hkl}}{\partial \sin^2\delta}$, and corresponding uniaxial macroscopic stresses, $\overline{\sigma_I}$, allowed to determine the thin film X-ray elastic constants, $\frac{1}{2}S_2^{hkl}, S_1^{hkl}$, followed by the direction-dependent thin film Young's modulus E^{hkl}. The thereby derived elastic constants such as ν^{111} = 0.241±0.004, ν^{200} = 0.199±0.001, ν^{220} = 0.222±0.001, E^{111} = 422±2 GPa, E^{200} = 467±2 GPa, and E^{220} = 446±2 GPa, excellently agree with DFT-values of ν^{200} = 0.218, ν^{220} = 0.251, E^{111} = 408 GPa, E^{200} = 496 GPa, and E^{220} = 427 GPa.

Having successfully calculated the directional-dependent thin film elastic constants and X-ray elastic constants from our experiments we interpolated the polycrystalline (macroscopic) thin film elastic constants, ν and E, from the calculated single-crystal X-ray elastic constants, $\frac{1}{2}s_2^{hkl}$, s_1^{hkl}, using the theoretical models proposed by Reuss, Voigt, and Eshelby/Kröner. Particularly, the Eshelby/Kröner model showed the best alignment with experimental data.

7.5 References

[1] P.H. Mayrhofer, C. Mitterer, L. Hultman, H. Clemens, Microstructural design of hard coatings, Prog Mater Sci. 51 (2006) 1032–1114.

[2] M. Stueber, H. Holleck, H. Leiste, K. Seemann, S. Ulrich, C. Ziebert, Concepts for the design of advanced nanoscale PVD multilayer protective thin films, J Alloys Compd. 483 (2009) 321–333.

[3] H. Kindlund, D.G. Sangiovanni, I. Petrov, J.E. Greene, L. Hultman, A review of the intrinsic ductility and toughness of hard transition-metal nitride alloy thin films, Thin Solid Films. 688 (2019).

[4] W. Zhai, L. Bai, R. Zhou, X. Fan, G. Kang, Y. Liu, K. Zhou, Recent Progress on Wear-Resistant Materials: Designs, Properties, and Applications, Advanced Science. 8 (2021).

[5] B. Breidenstein, B. Denkena, P. Wolters, M. Keitel, W. Tillmann, D. Stangier, N.F. Lopes Dias, A novel development of sustainable cutting inserts based on PVD-coated natural rocks, Materials Today Sustainability. 24 (2023).

[6] R. Janknecht, R. Hahn, N. Koutná, T. Wójcik, E. Ntemou, A. Steiger-Thirsfeld, Z. Chen, A. Kirnbauer, P. Polcik, S. Kolozsvári, Z. Zhang, D. Primetzhofer, P.H. Mayrhofer, A Strategy to Enhance the B-Solubility and Mechanical Properties of Ti–B–N Thin Films, Acta Mater. 271 (2024) 119858.

[7] C. Fuger, R. Hahn, A. Hirle, P. Kutrowatz, M. Weiss, A. Limbeck, O. Hunold, P. Polcik, H. Riedl, Revisiting the origins of super-hardness in TiB2+z thin films – Impact of growth conditions and anisotropy, Surf Coat Technol. 446 (2022).

[8] A. Bahr, S. Richter, R. Hahn, T. Wojcik, M. Podsednik, A. Limbeck, J. Ramm, O. Hunold, S. Kolozsvári, H. Riedl, Oxidation behaviour and mechanical properties of sputter-deposited TMSi2 coatings (TM = Mo, Ta, Nb), J Alloys Compd. 931 (2023).

[9] J. Ast, M. Ghidelli, K. Durst, M. Göken, M. Sebastiani, A.M. Korsunsky, A review of experimental approaches to fracture toughness evaluation at the micro-scale, Mater Des. 173 (2019).

[10] J.H. Choi, H. Kim, J.Y. Kim, K.H. Lim, B.C. Lee, G.D. Sim, Micro-cantilever bending tests for understanding size effect in gradient elasticity, Mater Des. 214 (2022).

[11] W. Luo, C. Kirchlechner, X. Fang, S. Brinckmann, G. Dehm, F. Stein, Influence of c omposition and crystal structure on the fracture toughness of NbCo2 Laves phase studied by micro-cantilever bending tests, Mater Des. 145 (2018) 116–121.

[12] J. Ast, G. Mohanty, Y. Guo, J. Michler, X. Maeder, In situ micromechanical testing of tungsten micro-cantilevers using HR-EBSD for the assessment of deformation evolution,

Mater Des. 117 (2017) 265–266.

[13] P. Peierls, The size of a dislocation, Proc Phys Soc. 52 (1940) 34–37.

[14] F.R.N. Nabarro, Dislocations in a simple cubic lattice, Proc Phys Soc. 59 (1947) 256–272.

[15] R.L. Fleischer, Substitutional solution hardening, Acta Metallurgica. 11 (1963) 203–209.

[16] E.O. Hall, The Deformation and Ageing of Mild Steel: III Discussion of Results, Proceedings of the Physical Society. Section B. 64 (1951) 747–747.

[17] N.J. Petch, The influence of grain boundary carbide and grain size on the cleavage strength and impact transition temperature of steel, Acta Metallurgica. 34 (1986) 1387–1393.

[18] E. Orowan, Fracture and strength of solids, Prep Prog Phys. 12 (1949) 185–232.

[19] J.G. Byrne, M.E. Fine, A. Kelly, Precipitate hardening in an Aluminium-Copper Alloy, Philosophical Magazine. 6 (1961) 1119–1145.

[20] G.I. Taylor, A Theory of the Plasticity of Crystals, Z Kristallogr – Cryst Mater. 89 (1934) 375–385.

[21] X.Q. Chen, H. Niu, D. Li, Y. Li, Modeling hardness of polycrystalline materials and bulk metallic glasses, Intermetallics (Barking). 19 (2011) 1275–1281.

[22] E. Mazhnik, A.R. Oganov, A model of hardness and fracture toughness of solids, J Appl Phys. 126 (2019).

[23] H. Niu, S. Niu, A.R. Oganov, Simple and accurate model of fracture toughness of solids, J Appl Phys. 125 (2019).

[24] Y. Le Page, P. Saxe, Symmetry-general least-squares extraction of elastic data for strained materials from ab initio calculations of stress, Phys Rev B Condens Matter Mater Phys. 65 (2002) 1–14.

[25] R. Yu, J. Zhu, H.Q. Ye, Calculations of single-crystal elastic constants made simple, Comput Phys Commun. 181 (2010) 671–675.

[26] Y. Le Page, P. Saxe, Symmetry-general least-squares extraction of elastic coefficients from ab initio total energy calculations, Phys Rev B Condens Matter Mater Phys. 63 (2001).

[27] V. Revi, S. Kasodariya, A. Talapatra, G. Pilania, A. Alankar, Machine learning elastic constants of multi-component alloys, Comput Mater Sci. 198 (2021).

[28] G. Vazquez, P. Singh, D. Sauceda, R. Couperthwaite, N. Britt, K. Youssef, D.D. Johnson, R. Arróyave, Efficient machine-learning model for fast assessment of elastic properties of high-entropy alloys, Acta Mater. 232 (2022).

[29] H. Levämäki, F. Tasnádi, D.G. Sangiovanni, L.J.S. Johnson, R. Armiento, I.A. Abrikosov, Predicting elastic properties of hard-coating alloys using ab-initio and machine learning

methods, NPJ Comput Mater. 8 (2022).

[30] A.A. Griffith, The phenomena of rupture and flow in solids, Phil Trans R Soc Lond A. 221 (1921) 163–198.

[31] G.R. Irwin, Analysis of Stresses and Strains Near the End of a Crack Traversing a Plate, J Appl Mec. 12 (1957) 361–364.

[32] V. Moraes, H. Riedl, C. Fuger, P. Polcik, H. Bolvardi, D. Holec, P.H. Mayrhofer, Ab I nitio inspired design of ternary boride thin films, Sci Rep. 8 (2018).

[33] K. Balasubramanian, S. V. Khare, D. Gall, Valence electron concentration as an indicator for mechanical properties in rocksalt structure nitrides, carbides and carbonitrides, Acta Mater. 152 (2018) 175–185.

[34] N. Koutná, A. Brenner, D. Holec, P.H. Mayrhofer, High-throughput first-principles search for ceramic superlattices with improved ductility and fracture resistance, Acta Mater. 206 (2021).

[35] H. Chan, B. Narayanan, M.J. Cherukara, F.G. Sen, K. Sasikumar, S.K. Gray, M.K.Y. Chan, S.K.R.S. Sankaranarayanan, Machine Learning Classical Interatomic Potentials for Molecular Dynamics from First-Principles Training Data, Journal of Physical Chemistry C. 123 (2019) 6941–6957.

[36] F. Tasnádi, F. Bock, J. Tidholm, A. V. Shapeev, I.A. Abrikosov, Efficient prediction of elastic properties of Ti0.5Al0.5N at elevated temperature using machine learning interatomic potential, Thin Solid Films. 737 (2021).

[37] S. Lin, L. Casillas-Trujillo, F. Tasnádi, L. Hultman, P.H. Mayrhofer, D.G. Sangiovanni, N. Koutná, Machine-learning potentials for nanoscale simulations of tensile deformation and fracture in ceramics, NPJ Comput Mater. 10 (2024).

[38] A.C. Fischer-Cripps, Critical review of analysis and interpretation of nanoindentation test data, Surf Coat Technol. 200 (2006) 4153–4165.

[39] E. Eiper, K.J. Martinschitz, J. Keckes, Combined elastic strain and macroscopic stress characterization in polycrystalline Cu thin films, Powder Diffr. 21 (2006) 25–29.

[40] K.J. Martinschitz, R. Daniel, C. Mitterer, J. Keckes, Elastic constants of fibre-textured thin films determined by X-ray diffraction, J Appl Crystallogr. 42 (2009) 416–428.

[41] M. Alfreider, M. Meindlhumer, V. Maier-Kiener, A. Hohenwarter, D. Kiener, Extracting information from noisy data: strain mapping during dynamic in situ SEM experiments, J Mater Res. 36 (2021) 2291–2304.

[42] M. Alfreider, M. Meindlhumer, T. Ziegelwanger, R. Daniel, J. Keckes, D. Kiener, Revealing dynamic-mechanical properties of precipitates in a nanostructured thin film

using micromechanical spectroscopy, MRS Bull. 49 (2024) 49–58.

[43] M. Alfreider, I. Issa, O. Renk, D. Kiener, Probing defect relaxation in ultra-fine grained Ta using micromechanical spectroscopy, Acta Mater. 185 (2020) 309–319.

[44] M.D. Uchic, D.M. Dimiduk, J.N. Florando, W.D. Nix, Sample dimensions influence strength and crystal plasticity, Science. 305 (2004) 986–989.

[45] J. Todt, J. Zalesak, C. Krywka, J. Keckes, Influence of Gradient Residual Stress and Tip Shape on Stress Fields Inside Indented TiN Hard Coating, Adv Eng Mater. 23 (2021).

[46] S. Heinze, T. Krülle, L. Ewenz, C. Krywka, A. Davydok, A. Stark, R. Cremer, C. Leyens, Influence of the deposition process and substrate on microstructure, phase composition, and residual stress state on as-deposited Cr-Al-C coatings, Mater Des. 225 (2023).

[47] C. Krywka, H. Neubauer, M. Priebe, T. Salditt, J. Keckes, A. Buffet, S.V. Roth, R. Doehrmann, M. Mueller, A two-dimensional waveguide beam for X-ray nanodiffraction, J Appl Crystallogr. 45 (2012) 85–92.

[48] G. Lotze, A.H.S. Iyer, O. Bäcke, S. Kalbfleisch, M.H. Colliander, In situ characterization of stresses, deformation and fracture of thin films using transmission X-ray nanodiffraction microscopy, J Synchrotron Radiat. 31 (2024) 42–54.

[49] M. Meindlhumer, L.R. Brandt, J. Zalesak, M. Rosenthal, H. Hruby, J. Kopecek, E. Salvati, C. Mitterer, R. Daniel, J. Todt, J. Keckes, A.M. Korsunsky, Evolution of stress fields during crack growth and arrest in a brittle-ductile CrN-Cr clamped-cantilever analysed by X-ray nanodiffraction and modelling, Mater Des. 198 (2021).

[50] L. Zauner, R. Hahn, E. Aschauer, T. Wojcik, A. Davydok, O. Hunold, P. Polcik, H. Riedl, Assessing the fracture and fatigue resistance of nanostructured thin films, Acta Mater. 239 (2022).

[51] A. Zeilinger, J. Todt, C. Krywka, M. Müller, W. Ecker, B. Sartory, M. Meindlhumer, M. Stefenelli, R. Daniel, C. Mitterer, J. Keckes, In-situ Observation of Cross-Sectional Microstructural Changes and Stress Distributions in Fracturing TiN Thin Film during Nanoindentation, Sci Rep. 6 (2016).

[52] J. Todt, C. Krywka, Z.L. Zhang, P.H. Mayrhofer, J. Keckes, M. Bartosik, Indentation response of a superlattice thin film revealed by in-situ scanning X-ray nanodiffraction, Acta Mater. 195 (2020) 425–432.

[53] W. Ecker, J. Keckes, M. Krobath, J. Zalesak, R. Daniel, M. Rosenthal, J. Todt, Nanoscale evolution of stress concentrations and crack morphology in multilayered CrN coating during indentation: Experiment and simulation, Mater Des. 188 (2020).

[54] W.C. Oliver, G.M. Pharr, An improved technique for determining hardness and elastic

modulus using load and displacement sensing indentation experiments, J Mater Res. 7 (1992) 1564–1583.

[55] G. Benecke, W. Wagermaier, C. Li, M. Schwartzkopf, G. Flucke, R. Hoerth, I. Zizak, M. Burghammer, E. Metwalli, P. Müller-Buschbaum, M. Trebbin, S. Förster, O. Paris, S. V. Roth, P. Fratzl, A customizable software for fast reduction and analysis of large X-ray scattering data sets: Applications of the new DPDAK package to small-angle X-ray scattering and grazing-incidence small-angle X-ray scattering, J Appl Crystallogr. 47 (2014) 1797–1803.

[56] J.C. Lagarias, J.A. Reeds, M.H. Wright, P.E. Wright, Convergence propoerties of the Nelder-Mead simpley method in low dimensions*, Siam J Optim. 9 (1998) 112–147.

[57] H. Möller and M. Gerhard, Elastische Anisotropie und röntgenographische Spannungsmessung, Verlag Stahleisen, 1939.

[58] C. Zener, Classical Theory of the Temperature Dependence of Magnetic Anisotropy Energy, Phys Rev. 96 (1954) 1335–1337.

[59] A. Cornec, E. Lilleodden, Numerical analysis of micropillar compression behaviour and stress-strain curve estimation verified on glass fused silica, Mater Today Commun. 33 (2022).

[60] J. Keckes, R. Daniel, J. Todt, J. Zalesak, B. Sartory, S. Braun, J. Gluch, M. Rosenthal, M. Burghammer, C. Mitterer, S. Niese, A. Kubec, 30 nm X-ray focusing correlates oscillatory stress, texture and structural defect gradients across multilayered TiN-SiOx thin film, Acta Mater. 144 (2018) 862–873.

[61] T. Gnäupel-Herold, ISODEC: Software for calculating diffraction elastic constants, J Appl Crystallogr. 45 (2012) 573–574.

[62] E. Kröner, Berechnung der elastischen Konstanten des Vielkristalls aus den Konstanten des Einkristalls, Z Physik. 151 (1958) 504–518.

[63] T. Gnäupel-Herold, A.A. Creuziger, M. Iadicola, A model for calculating diffraction elastic constants, J Appl Crystallogr. 45 (2012) 197–206.

[64] H. Behnken, Mikrospannungen in vielkristallinen und heterogenen Werkstoffen, Shaker-Verlag, 2003.

[65] A. Reuss, Berechnung der Fließgrenze von Mischkristallen auf Grund der Plastizitätsbedingung für Einkristalle, Z angew Math Mech. 9 (1929) 49–58.

[66] W. Voigt, Lehrbuch der Kristallphysik (mit Ausschluss der Kristalloptik), B.G. Teubner, 1910.

[67] J.D. Eshelby, The Determination of the Elastic Field of an Ellipsoidal Inclusion, Proc R

Soc Lond A. 1226 (1957) 376–396.

[68] U. Welzel, J. Ligot, P. Lamparter, A.C. Vermeulen, E.J. Mittemeijer, Stress analysis of polycrystalline thin films and surface regions by X-ray diffraction, J Appl Crystallogr. 38 (2005) 1–29.

[69] G. Kresse, J. Furthmüller, Efficient iterative schemes for ab initio total-energy c alculations using a plane-wave basis set, Phys Rev B. 54 (1996) 11169–11186.

[70] G. Kresse, D. Joubert, From ultrasoft pseudopotentials to the projector augmented-wave method, Phys Rev B. 59 (1999) 1758–1775.

[71] J.P. Perdew, K. Burke, M. Ernzerhof, Generalized Gradient Approximation Made Simple, Phys Rev Lett. 77 (1996) 3865–3868.

[72] W. Kohn, L.J. Sham, PHYSICAL REVIEW Self-Consistent Equations Including Exchange and Correlation Effects, Phys Rev. 140 (1965) A1133–A1138.

[73] S.-H. Wei, L.G. Ferreira, J.E. Bernard, A. Zunger, Electronic properties of random alloys: Special quasirandom structures, Phys Rev B. 42 (1990) 9622.

[74] D.G. Sangiovanni, F. Tasnádi, L.J.S. Johnson, M. Odén, I.A. Abrikosov, Strength, transformation toughening, and fracture dynamics of rocksalt-structure $Ti_{1-x}Al_xN$ $(0 \leq x \leq 0.75)$ alloys, Phys Rev Mater. 4 (2020) 033605.

[75] M. Moakher, A.N. Norris, The closest elastic tensor of arbitrary symmetry to an elasticity tensor of lower symmetry, J Elast. 85 (2006) 215–263.

[76] R. Hill, The Elastic Behaviour of a Crystalline Aggregate, Proc Phys Soc A. 65 (1952) 349–354.

[77] J.F. Nye, Physical Properties of Crystals, Oxford University Press, 1985.

[78] S. Gates-Rector, T. Blanton, The Powder Diffraction File: a quality materials characterization database, Powder Diffr. 34 (2019) 352–360.

[79] G. Abadias, E. Chason, J. Keckes, M. Sebastiani, G.B. Thompson, E. Barthel, G.L. Doll, C.E. Murray, C.H. Stoessel, L. Martinu, Review Article: Stress in thin films and coatings: Current status, challenges, and prospects J. Vac. Sci. Technol. A. 36 (2018) 020801.

[80] J.O. Kim, J.D. Achenbach, P.B. Mirkarimi, M. Shinn, S.A. Barnett, Elastic constants of single-crystal transition-metal nitride films measured by line-focus acoustic microscopy, J Appl Phys. 72 (1992) 1805–1811.

[81] J. Almer, U. Lienert, R.L. Peng, C. Schlauer, M. Odén, Strain and texture analysis of coatings using high-energy x-rays, J Appl Phys. 94 (2003) 697–702.

[82] M. Zhang, J. He, Ab-initio calculation of elastic constants of TiN, Surf Coat Technol. 142–144 (2001) 125–131.

[83] L. Spieß, G. Teichert, R. Schwarzer, H. Behnken, Ch. Genzel, Moderne Röntgenbeugung, Vieweg+Teubner Verlag Wiesbaden, 2009.

[84] P.J. Withers, M. Preuss, A. Steuwer, J.W.L. Pang, Methods for obtaining the strain-free lattice parameter when using diffraction to determine residual stress, J Appl Crystallogr. 40 (2007) 891–904.

[85] R. Hahn, A. Tymoszuk, T. Wojcik, A. Kirnbauer, T. Kozák, J. Čapek, M. Sauer, A. Foelske, O. Hunold, P. Polcik, P.H. Mayrhofer, H. Riedl, Phase formation and mechanical properties of reactively and non-reactively sputtered Ti-B-N hard coatings, Surf Coat Technol. 420 (2021).

S7 Supplementary Materials

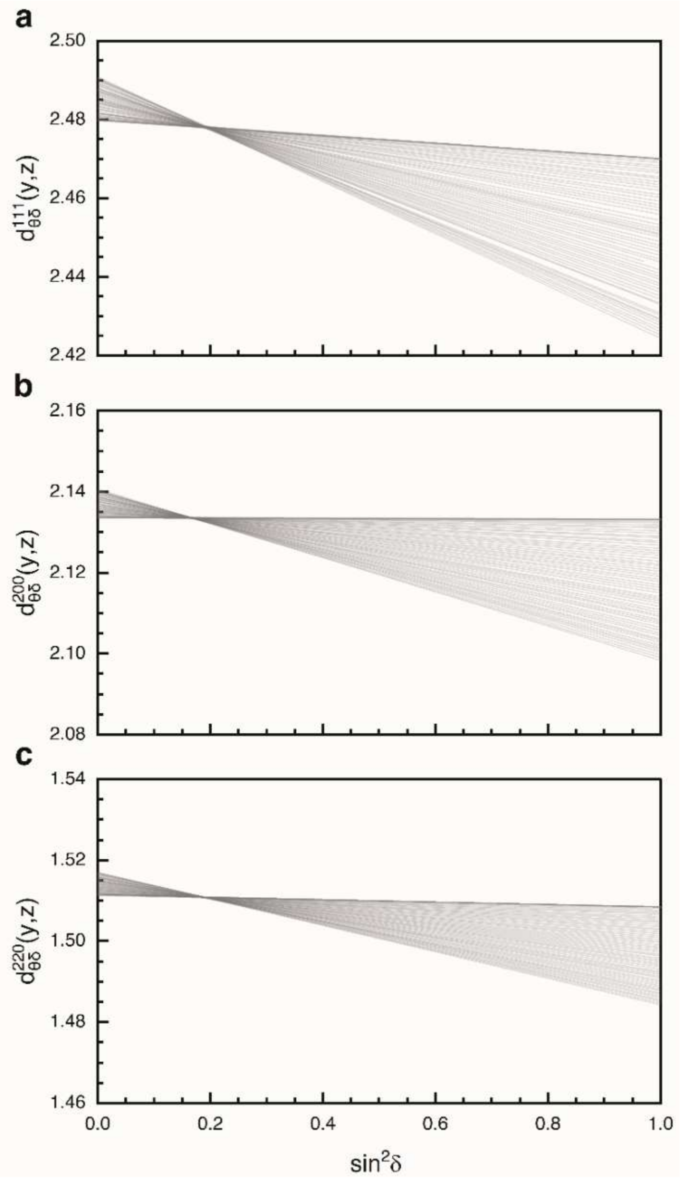

Figure S7.1. (a), (b), and (c) show the linear fits of all 36 lattice parameters $d_{\theta\delta}^{hkl}$ from the first recorded diffraction pattern until one pattern before failure of the pillar for the {111}, {200}, and {220}, respectively, regarding their $sin^2\ \delta$ value. The initial d_0^{hkl} value is determined at the intersection of all linear fits.

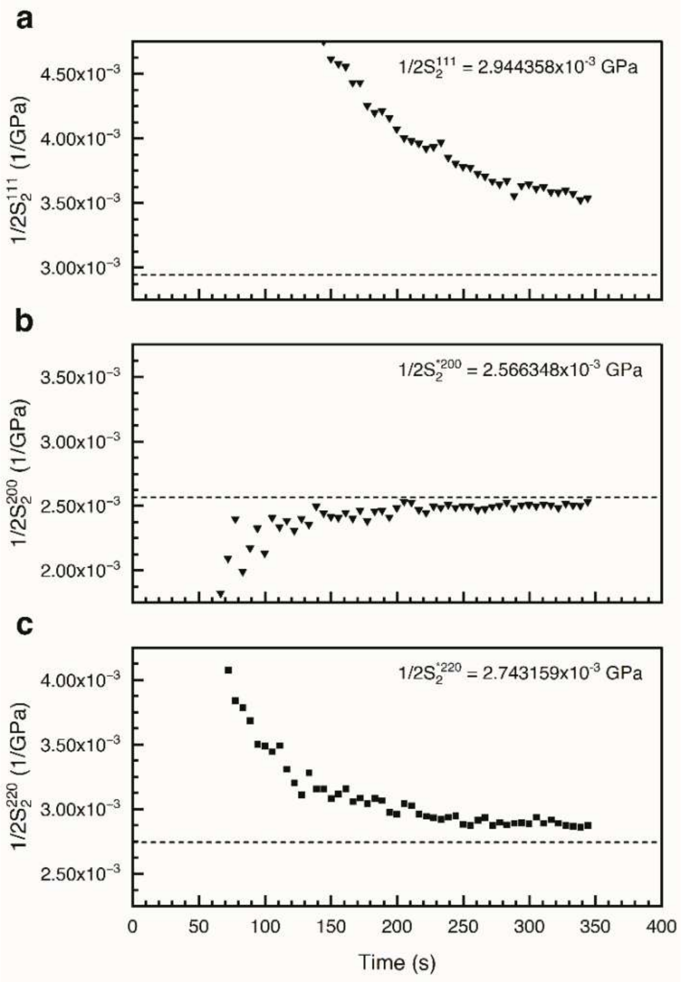

Figure S7.2. $\frac{1}{2}S_2^{hkl}$ values of TiN$_{0.8}$B$_{0.2}$ obtained for three crystallographic plane families {111}, {200}, and {220} shown in panels (a) triangular symbols, (b) triangular symbols, and (c) square symbols, respectively. The dashed horizontal line in each panel represents the $\frac{1}{2}S_2^{hkl}$ value calculated from the ratio of the slopes of the linear fit of the $d_{\theta\delta}^{hkl}$ over $sin^2\,\delta$ over the discrete indentation stress values, $\overline{\sigma}_I(y,z)$, as indicated in the upper right corner.

8 Summary

This thesis contains three major chapters—next to the more general description of the used model system Ti–B–N and experimental methods used—describing and explaining the possibilities to modify the B-solubility within the TiN-lattice and introducing a method through which the elastic constants can fully be obtained experimentally (incl. the Poisson's ratio, which very often is simply assumed or calculated).

Chapter 5 focusses on the solubility behavior of B in fcc-TiN using non-reactive co-sputtering. The addition of titanium to TiN can increase the solubility of boron by creating vacancies in the non-metal sublattice or, more generally, by creating a stoichiometry that deviates from the TiN-TiB_2 line in the ternary phase diagram. An essential aspect of this work is that detailed XRD investigations would be sufficient to prove a so-called solid solution of boron on the non-metal sublattice. These findings have been corroborated by DFT simulations, which predict the same trend in the lattice parameter and elastic properties (polycrystalline Young's modulus) as obtained by XRD and nanoindentation. The solid solution in the case of additional Ti was confirmed by complementary HRTEM investigations, which showed us that B is uniformly distributed in the TiN lattice with a chemistry along the TiN–TiB tie line in a coating.

In contrast, an increased occurrence of B at the grain boundaries was observed without Ti addition. The effect of this solubility is not primarily seen in an increase in hardness of the coating, but in a significant improvement in fracture toughness compared to the coating without additional titanium. In conclusion, this work has highlighted the importance of correct chemical composition and XRD's very good determinability of a solid solution.

Chapter 6 presents a concept to further modify the solubility of B in fcc-TiN. By targeted microalloying of metals on the metal sublattice allows to manipulate the spatial conditions so that the solubility of B was intentionally either favored or hindered. Specifically, Cr or Zr was added to reduce (Cr) or increase (Zr) the lattice parameter of the basic Ti–Me–N system, thus favoring or limiting the solubility of boron (which has a larger covalent radius than N) on the non-metal sublattice. This study was also supported by DFT calculations, which showed that stretching the lattice improves B solubility. Such calculations were also used to determine the local strain due to the bond distance between titanium and boron (Ti-B) compared to titanium and nitrogen (Ti-N). These calculations support the experimental trend established by XRD, which was that the solution of B is promoted in the case of Zr addition—more than obtained through simply adding Ti, which promotes the formation of vacancies at the non-metal sublattice—and reduced when alloying Cr to TiN.

Chapter 7 focusses on a combination of micromechanics and synchrotron beam diffraction. This allows to entirely measure the elastic constants of materials. Specifically, a micropillar (Ti–B–N was also used as a reference system) was loaded at constant strain rate, and scattering experiments were performed simultaneously using a micro-focused synchrotron beam. The strains occurring in the material are calculated by analyzing the resulting Debye-Scherrer pattern in detail to determine the so-called Poisson's ratio. X-ray elastic constants were then obtained using the recorded force at the indenter and the known gradients or zero crossings of d over sin2θ. By analyzing three different families of planes, it was possible to determine these and subsequently calculate Young's moduli as a function of crystallographic directions. Finally, polycrystalline values were calculated, assuming that the intersection points of three different models for calculating the theoretical directional constants must intersect at the same point as the measured values. The experimentally determined elastic constants show excellent agreement with DFT obtained values, so a methodology was successfully developed which allows the determination of elastic constants on a purely experimental basis. This advancement represents a significant enrichment in materials research, as other techniques use assumed or calculated Poisson’s ratios.

In summary, this thesis shows how the solubility of alloying elements can be manipulated using the Ti–B–N model system, and how the elastic constants (directional values such as E^{111}, E^{100}, and Poisson’s ratio) can entirely be obtained through experiments without assumed or calculated inputs (like often done with Poisson’s ratio). These three chapters have in common the material system, the powerful tool of X-ray diffraction, and my passion and accuracy.